Proceedings of the 10^{th} International Workshop on Radiation Safety at Synchrotron Radiation Sources

MAX IV Laboratory, Lund University, Sweden.
22-24 May 2019

Contents

Effect of Magnetic Fields on Bremsstrahlung Radiation

Stuart Ansell

MAX IV Laboratory, Lund University, Sweden.
October 2019

Abstract

At most X-ray synchrotron beamlines, the bremsstrahlung radiation field generated from the electron interactions with the residual gases in the ring are highly forward sampled by the beamline collimation systems. Although there is no direct interaction of the magnetic fields in the bremsstrahlung process, the angular deviation of the electron beam while it passes through the undulators, relative to the fixed beamline collimation, and the highly angular dependence of the emmitted photons in the bremsstrahlung process, results in a signficant change in the radiation field in optics hutches. This paper examines the required methodology to correctly calculate this effect, the variance observerd and compares this with experimental measurements done at MAX IV.

1 Introduction

At most synchrotron facilities, 3D Monte Carlo codes, e.g. Fluka, MCNP etc. are use to help evaluate the radiation shielding and instrument background effects. These codes spend considerable effort in accurately simulating the different physics processes that can occur at any state point from the high energy (GeV) electrons in a storage ring to the low energy photons and neutrons before absorption. The quality of the physics models is now sufficiently accurate that the geometry errors and transport statistics are potentially the dominate error. In addition, the synchrotron light from coherent electron effects in the magnetic fields of the undulators, are often separately calculated in different code (e.g. XOP, XRT) and thus the magnetic fields are often neglected from the 3D Monte Carlo calculations.

Of these three type of error (geometry,magnetic,variance), the first two can be estimated readily by simulation using the pertibation method. This is typcially done by adding a more complete geomety or by adding a more detailed magnetic field. Variance reduction which is seldom done by this method, because the process of reducing the variance reduction typically leads to expondential increase in computational time, which is prohibative.

This paper examines the effect of adding the magnetic field on the radiation field in the MaxPEEM beamline optics hutch at MAX IV. We examine both measured and calculated for Monte Carlo because it is possible to vary just the magnetic field in both the simulation and the experimental measurement.

1.1 Bresstrahlung process

At a synchrotron, the electrons orbit in a ring, which consists of sections in which the electrons experience a net dipole field, and "straight sections" in which the net dipole field is zero. Undulators/Wigglers are inserted into these straight sections and consequently the optics hutches are aligned on these axises. The collimation that is places before the optics hutch is normally very tight ($\sim \mathrm{mrad}$) but it is in the optics hutch that the characteristic large thick walls of the ring tunnel, necessitated by the requirement to shield direct electrons loses, are replaced

with thinner (lead) walls that are only required to shield radiation from bresstrahlung processes. Therefore it is necessary to accurately calculate the forward going processes that can be accepted by this collimation.

The bresstrahlung process occurs when an electron is deflected by a charged particle and a photon is emmitted. This occurs in storage rings by an interaction between the electron and the atomic nucleus of a residual gas molecule from the vacuum of the ring. The electron loses energy and is deflected. The process is isotropic in the centre of mass frame, but due to the high electron relativistic gamma factor, it is predominantly forward going in the laboritory frame. The process gives rise to two sources of radiation that enters the optics hutch. First, is the bremsstrahlung photons that are emmited from the direct interaction. Second, are from the secondary particles that electrons create via pair interactions, when they encounter the walls of the vacuum system (in the vicinity of the undulator), and then are able to find a route via the collimation [1] into the the optics hutch.

1.2 Geometry

The accuracy of the geometry of the beamline determines the minimum error on the secondary bremmmstrahlung radiation field in the optics hutch. The collimation is critical to be accurately simulated, both in terms of position and materials, because the collimators often provide weak attenuation above $1\,\mathrm{MeV}$ in the proximimity of the true aperature centre due to angular cuts on the collimator. Additionally, the optics hutch can direclty see a fraction of the surface area of the undulator vacuum system and the electron/photon seperation vacuum systems.

Since it is difficult to determine the exact components that will contribute to the radiation field, it is much simpler to model all components with a high level of detail. However, the current Monte Carlo code e.g. Fluka/MCNP which all use continuous volume geometry (CVG) which are efficient at path tracking for Monte-Carlo, but are highly inefficient for developing large scale geometries due to two issues. The first is their use of singular Eurler rotation systems which disallows components to be readily built in any vectorial basis set and inserted, unless the component is completely devolved from the existing model, so has one Eurler rotation relative to the primary origin and basis set. Secondly, the insertion of an object into an existing object results in the boolean inversion of the inserted object. This process is either done by a human intensive or because none of the codes provide boolean optimization methods results in an overly complex object due to unnecessary surfaces and results in significant runtime performance issues.

We minimize these problems by using a C++ code (CombLayer), we have developed. The conceptial space of the program is outlined in figure 1. The user specifies the beamline by writing a C++ function that requests each component type and indicates which components it links too. Each component is designed in isolation (although can borrow surfaces if required from other components), along the a simplified basis set, for example it it common to design a component with the Y axis along the direction of the beam and the Z axis pointing upwards. It is possible to design and object with multiple basis sets if useful (e.g. a mirror box can have an incoming and outgoing basis set). In addition, all the sizes, thicknesses are controlled by user variables, thus a large and small gate valve will only be one component.

The rotation problem is simplified by allowing every component (a set of objects) to be rotated via a quaternion rotation system. This avoids all the gimbol lock problems that Fluka/MCNP/Phits suffer from by using rotation matrixes. It also improves runtime performance because rotations are expensive in ray tracing Monte Carlo, as they must be done for each track. As each component after rotation has new unique surfaces, there is another surprising performance increase, due to each object having less other objects with which it shares a common surface. This means that as a particle leaves an object, the job of finding the next cell is greatly simplified.

The offset and basis set rotation is typcially decided by assignment relative to the connection point on an existing component (with displacement,rotation as needed) and in a sence the basis set of the objects propergate down the beamline as it is constructed. Therefore the user typically doesn't have to interact at all with the rotation system because the rotations are defined by connection points.

The combined effect of this geometric system can be seen in the layout of the MaxPEEM beamline (figure 2a). The beamline has a 4° bend after the M1 mirror, and a vertial step and angle after the monochromator followed by a split, however, several of the components (slits/gate valves) are reused in both sides of the beamline

[1] It is rare that the collimation system is sufficiently tight that the optics hutch only views vacuum until before the undulator.

The insertion system is simplified by constructing the boolean algebra of object and then applying Shannon expansion and decomposition (after applying surface implicates in which surface that are parallel or included are re-inserted into the boolean algebra as implication (surface A is true impiles surface B is true) to remove unnecessary surfaces and simplify the boolean algebra of the obejct [4]. This is particularly important for FLUKA, which expands each cell into a disjoint normal form and has an upper limit on the number of surfaces in a cell.

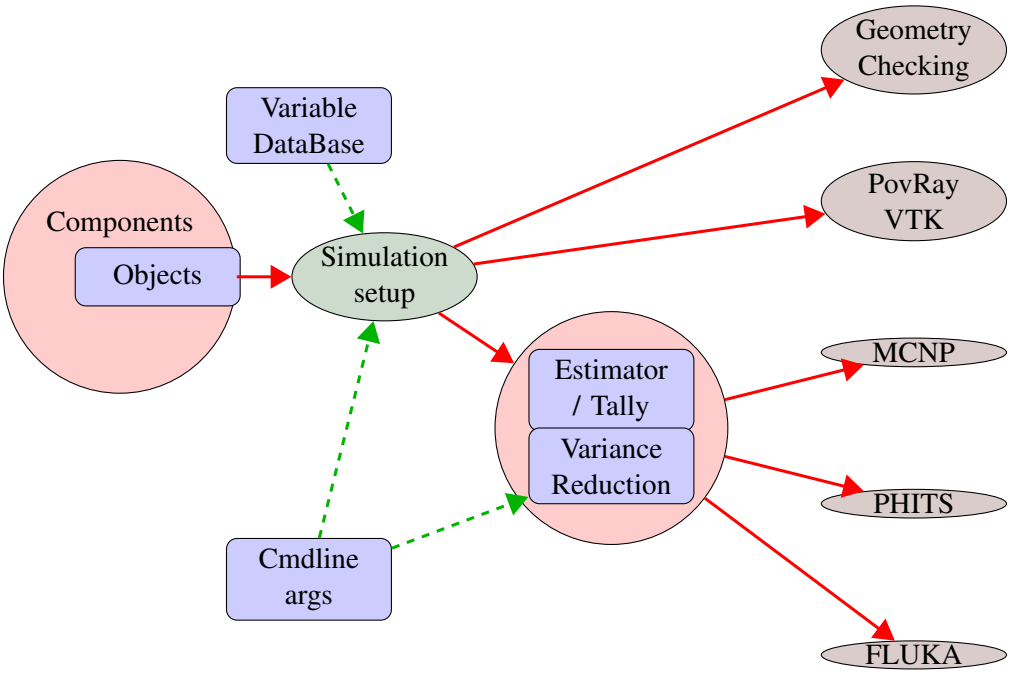

Figure 1: *The primary data components within the CombLayer probram. User controlled flow is marked in dashed green arrows, and computational flow is marked in red arrow. Program flow results in any combination of final outputs. The simualtion setup has both programatic and/or user input.*

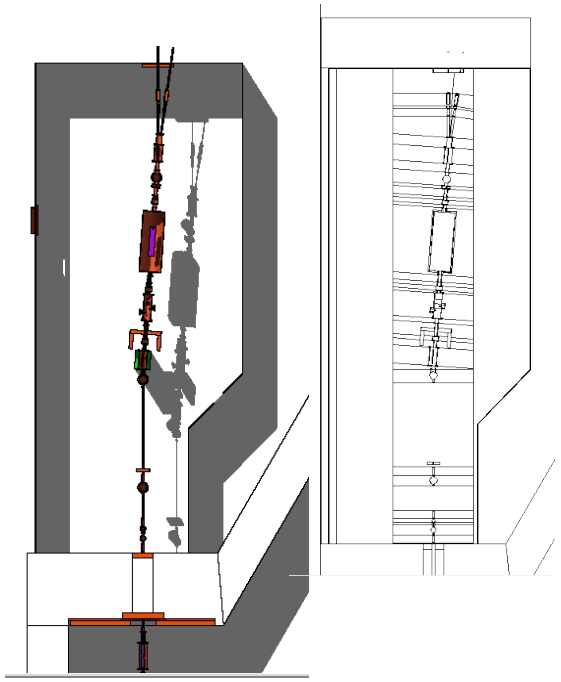

(a) *The geometric layout of the MaxPEEM beamline's optics hutch, both rendered in the Povray 3d view (with shadows) and showing a plane cut with cell boundaries (displaced to the right). This highlights the automatically produced cell cutting divisions that reduce the cell complexity of the optics hutch inner cell.*

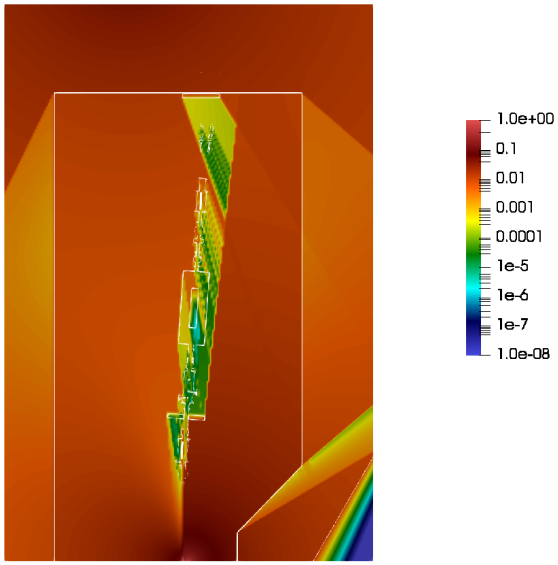

(b) *The CombLayer produced variance reduction weight window mesh for forward going particles P=(0,1,0) for* $100\,\mathrm{keV}$ *photons towards the outside the back wall tally.*

Figure 2

1.3 Magnetic fields

Typically the tight collimation on a beamline means that the bremsstrahlung radiation from the whole straight section produces highly forward going particles, due to the high gamma value for the electrons, and The exact direction of the photons is therefore dependent on the direction of the electrons at the moment of the bremsstrahlung process.

After the electrons enter the straight section of a beamline, the first magnetic field that the electrons encounter is the undulator field. This field has a net zero directional perturbation for the electrons entering the undulator. Typically it has not been included in Monte Carlo simulations for radiation safety except for the purpose of generating synchrotron light, but it was found to be of interest. The electrons do not take a straight path but instead oscillate in the horizontal plane, which increase the total path length by an insignificant factor (10^{-5}). The angle, on the other hand, varies by $\pm 0.6°$ for the MAXPEEM undulator. In the event of a bremsstrahlung interaction both the bremsstrahlung photon and electron are highly forward directional. However, it is necessary to consider the oscillating direction of the electron as it travels down the wiggler. This movement broadens the bremsstrahlung cone, effectively reducing the direct photon bremsstrahlung that can directly exit the fixed masks by a factor 4.

However, this is only part of the contribution to the radiation field in the optics hutch. There are contributions from secondary particles that are generated when the recoil electron from the bremsstrahlung process hits the vacuum system, and if the photon cannot enter the vacuum system then the secondary paritlce from their interction must also be taken into account. Therefore, the magnetic fields for all the magnets in the first part of the ring achromat after the undulator (which for MAX IV is a QSQ Quad-Sextupole-Quad configuration [QSQ]) need to be modeled as they can divert the path of the bremsstrahlung electron into viewable material.

The electron field in the region after the undulator is shown in figure 3. It shows that the main electron beam going round the dipole field and then they are artificially removed, but also the high electron focusing into the

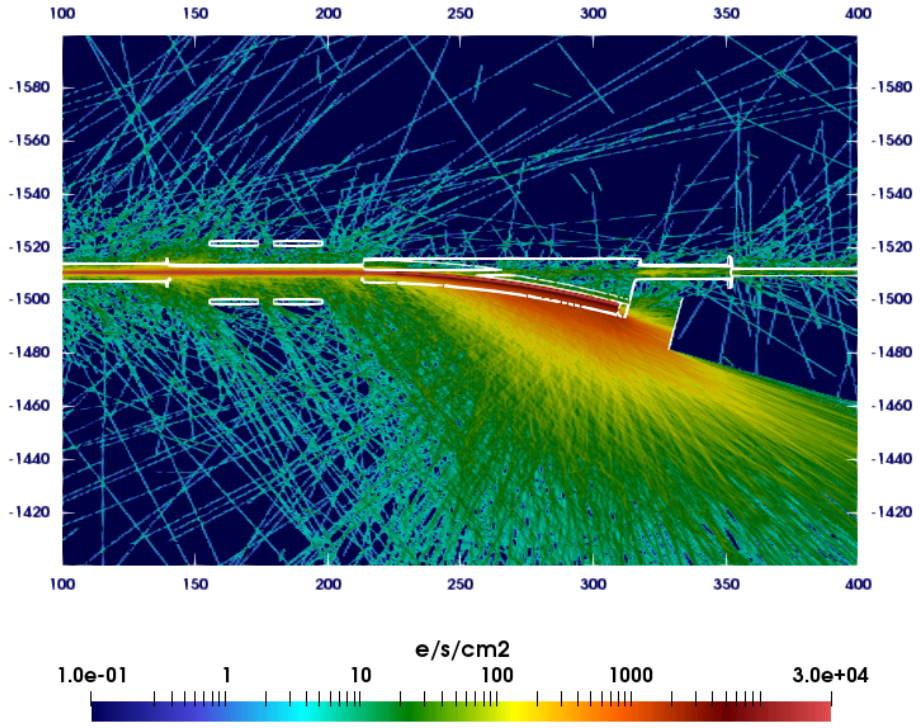

(a) *Horizontal view at electron height.*

Figure 3: *The electron flux distribution going through the last part of the undulator and the first part of the ring achromat after the undulatorx (a dipole and a QSQ (M1) magnet block). Electrons enter from the left and the ones successfully bend by the dipole magnet are eliminated from the exit of the dipole bend pipe.*

choke separate just after the end of the magnet block, along with the electrons that are "over" bent into the dipole inner vacuum surface after they have lost energy in the bremsstrahlung process.

2 Bremsstrahlung

The full Bethe-Heitler (equation 1) cross section is a complex cross section but computationally integrable with numerical care at the limits [1] [2]. It has a strong $\frac{1}{q^4}$ dependence which makes it very forward going, however, in the highest angles this term in comensurate with the momentum exchange sum that the factor is multiplied by.

[2] For a modern reviews see for example: C. Kohn and U. Ebert *Angular distribution of Bremsstrahlung photons and of positrons for calculations of terrestrial gamma-ray flashes and positron beams* [2]

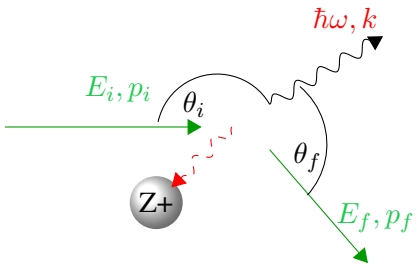

Figure 4: *Schematic diagram for the virtual photon bremsstrahlung exchange process. $\hbar\omega, k$: photon Energy/momentum, E_i, E_f, p_i, p_f : electron inital/final energy/momentum, ϕ_i, ϕ_f intial final angles*

$$\frac{d^4\sigma}{d\omega d\Omega_i d\Omega_f d\phi} = \frac{Z^2\alpha^3\hbar^2}{4\pi^2}\frac{|p_f|}{|p_i|}\frac{1}{\omega|q|^4}\left[\frac{p_f^2\sin^2\theta_f}{(E_f - c|p_f|\cos\theta_f)^2}(4E_i^2 - c^2q^2) + \frac{p_i^2\sin^2\theta_i}{(E_i - c|p_i|\cos\theta_i)^2}(4E_f^2 - c^2q^2)\right.$$
$$\left. +2\hbar^2\omega^2\frac{p_i^2\sin\theta_i + p_f^2\sin\theta_f}{(E_f - c|p_f|\cos\theta_f)(E_i - c|p_i|\cos\theta_i)} - \frac{2|p_i||p_f|\sin\theta_i\sin\theta_f\cos\phi}{(E_f - c|p_f|\cos\theta_f)(E_i - c|p_i|\cos\theta_i)}(2E_i^2 + 2E_f^2 - c^2q^2)\right] \quad (1)$$

The integrated cross section of the solid angle of the photon shown in figure 5 and shows a drop of two orders of magnitude between zero and the maximum photon angle. This is highly significant for typcial Max IV beamlines because the acceptance angle of the front end mask is between 40 and 400 µrad. Further the electron beam undergoes a oscillation of ±5000 µrad. The overlap integral with the MaxPEEM front end mask is sufficient to reduce the non-magnetic field direct photon intensity by a factor 10.

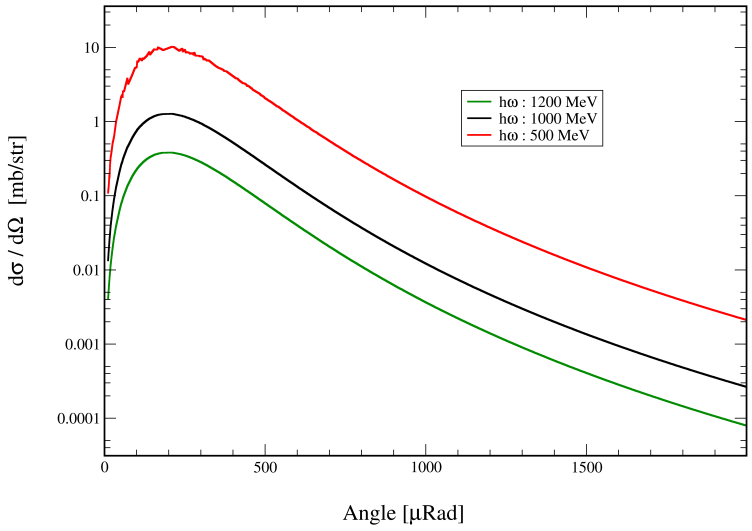

Figure 5: *Bremsstrahlung integrated cross section for photon production from a carbon nucleius with incident electron energy of* 1.5 GeV.

3 Experimental

The basic experiment places a detector (BRM) within the optics hutch at the point of maximum bremsstrahlung dose and measures the resultant radiation field, with the undulator fully open and the undulator fully closed. The results are then modeled with a high detail Monte Carlo model [12000 components] using FLUKA [3], in which the magnetic field of the undulator and the M1 magnet block QSQ and dipole components are simulated.

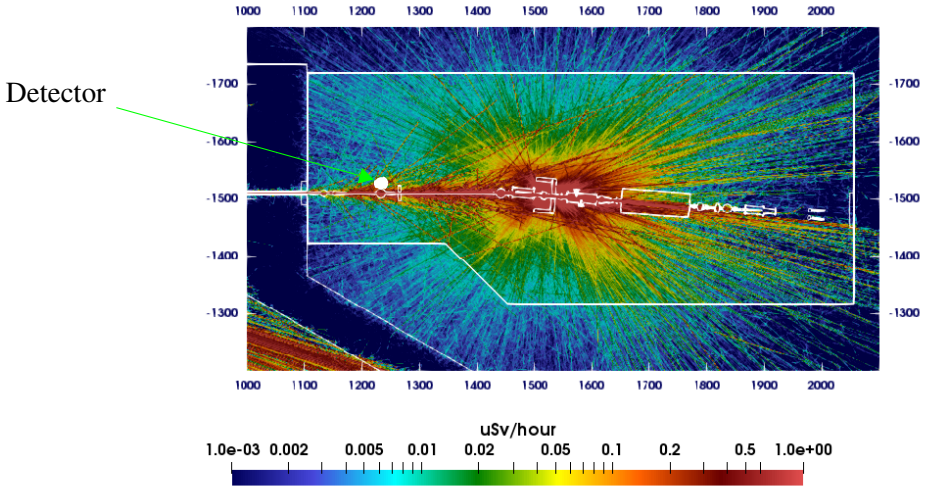

Figure 6: *Monte Carlo dose rate simulation in the optics hutch of MaxPEEM. The dose rate distribution is for the z plane of the electron orbit. Calculated at* $250\,\mathrm{mAmp}$ *at zero magnetic field in the undulator.*

The newly commissioned MaxPEEM beamline provided a good location for experimental verification of the application of the theory and simulation method. In the first few weeks of a new beamline, the vacuum in the undulator relatively high ($5 \times 10^{-9}\,\mathrm{mbar}$) as the vacuum system outgases. However, in this case we were unable to fully closed the undulator magnets due to outgassing from components further upstream (M1 Mirror), so the full difference in magnetic field was not available. A $1.5\,\mathrm{GeV}$ undulator is unable to produce high energy photons via the synchrotron process, with the 1 photon per second limit on MaxPEEM occuring at $4.5\,\mathrm{keV}$. This is completely stopped by the vacuum system so the only radiation we are measuring must come from the electron lost processes, which for a new beamline is dominated by bremsstrahlung.

A BRM detector was placed just after the M1 mirror, and the beamline was in a normal operation mode. Care was taken to model the experimental position of the variable collimators that were necessary to prevent thermal damage to the M1 mirror, and the gas pressure was estimated from the two ion pumps either side of the undulator.

Figure 6 shows the bremsstrahlung radiation in the optics hutch calculated by Fluka. The detector was not small enough to fit into the L-shaped shielding after the M1 Mirror so was placed next to the mirror. The integral of the detector volume in the 3D Monte Carlo field was used to calculate the effective dose rate seen by the detector.

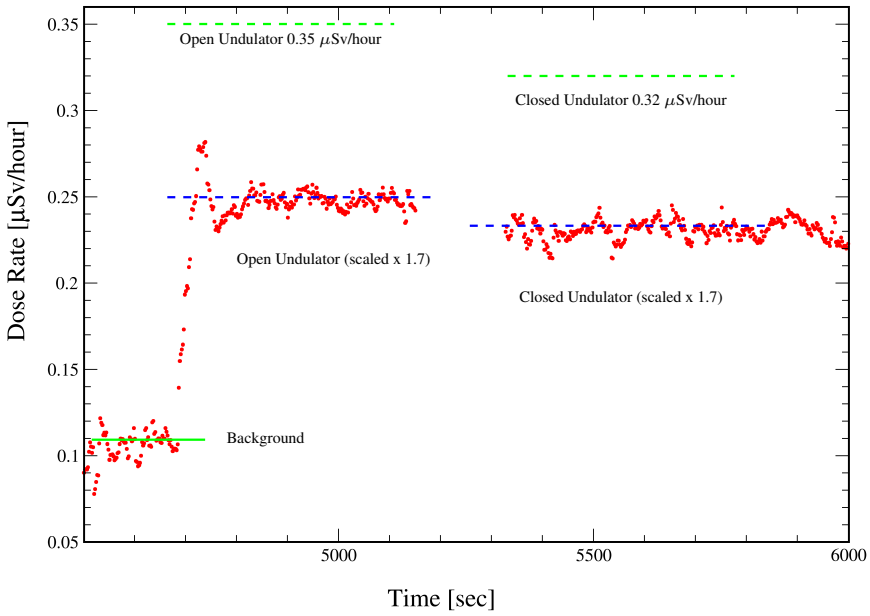

Figure 7: *Dose rate measurements in the MaxPEEM optics hutch compared to Monte Carlo simulation. Those point on the left of the break were measured with undulator closed, and those on the right were measured with the undulator open (no magnetic field). The experimental data ha been normalized to a ring current of* $250\,\mathrm{mAmp}$. *Green dashed lines are monte carlo results + a background of* $0.11\,\mu\mathrm{Sv/h}$, *and the blue lines are the same Monte Carlo results divided by 1.7 before adding a background of* $0.11\,\mu\mathrm{Sv/h}$.

The results of the experimental measurement are shown in figure 7 along with the simulation results. The absolute level was not in agreement with the experimental data but the largest systematic error is believed to be the true pressure in the undulator. This is because we can only measure the pressure either side of the undulator, and the electron beam sweeps out a volume of the gas on each pass. If we scale both the simulation results by 1.7 then we can see good agreement to both "with field" and "without field" simulations. This gives a good indication that the relative values are correct. It also is indicative that the ratio between direct photons from bremsstrahlung and the indirect secondary effects have been correctly modeled.

4 Conclusions

These experiments and calculations show that magnetic fields are important, particularly when small aperature systems are used for synchrotron beamlines. The theory and simulation seem to agree well with the experimental data.

It was also found important that the longer undulators an accurate model is used, as the contribution from secondary events comes to dominate the optics hutch radiation field. Additionally, the most important region for the inclusion of magnetic fields would seem to be the new free-electron lasers (FELs), because the straight sections are signficiantly further from the aperatures so the solid angle from the the early undulators is extremely small.

References

[1] H.A. Bethe, W. Heitler, *On the stopping of fast particles and on the creation of positive electrons.* Proc. Phys. Soc. Lond. **146**, 83–112 (1934).

[2] Christoph Köhn, Ute Ebert, *Angular distribution of Bremsstrahlung photons and of positrons for calculations of terrestrial gamma-ray flashes and positron beams* Atmospheric Research, **135-136**, pp. 432-465 (2012).

[3] A. Fasso, A. Ferrari, J. Ranft, P.R. Sala, *FLUKA, A multi-particle transport code*, CERN-2005-10, INFN/TC_05/11, SLAC-R-773 (2005).

[4] C. Soviani, O. Tardieu, and S. A. Edwards *Optimizing Sequential Cycles Through Shannon Decomposition and Retiming* IEEE Transactions on Computer-Aided Design of Integrated Circuits and Systems, Vol 26, pg. 456 (2007)

Characteristics of Laser Compton Scattering photon beams and its application to radiation safety researches

Y. Asano

NewSUBARU/Laboratory of advanced Science and Technology for Industry
University of Hyogo
October-2019

Abstract

The production process of laser Compton scattering (sometimes we call backward Compton scattering or laser electron) photon beam is presented including the spectra depending on the electron energy and optical laser photon energy by using SPring-8 and NewSUBARU cases. Two methods to obtain quasi-mono energy photons for the laser Compton scattering photon beam and the effect of the stored electron emittance to the quasi mono- energy photons are discussed including the application to the radiation safety reaserches of synchrotron radiation facilities and electron accelerators.

1 Introduction

Laser Compton Scattering (LCS) photon beams have many characteristics such as an unique spectrum that has the maximum peak intensity at the maximum energy. In addition to the unique spectrum, the photon energy and the polarity can be changed easily with changing the electron energy or optical laser polarization. Recently, many LCS beamlines have been constructed in association with operating synchrotron radiation facilities to investigate science and technology [1],[2],[3],[4] . LCS photons with more than MeV energy can be available easily more and more with developing accelerator and optical laser techniques. Polarized high energy photons can be also utilized relatively and easily. Therefore, in addition to the utilization to research of nuclear physics [5] , detector developments of space physics [6] , the application research to physical protection of nuclear materials [7] and the transmutation to produce exclusively radioactive isotopes [8] and so on have been started. Some plans of small size LCS systems are now presented to obtain high energy photons with a tabletop size to use in industry and safety.

In 1923, Compton scattering was discovered [9] , and backward Compton scattering was proposed by Feenberg et al. [10] in 1948. In 1963, Milbum, Arutyunian et al. proposed to produce LCS by using high energy electrons [11],[12] , and Kulikov et al. observed LCS photons (Max 8.3MeV) by using a 600MeV synchrotron machine and a ruby laser in 1964 [13] . Many LCS beamlines were operated until now such as NCLS, ESRF, UVSOR and so on. A few high energy LCS beamlines are now routinely operated. At SPring-8 site, we have three LCS beamlines; two beamlines are at SPring-8, LEPS [3] and LEPS-II [4] , the other is BL-1 at NewSUBARU [4] . Characteristics of these beamlines are presented including how to obtain quasi-mono energy photons and the present status of LCS beamlines in the world. The availability to use radiation safety investigation is also overviewed including our activity [14],[15] to measure photo-neutron distribution due to photo-nuclear reaction depending on photon polarization.

2 Fundamentals of LCS photon

LCS photons can be derived in the same way of Compton scattering by using energy conservation and momentum conservation laws as indicated in formula 1 and 2, respectively. In this case, collision electrons have high energy and recoil photons go to backward as shown in Fig.1,

$$h\nu + (E_i - m_e c^2) = h\nu' + (E - m_e c^2) \tag{1}$$

$$\frac{h\nu}{c}\vec{e} + \vec{p_i} = \frac{h\nu'}{c}\vec{e'} + \vec{p} \tag{2}$$

$$E_i^2 = c^2(p_i^2 + m_e^2 c^2) \tag{3}$$

$$E^2 = c^2(p^2 + m_e^2 c^2) \tag{4}$$

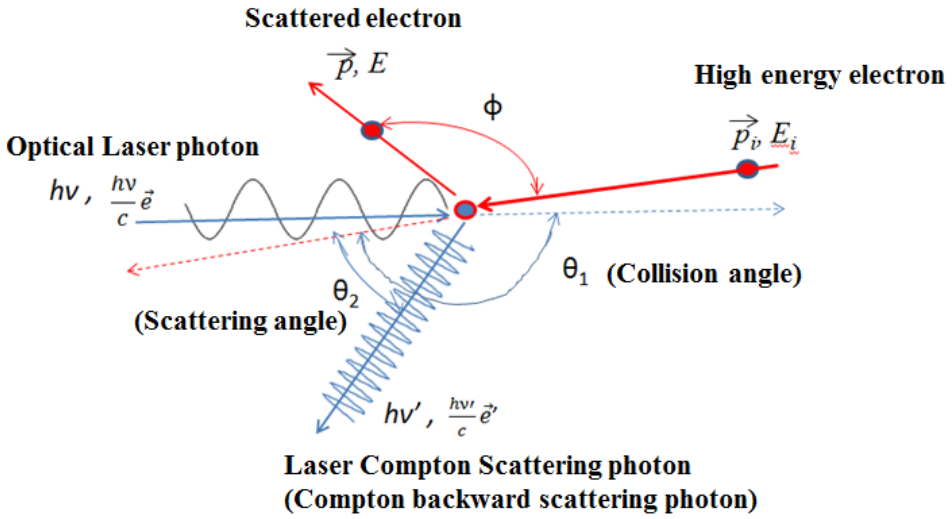

Figure 1: *Schematic drawing of the production of laser Compton scattering photons. In this case, high energy electron collides with optical laser photon with the collision angle of* θ_1 .

where m_e and c are the rest mass of electron and light velocity. E_i and $\vec{p_i}$ are the energy and the momentum of collision electron, respectively. E and $\vec{p}$ are for scattered electron. $h\nu$ and $\frac{h\nu}{c}\vec{e}$ are the photon energy and the momentum of collision optical laser, respectively. $h\nu'$ and $\frac{h\nu'}{c}\vec{e'}$ are the LCS photon energy and the momentum. θ_1 and θ_2 are collision angle between high energy electron and optical laser photon and the scattering angle of the LCS photon from the direction of the high energy electron, respectively. ϕ is the scattering angle of electron. Using these formula, LCS photon energy can be derived as follows,

$$h\nu' = h\nu \frac{E_i - c \cdot p_i \cos\theta_1}{E_i - c \cdot p_i \cos\theta_2 + h\nu(1 - \cos(\theta_1 - \theta_2))} \tag{5}$$

As shown in this formula, the energy of LCS photon depends on the energy of the optical laser and the electron, E_i , and $h\nu$, and the angles of the collision and the scattering, θ_1 and θ_2. For example, Figs. 2 and 3 show the relation between photon scattering angle θ_2 and LCS photon energy, $h\nu'$ in the case of the head on collision ($\theta_1 = \pi$), and the LCS photon spectra are shown in Figs.4 and 5.

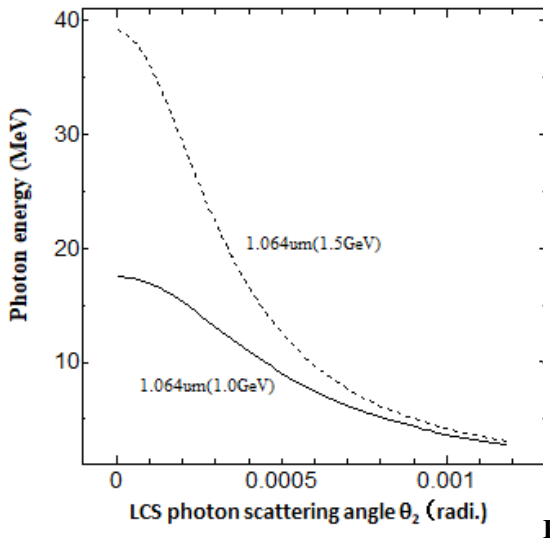

Figure 2: *LCS photon energy on a function of the scattering angle θ_2 with the* $1.064\,\mu$m *laser and electron energy* 1.5 GeV *(dash line) and* 1 GeV *(solid line). (NewSUBARU BL-1 case)*

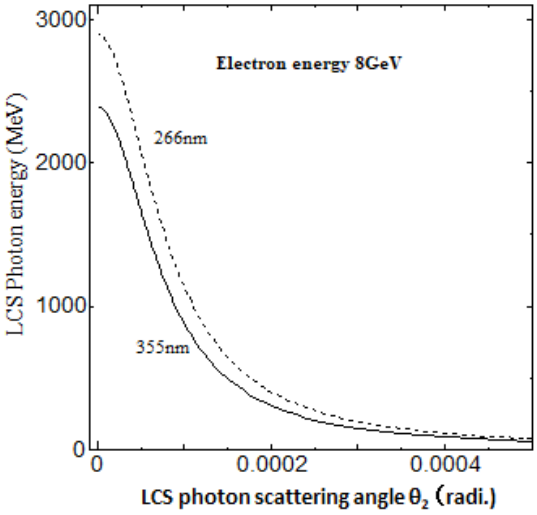

Figure 3: *LCS photon energy on a function of the scattering angle θ_2 with the* 8 GeV *electron and* 266 nm *(dashed line) and* 355 nm *(solid line) wavelength laser. (SPring-8 LEPS beamline case)*

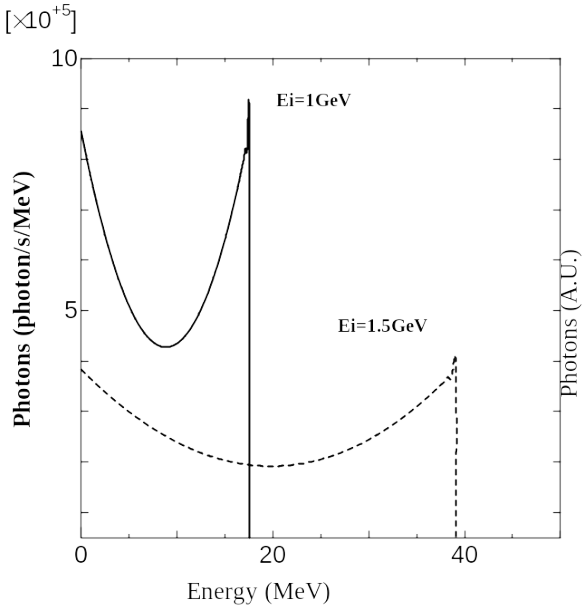

Figure 4: *LCS spectrum at the NewSUBARU cases by using* $1.064\,\mu$m *(YAG) wavelength laser photons. Solid and dashed lines indicate the spectra using* 1.5 GeV *and* 1.0 GeV *electrons.*

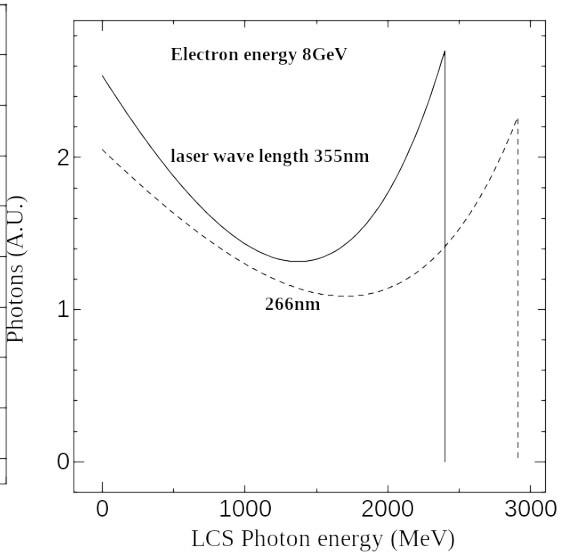

Figure 5: *LCS photon spectrum at the SPring-8 cases. Solid and dashed lines indicate the spectra using* 355 nm *(Paladin) and* 266 nm *(Semiconductor +BBO) wavelength laser photons.*

As shown in Figs.4 and 5, LCS photons are a unique continuous spectrum that is the maximum peak intensity at the maximum energy in corresponding to θ_2=0 degrees. The direct measurement data of LCS spectrum using 350 nm laser photons at SPring-8 LESP beamline is shown in Fig.6 by using PWO detector including calculation data of 350 nm and 200 nm laser cases. The measurement data show in good agreements with the calculations.

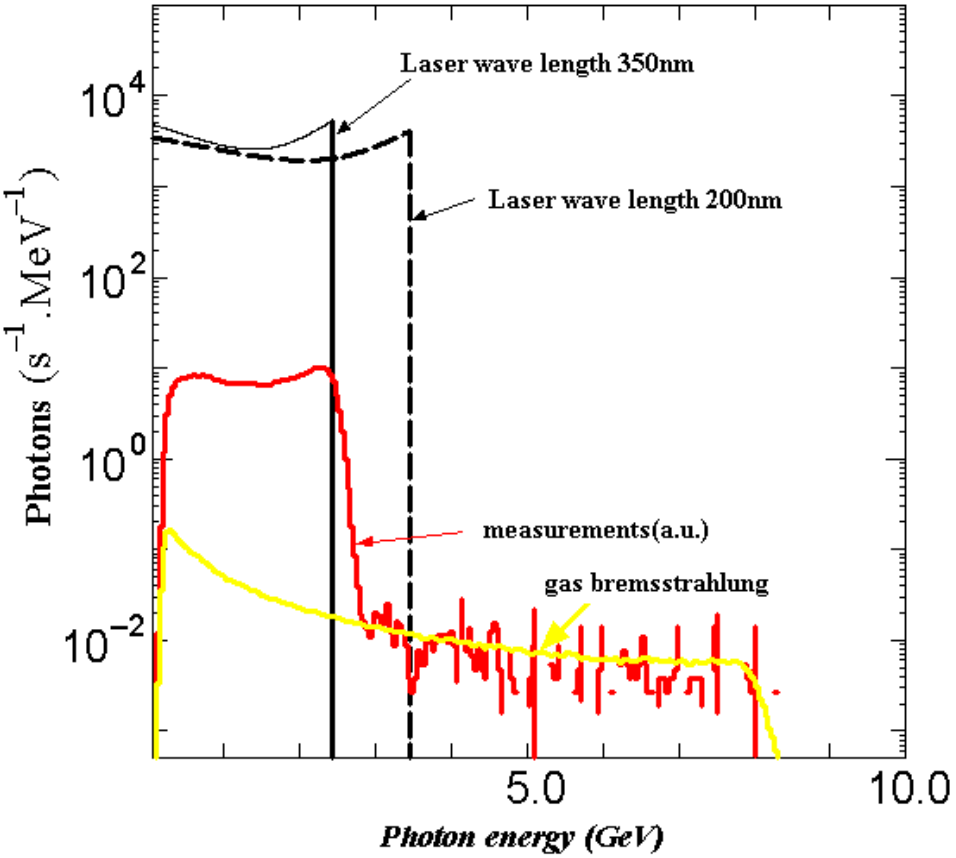

Figure 6: *Measurement data of LCS photon spectrum by using PWO detector at SPring-8 LEPS beamline [16]. Solid red line shows the measurement data of LCS photon with a* $350\,\mathrm{nm}$ *laser and yellow line indicates the measurement data of the gas bremsstrahlung. Solid and dashed lines show the LCS photon calculations with* $350\,\mathrm{nm}$ *and* $200\,\mathrm{nm}$ *laser photon,respectively.*

There are two methods to obtain the quasi mono-energy photons: one is to confine the scattering angle by using collimators and the other is to measure the loss energy of the electron ($E_i - E$) that is connected to the LCS photon energy with one to one relationship by using tagging counters. In the case of using collimators, the emittance, especially electron beam divergence of the accelerated electrons is very important because the divergence strongly connects to the collision angle and the scattering angle. Figure 7 shows the simulation results of collimated LCS spectra depending on the electron beam emittance of the NewSUBARU with the electron energy of $0.982\,\mathrm{GeV}$ and the head-on laser wave length of $1.064\,\mu\mathrm{m}$ by using EGS5 [17] under the assumption of Gaussian for the beam emittance. The aperture size of LCS photons that means takeoff angles from 0 degrees to the scattering angles θ_2 is fixed by collimators to $0.1\,\mathrm{mrad}$. As shown in Fig.7, the spectrum of the collimated LCS photon beam is strongly affected by the electron beam divergence, and the shape of the quasi mono-energy spectrum is worse in association with worse of the electron beam divergence. In contract, electron beam size has no effect on the spectrum. In the case of changing the collision angle, θ_1 , the shape of the collimated LCS photon beam is changed as well as the peak energy. Figure 8 shows the LCS photon spectra dependence on the collision angles from head-on to right and its collimated LCS photon beam with the aperture size of $0.05\,\mathrm{mrad}$. In this case, the electron energy and laser wave length are $3.5\,\mathrm{GeV}$ and $1.064\,\mu\mathrm{m}$, respectively. As shown in these figures, the collimated LCS photon energy can be variable easily in changing the collision angle, however the collimation methods have a limitation in obtaining a good quasi mono-energy LCS photons in the case of increasing the energy.

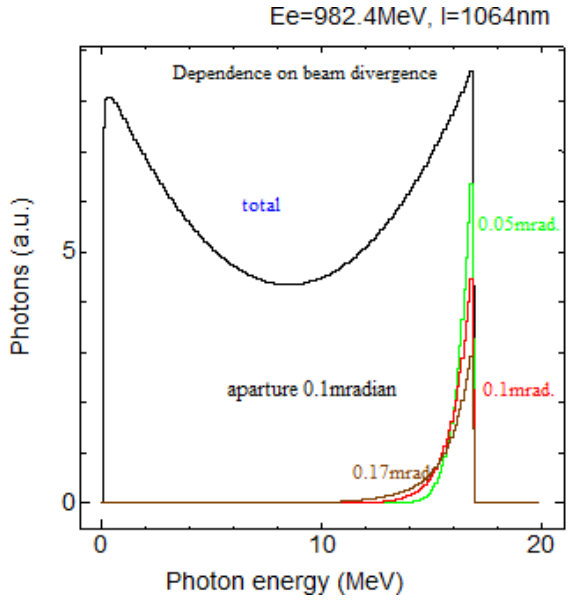

Figure 7: *Collimated LCS photon spectra depending on electron beam divergences(green line; horizontal electron divergence of* $0.05\,\mathrm{mrad}$ *(1*σ*), red;*$0.1\,\mathrm{mrad}$*, ocher;* $0.17\,\mathrm{mrad}$*) . The vertical divergence is fixed to* $0.048\,\mathrm{mrad}$*.*

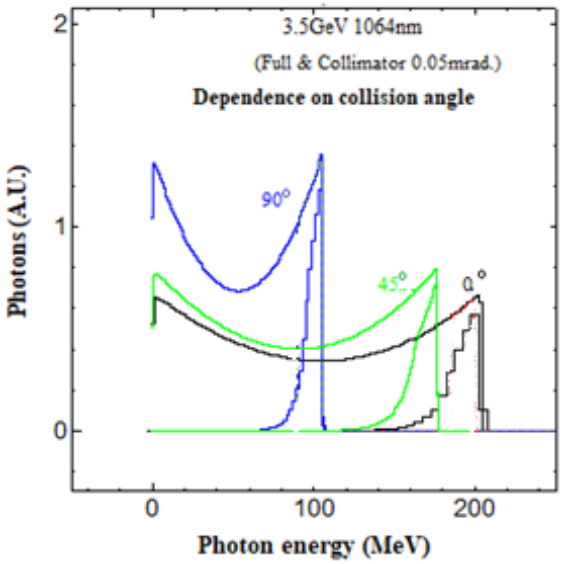

Figure 8: *LCS photon beam dependence on collision angles. (Black line; collision angle* $\theta_1 = 0$ *deg., Green;* $\theta_1 = 45$ *deg. Blue;* $\theta_1 = 90$ *deg. Each stair is collimated LCS photon with the aperture size of* $0.05\,\mathrm{mrad}$*.*

As mentioned above, the energy of LCS photons can be measured by using tagging system to measure the energy of scattered electrons with coincidence to the LCS photons. To measure the scattered electron energy, we usually measure the position of the electron passing through the bending magnet which lies the nearest downstream of the collision point. Figure 9 shows the schematic drawing of the SPring-8 LEPS case with the magnetic field of the bending magnet of $0.693\,\mathrm{Tesla}$ and the length of $2.77\,\mathrm{m}$. The electron trajectory is shown in the above of the figure (laser off case) and the tagging counter which made of plastic and fiber scintillation counters with the size of $2\,\mathrm{mm}$ pitch was set outside the trajectory. In the case of the laser on, the collision electron losses the equivalent energy of the LCS photon and the trajectory after passing through the bending magnet is shifted to the inside of the stored electrons accordingly so that the LCS photon energy can be obtained to measure the position of the scattered electron with the coincidence counting by using the tagging counter. Figure 10 shows the simulation results of tagged LCS photons by using EGS5 with $8\,\mathrm{GeV}$ electrons and $350\,\mathrm{nm}$ laser photons. This figure shows two electron divergences cases, one is the horizontal divergence of σ_u = $8.8\,\mu\mathrm{rad}$ and the vertical divergence of σ_v = $1\,\mu\mathrm{rad}$ (blue lines), and the other is the σ_u =$92.1\,\mu\mathrm{rad}$ and σ_u =$1\,\mu\mathrm{rad}$ (green lines). To compare two methods, the collimated LCS photon spectra are also indicated with the aperture size of $0.05\,\mathrm{mrad}$ and $0.1\,\mathrm{mrad}$. The solid lines with the numbers show the LCS photons with coincidence to the tagging counters. The tagging counters were set from LCS light axis to $16.8\,\mathrm{cm}$ distance with $2\,\mathrm{mm}$ pitch, for example No.2 counter sets 16.4 to $16.6\,\mathrm{cm}$ distance from the LCS photon axis, and No.5 is from 15.8 16 0cm. As shown in the figure, the spectrum of LCS photons with tagging system is almost independent of the electron beam divergence and a good quasi mono-energy spectrum can be obtained. On the other hand, it is impossible to obtain the mono-energy LCS photons by using collimator system in the high energy region. In the case of the very bad divergences, σ_u = $170\,\mu\mathrm{rad}$ and σ_v = $48\,\mu\mathrm{rad}$, the tagging LCS spectra are shown in Fig.11 to investigate the effect of the divergence to the spectrum. As shown in the figure, the tagged LCS photon spectra are not strongly sensitive for electron divergences and the LCS spectra with collimated system are sensitive clearly in comparison with the results as shown in figure 10.

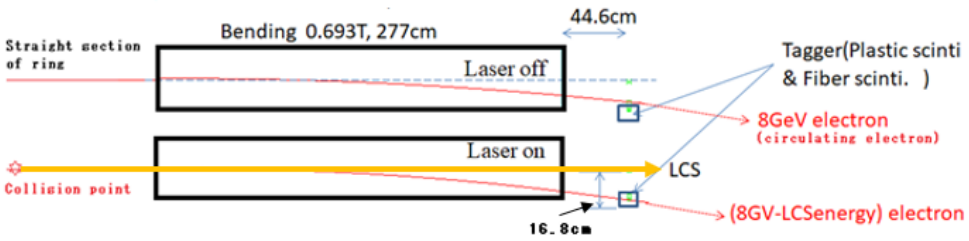

Figure 9: *Schematic diagram of LCS production using tagging system. The energy of stored electron is* 8 GeV *and the wavelength of optical laser is* 350 nm*. The magnetic field strength of the bending magnet is* 0.693 Tesla *with* 277 cm *length. The tagging counter is set at the* 44.6 cm *downstream from the edge of the bending magnet.*

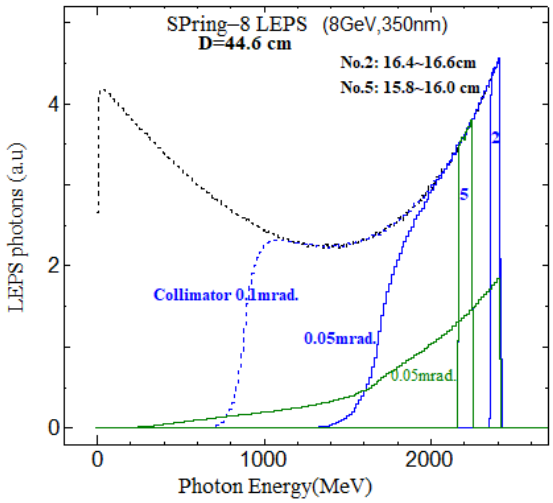

Figure 10: *Simulation results of LCS photon spectra with tagging system and collimator system depending on the electron beam divergence. Blue lines show the case of* σ_u =8.8 μrad *and* σ_v =1 μrad*, and green lines are* σ_u =92.1 μrad *and* σ_v =1 μradian*. The lines with aperture sizes show the collimated LCS photon spectra. The solid lines with the numbers show the tagged LCS spectra with the tagger counters which set on the different distance from the light axis (No.2;* 16.4 16 6*cm, No5;* 15.8 16 0*cm).*

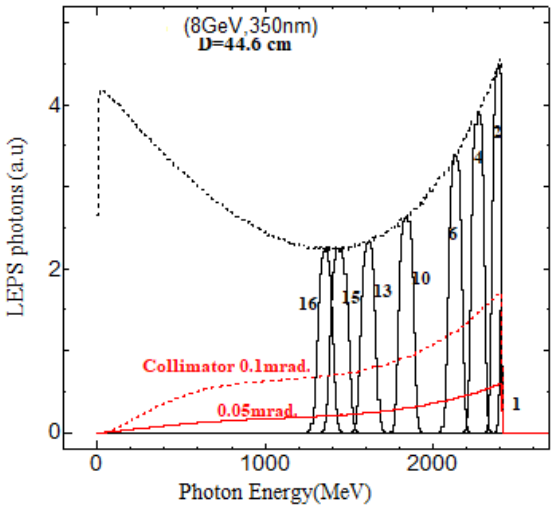

Figure 11: *Simulation results of LCS photon spectra with tagging system and a very bad divergence (*σ_u =170 μrad *and* σ_v =48 μrad *) case (virtual case). Solid lines with the numbers are tagged LCS photon spectra. The number means the tagging counter number which locates the distance from LCS light axis to 16.8cm with 2mm pitch, for example, No.1 counter locates at the distance from* 16.6 16 8*cm, No.2 is from* 16.4 16 6*cm, and No.16 is* 13.6 13 8*cm. The solid and dotted red lines show the collimated LCS photons with* 0.05 *and* 0.1 mrad*, respectively.*

Another great advantages of LCS photons are to be available of high energy polarized LCS photons by using a polarized optical laser and ultra-short pulse (sub or pico-second) LCS photons [18].

3 Present status of LCS beamlines

The energy of LCS photon depends on the wavelength of optical laser directly. Many lasers are employed to produce LCS photons and listed up in Table1. Many LCS photon beamlines have been constructed so far. However, LCS photon beamlines which can produce photons with high energy have not been so much. Main LCS photon beamlines with high energy (over 10 MeV) are listed in Table 2. Only three facilities, NewSUBARU, SPring-8 and Duke Univ., are now under operation routinely. SLEGS are now under construction.

Table 1: *Optical laser for using LCS photon production*

Laser	Wavelength	Energy
CO_2	10.59 mm	0.1171 eV
$NdYuO_4$	1.064 mm	1.165 eV
Paladin	0.355 mm	3.492 eV
UV	0.200 mm	6.199 eV
Semiconductor + BBO	0.266 mm	4.661 eV
Ti : Sa	0.8 mm	1.550 eV
FEL	$<$0.103 mm	$>$12.04 eV

Table 2: *Main LCS photon beamlines (LCS photon energy $>$10 MeV)*

	Legs (NSLS) BNL USA [1]	**Graal (ESRF) Grenoble EU[2]**	**NewSUBARU Univ.of Hyogo Japan[3]**	**LEPSI,II Osaka Univ. RCNP, Japan[4]**	**TUNL-HIGS Duke Univ. USA[19]**	**SLEGS (SSRF) Shanghai China[20]**
LCS photon energy (MeV)	180-300	300-1500	4-73	1500-2900	1-100	0.4-550
Electron energy (GeV)	2.5	6	0.5-1.5	8	0.21-1.2	3.5
Energy discrimination	Tagging	Tagging	Collimation	Tagging	Collimation & Tagging	Tagging
Status	Shutdown	Shutdown	Operating	Operating	Operating	Under const.

4 Application of LCS photon beam to radiation safety researches and others

To construct the high-energy electron machines including synchrotron radiation facilities, one of the crucial issues is the radiation protection such as the estimation of leakage dose distribution and induced activities. Sometimes the design of the radiation shielding restricts the machine designs. To investigate the physical phenomena of neutrons due to photo-nuclear reaction is important because of insufficient experimental data in addition to its strong attenuation and cause to activate the components. The double differential cross section data that fully describe energy and the angle of the emitted neutrons are required to design and estimate the shielding and leakage dose distributions. However, there are few experimental data of the double differential cross section until now. In addition, there are some different in the cross-section data that employed in commonly used Monte Carlo codes such as PHITS [21] and FLUKA [22] , especially for low-Z nuclides [23] . Emitted neutrons due to polarized photons distribute anisotropic obviously [24] , however neutron energy spectra have not previously been measured precisely with linearly polarized photons. It is desired to obtain the experimental data of photo-neutron angular and energy distributions with polarization effects.

To investigate the double differential cross section of neutron production due to photo-nuclear reaction systematically for giant dipole resonance and quasi-deuteron disintegration regions, we have started to measurethe neutron spectra at the several directions from the photonuclear reaction with the linearly and circularly polarized photons using liquid scintillation counters in collaboration with KEK, JAEA, and NewSUBARU. Figure

12 illustrates the NewSUBARU BL1 beamline and Fig.13 shows the photo at the optics hutch2 during the experiments. A YAG (Nd:YVO4) laser is led to the straight section of the storage ring and then collided with stored electrons to produce LCS photons. Two collimators are employed to define the LCS photon spectra for the experiments. The intensities of LCS photons have been measured by a GSO scintillation detector and monitored by a thin plastic scintillation detector (PLS). The pulse height distributions of GSO for the maximum

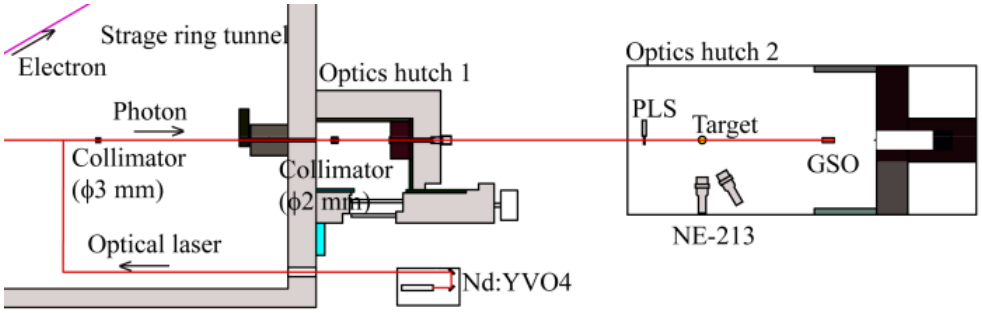

Figure 12: *Schematic illustration of NewSUBARU BL1 beamline. PLS and GSO indicate the plastic and Gadolinium Silicate scintillation detectors, respectively [14].*

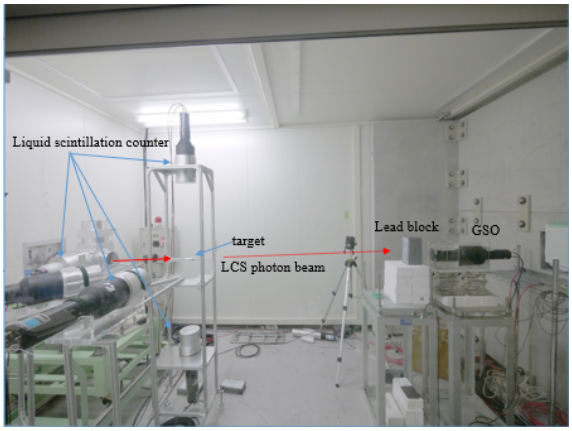

Figure 13:*Photo of the experimental setup in the hutch of the NewSUBARU BL1beamline.*

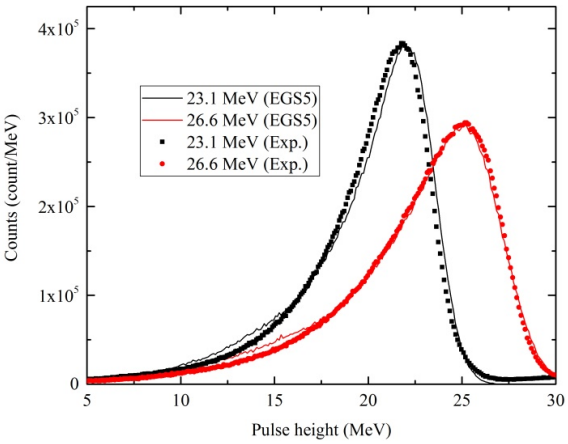

Figure 14: *Pulse height spectra of GSO and the simulations using EGS5 for LCS photons with the maximum energy of* 23.1 *and* 26.6 MeV *[14].*

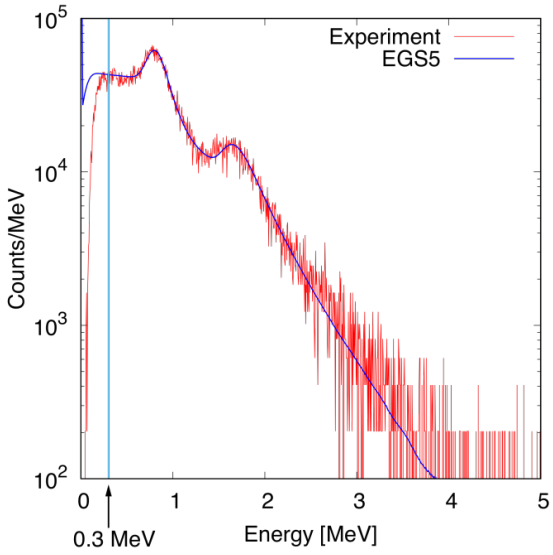

Figure 15: *Output of PLS and the simulation using EGS5 [14]*

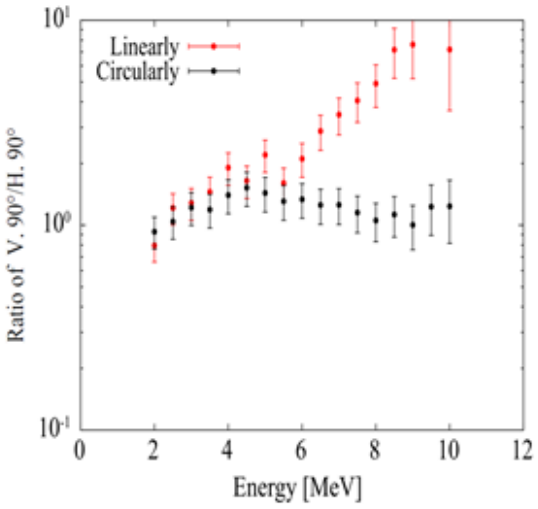

Figure 16: *Polarization dependence on the emitted photo-neutron energy. (Gold target, V90 and H90 are same direction of the linearly polarization and perpendicular direction. [15]*

photon energy of 23.1 and 26.6 MeV are shown in Fig.14 with the EGS 5 simulations. The size of the GSO detector is 76 mm square with 180 mm in length and enough to full stop of the LCS photons. The PLS outputs with the EGS5 simulation are shown in Fig.15 and calibrated to use the monitor during the experiments in comparison with the GSO outputs. The separation of photons and neutrons have been performed by using time of flight and pulse shape analysis methods of the liquid scintillation counters with the sizes of 127 mm in diameter and 127 mm long. The detailed configuration of the experiments was reported in reference [14] and [15] . One of the results is shown in Fig.16 with the case of a gold target. In this case, V90^o and H90^o are the same direction of the linearly polarization vector from the target and the perpendicular direction, respectively. As shown in the figure, the photo-neutrons with the energy of less than about 4 MeV are independent of photon polarization and the photo-neutrons with the energy of higher than about 4 MeV depend on the polarization. This means that photo-neutrons consist of two groups, one is evaporated and the other is direct production process component. The emitted distribution of the evaporate component of photo-neutrons is independent of photon polarization and the direct component depends on photon polarization. The distribution of emitted photo-neutron due to direct process can be expressed as $\{\ a + b \cdot \cos(2\theta)\ \}$, where a and b are the constant numbers for gold and θ is the angle between the photon polarization vector and the emitted direction of the photo-neutron [25].

Other researches using LCS photons are, for examples, investigation of Penta quarks and Kaon physics using from 1.3 to 2.9 GeV polarized LCS photons at SPring-8 LEPS-1 and II beamlines [5], nondestructive inspection for nuclear materials using nuclear resonance fluorescence with LCS mono-energetic photons for nuclear security at the transport section like as harbors or airports [7], using high mono-energy photon beams, feasibility study to produce exclusively radioisotopes such as Molydenum-99/Technetium-99m [8], and detector calibration using polarized photons such as HARPO detector for the investigation of cosmic rays [6], and so on.

5 Summary

LCS photons have a quite unique spectrum with some feature points such as the high usability and changeability of high energy photons and the photon polarization. The LCS beamline will be grown in use in combination with the improvement of accelerator techniques and powerful optical laser techniques. To obtain quasi mono-energy LCS photons, two methods were discussed. For LCS collimation systems, the accelerated electron emittance, especially the divergence is sensitive on shaping the spectrum and important to simulate it with precisely. For the scattering electron tagging systems, the coincidence spectrum of LCS is not sensitive strongly

and the system must be employed in the case of higher energy LCS photon experiments.

Researches using LCS photons have been overviewed mainly with viewpoints of radiation safety. In the reviews, LCS photons showed to be useful to measure photo-nuclear reaction cross sections with the effect of photon polarization. The emitted photo-neutrons consist of two components, one is photo-neutrons due to evaporation process and the other is photo-neutrons due to direct process. The measured data shows the emission distributions of the evaporate component and the direct component are isotropic and anisotropic under the polarized photon irradiation, respectively. However, these polarization effects are not included in common Monte Carlo codes such as FLUKA and PHITS. It is desired for these codes to improve these functions.

References

[1] A.M.Sandorfi et al., *High Energy Gamma Ray Beam from Compton Backscattered Laser light*, IEEE Transactions on Nuclear Science V30 p3083-3087 (1983)

[2] J.P.Bocquet et al., *GRAAL: a polarized γ-ray beam at ESRF*, Nuclear Physics A V622 pc124-c129(1997)

[3] Yoshihiro Asano, Takao Nakano, Tomoaki Hotta and Yuji Ohashi, *Shielding Design Calculations for Laser Electron Photon Beamline of SPring-8*. J. Nuclear Science & Technology supplement 1 p217-221 (2000)

[4] Yoshihiro Asano, Shuji Miyamoto and LEPS-II collaboration *Shielding Design of Laser Electron Photon beamlines at SPRING-8* , Progresses in Nuclear Science and technology 4 p252-256(2014)

[5] T.Nakano et al., *Evidence for a Narrow S = +1 Baryon Resonance in Photoproduction from the Neutron* Phys. Rev. Lett. 91, 012002 (2003)

[6] P.Gros, et al., *Performance measurement of HARPO: A time projection chamber as a gamma-ray telescope and polarimeter*, Astroparticle Physics 97 p10-18 (2018)

[7] T.Hajima, N.Kikuzawa, N.Nishimori, T.Hayakawa, T.Shizuma, K.Kawase, M.Kando, E.Minehara, H.Toyokawa, and H.Ohgaki, *Detection of radioactive isotopes by using laser Compton scattered gamma ray beams*, NIM A 608 s57-s61 (2009)

[8] Hiroyasu Ejiri, Tatsushi Shima, Shuji Miyamoto, Ken Horikawa, Yasuhisa Kitagawa, Yoshihiro Asano, Schin Date, and Yuji Ohashi, *Resonant Photonuclear Reactions for Isotope Transmutation*, Journal of the Physical Society of Japan 80 (2011) 094202

[9] A.H.Compton, Physics Review V21 p483 (1923)

[10] E.H.Feenberg and H.Primakov, Physics Review V73 p459 (1948)

[11] R. H. Milburn: *Electron scattering by an intense polarized photon field,* Phys. Rev. Lett., 10 75-77 (1963)

[12] F. R. Arutyunian and V. A. Tumanian: *The Compton effect on relativistic electrons and the possibility of obtaining high energy beams,* Phys. Lett., V4 176-178 (1963)

[13] O. F. Kulikov, Y. Y. Telnov, E. I. Filippov and M. N. Yakimenko: *Comptom effect on moving electrons*, Phys. Lett., V13 p344-346(1964)

[14] Toshiro Itoga, Hiroshi Nakashima, Toshiya Sanami, Yoshihito Namito, Yoichi Kirihara, Shuji Miyamoto, Akinori Takemoto, Masashi Yamaguchi, and Yoshihiro Asano, *Measurement of neutron energy spectra for Eg*=23.1 *and* 26.6 MeV *mono-energetic photon induced reaction on natC using laser electron photon beam at NewSUBARU*, 13^{th} International Conference on Radiation Shielding & 19^{th} Topical meeting of the Radiation Protection and shielding Division of the ANS, ICRS-13 & RPSD-2016 Paris, France Oct.3-6 2016

[15] Yoichi Kirihara, Toshiro Itoga, Toshiya Sanami, Hiroshi Nakashima, Yoshihito Namito, Shuji Miyamoto, Akinori Takemoto, Masashi Yamaguchi, and Yoshihiro Asano, *Measurement of neutron spectra for photonuclear reaction with linearly polarized photon*, 13^{th} International Conference on Radiation Shielding & 19^{th} Topical meeting of the Radiation Protection and shielding Division of the ANS, ICRS-13 & RPSD-2016 Paris, France Oct.3-6 2016

[16] Y.Asano, T.Matsumura, R.Chiba, T.Hashimoto, A.Miura, H.Shimizu, Y.Tajima, and H.Y. Yoshida, *Measurement of Gas bremsstrahlung at the SPring-8 Insertion Device Beamline using PWO scintillator.* Nucle. Inst. & Methods Physics Research A 451 p685-696 (2000)

[17] Hirayama H, Namito Y, Bielajew AF, et al. : *THE EGS5 CODE SYSTEM*, SLAC-R-730 and KEK Report 2005-8, Stanford Linear Accelerator Center and High Energy Accelerator Research Organization, 2005

[18] Y.Taira, M.Adachi, H.Zen, T.Tomikawa, M.Hosaka, Y.Takashima, N.Yamamoto, K.Soda, M.Katoli, *Feasibility study of ultra-short gamma ray pulse generation by laser Compton scattering in an electron storage ring*, Nuclear Instruments and Methods in Physics research A 637 pS116-119 (2011)

[19] http://www.tunl.duke.edu/facilities

[20] G.Wei, et al., *Shanghai laser electron gamma source and its applications*, Chinese Physics (HEP & NP) V32 Sup.-II p190-193 (2008)

[21] Sato T. Niita K. Matsuda N. Hashimoto S. Iwamoto Y. Noda S. Ogawa T. Iwase H. Nakashima H. Fukahori T. Okumura K. Kai T. Chiba S. Furuta T. Sihver L. Particle and Heavy Ion Transport Code System PHITS,version 2.52:J.Nucl. Sci.Technol. 50: 913-923;2013

[22] Ferrari A. Sala P.R. Fasso A. Ranft J. *FLUKA: a multi-particle transport code*: CERN 2005-10 (2005),INFN/TC_05/11,SLAC-R-773 2005

[23] Yoshihiro Asano, *Estimation of airborn Radioactivity induced by 8GeV class electron LINAC accelerator* , Health Physics 113(4) p237-245 (2017)

[24] K.Horikawa et al., Physics Letters B 737 109 (2014)

[25] Yoichi Kirihara, Hiroshi Nakashima, Toshiya Sanami, Yoshihito Namito, Toshiro Itoga, Shuji Miyamoto, Akinori Takemoto, Masashi Yamaguchi, and Yoshihiro Asano, *Neutron emission spectrum from gold excited with* $16.6\,\mathrm{MeV}$ *linearly polarized monoenergetic photons* to be published in J. Nuclear Science and Technology.

Calculation of High Energy Neutron Corrections for Albedo Dosimeters at BESSY

A. Bundels, K. Ott

Helmholtz-Zentrum Berlin, BESSYII, 12489 Berlin, Germany
October-2019

Abstract

At synchrotron light sourceslike BESSYII a considerable part of the exposition consists of high energy neutrons with E $>10\,\mathrm{MeV}$. The detection of neutrons with common Leake or Anderson-Braun monitors require the thermalization of neutrons resulting in a high energy limit of 10 - $20\,\mathrm{MeV}$. We found solutions for this problem in our development of lead moderators that increase the upper detection limit to several GeV [1] and by the calculation of correction factors for our neutron spectra [2, 3].
The correction factor between 2 and 3 (depending on shielding) makes it necessary to consider the situation for Albedo-dosimeter too. These dosimeters which are in usage for personal dosimetry at BESSYII also require thermal energies for neutron detection.
In contrast to the ambient dosimetry where the fluence to dose conversion coefficients H*(10) [4] have been calculated up to the TeV range [5], the conversion coefficients Hp(10) for the personal dosimetry have been tabulated only up to $20\,\mathrm{MeV}$ [4] and have been calculated more recently by Olsher et al [6] up to $250\,\mathrm{MeV}$.
We present in this work our approach to calculate the correction factors for Albedo-dosimeters using FLUKA [7,8] calculations of the neutron spectra in the experimental hall at BESSYII and PTB neutron reference spectra for neutron sources [9] to calculate the Albedo-dosimeter response function [9] from relative in absolute units.

1 Introduction

At BESSYII, researchers from all over the world carry out research and experiments on approximately 50 beamlines. For this purpose, state-of-the-art spectroscopy and microscopy methods are available. The users can also conduct time resolved studies very short light pulses ($3\,\mathrm{ps}$) during the weeks of low-alpha mode.

With the planned conversion of BESSYII to a variable pulse length storage ring (BESSY VSR [10]), users will be able to choose between short ($1.5\,\mathrm{ps}$) and longer ($15\,\mathrm{ps}$) pulses for each experiment. To ensure the protection of radiation exposed persons in Germany, the Radiation Protection Ordinance and the Radiation Protection Law apply. At BESSYII Albedo-dosimeters are used to comply with these legal regulations and to monitor the personal doses.

Albedo - dosimeters detect neutrons of thermal energies. This raises the question up to which energies the neutrons can still be decelerated to thermal energies by a moderator.

This situation is similar to the ambient dosimetry because the common Anderson-Brown or Leake monitors also detect neutrons which are thermalized by a moderator. The maximum neutron energy of Anderson-Brown type neutron monitors used at BESSYII is $10\,\mathrm{MeV}$. If the energies are higher the neutrons can no longer be decelerated to the thermal detection energy in the counter tube by the moderator present in the monitor. The moderator is made polyethylene, and borated polyethylene inside to reduce the flux of thermalized neutrons.

The neutron spectra in the experimental hall has a broad maximum at $100\,\mathrm{MeV}$ with a similar height to the one at $1\,\mathrm{MeV}$. We calculated the correction factor folding the neutron spectrum at BESSYII with the response function of our neutron monitors. The resulting measurement errors outside the shielding walls are considerable

[3]. Because of the correction factor of about three we developed a lead moderator that enabled our Anderson-Brown type monitor to extend its measurement range to several GeV [1].

Since neutron detection with Albedo-dosimeters require thermal energies as well it can be assumed that we also need a correction factor for them. The calculation of a correction factor for Albedo-dosimeters we will present in this paper.

2 Interaction of neutrons

When neutrons penetrate matter, they interact exclusively with the atomic nuclei. Photons, on the other hand, can interact with the atomic shells of matter due to ionisation. Since the range of the nuclear forces is very small, the neutrons must be very close to the atomic nuclei.

A measure for the interaction probability of a neutron is the cross section. It is the probability that a certain interaction takes place between an incident neutron and another particle.

Neutrons can conduct nuclear reactions e.g. (n,γ), (n,p), (n,α) or even fission processes as well as elastic scattering processes which are used for the moderation. The most effective energy reduction occurs in particular with the hydrogen nuclei present in the body because of the about same mass of neutrons and protons. Within the moderators used for neutron dosimetry neutrons could be moderated down to thermal energies.

The energy loss of the neutrons after elastic scattering is described by the relative energy loss factors f eq. (1) for isotropic scattering.

$$f = \frac{E_n}{E_0} \tag{1}$$

E_0 is the energy before the impact and is the energy after the impact.

A quantity related to the energy loss factor is the so called lethargy $L = \ln f$. The presentation of neutron spectra is often given in lethargy units. In that case the spectra are divided by $L = \ln E_{i+1}/E_i$ with E_{i+1}/i as energy limits of the respective energy bin.

3 Ambient neutron dosimetry

For the measurement of the ambient dose at BESSYII an ionization chamber and a neutron monitor (Biorem) are used. They are located in the experimental hall close to the front-ends, on the tunnel roof of both storage ring and booster tunnel and around the booster shielding wall.

We investigated the measurement errors of our ambient neutron dosimetry earlier [2, 3] and calculated correction factor for the high energy part of our neutron spectra. The results are summarised in fig.1.

The lower curve shows the neutron fluence spectrum calculated for the BESSYII experimental hall behind a 1 metre thick concrete shielding in lethargy units, derived from the Monte Carlo transport code FLUKA [7, 8]. Three peaks are clearly visible: at thermal energies ($25\,\mathrm{meV}$), at about $1\,\mathrm{MeV}$ (giant resonance neutrons) and at $100\,\mathrm{MeV}$ (neutrons by quasi deuteron fission and photo pion production). In the upper part of fig.1 the response function of the Biorem is plotted, the energy limits of this curve are $25\,\mathrm{meV}$ and $10\,\mathrm{MeV}$. If we compare this with the energy spectrum we can see that the high energy part cannot be detected by this neutron monitor. Also in the upper part of fig.1 the H*(10) fluence to dose response function with its expansion by Pelliccioni is given. Folding the spectrum with fluence to dose curve results in the true H*(10) value, folding the spectrum with the response function results in the measured dose. From the quotient of these numbers we get the correction factor of 2.98 for this spectrum.

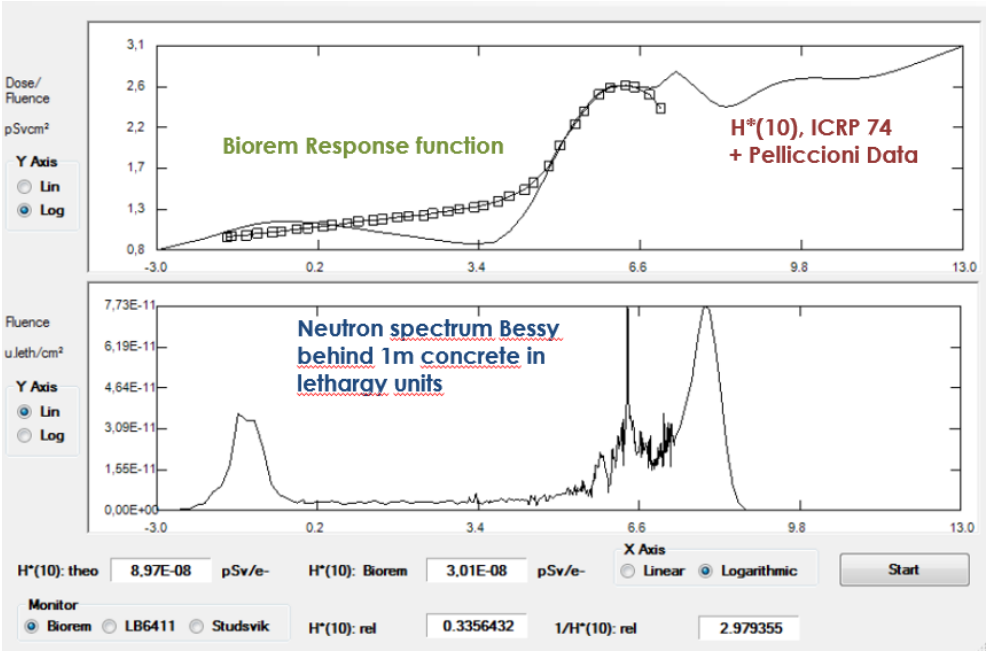

Figure 1: *Correction factor from folding neutron spectrum. Upper curves: Squares, BIOREM response function and fluence to dose conversion function H*(10 [4])and Pelliccioni data[5]. Lower curve: Neutron spectrum BESSYII behind 1m concrete in lethargy units.*

Due to the introduction of the top-up mode it is also possible that neutrons through the open front ends during the injections are detected by the neutron monitors close to the openings. In that case the usage of the correction factor for the high energy neutrons would lead to an overestimation because a part of these neutrons are not moderated by the concrete wall. Therefore we developed a neutron moderator (yellow lead cylinder in fig. 2) to increase the high detection limit from $10\,\mathrm{MeV}$ up to the GeV range and tested it successfully at the CERN reference field [1].

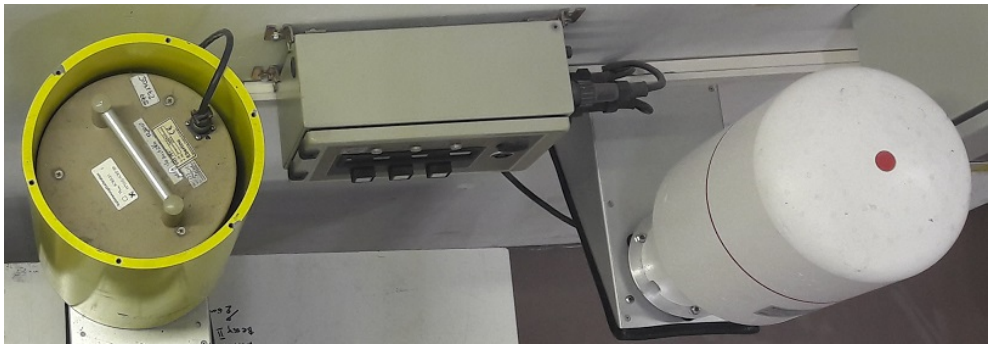

Figure 2: *Measurement system of ambient dose. Left: BIOREM neutron monitor with neutron moderator. Right: ionization chamber.*

The usage of the lead moderators increased the measured annual neutron doses on the average by a factor 2.5 which is in acceptable agreement with the calculated correction factor (see fig.1). Because both ambient and personal dose measurements uses thermalized neutrons it follows that we need a correction factor for personal neutron dosimetry with Albedo-dosimeters too.

Table 1: *Overview reaction data for lithium and boron*

Nuklide	**Reaction**	**thermal capture cross section [b]**	bf Detection
^{6}Li	^{6}Li(n,α)^{3}H	941	Neutron and Gamma
^{10}B	^{10}B(n,α)^{7}Li	3838	Neutron and Gamma
^{7}Li	^{7}Li(γ,α)^{3}H	0.0454	Gamma

4 Personal dosimetry

4.1 Albedo-Dosimeter

The Albedo-dosimeters used at HZB are official personal dosimeters and based on thermoluminescence detectors (TLDs). They are sensitive to both neutron and gamma radiation. TLDs consist of lithium fluoride (LiF) doped with Mg and Ti. ^{7}Li is sensitive only for gamma radiation, ^{6}Li can also detect thermalized neutrons by the reaction ^{6}Li(n,α)^{3}H. Therefore TLDs are used as pairs, the neutron dose is determined by subtraction of the gamma dose from the ^{6}Li value which contains both gamma and neutron dose.

The structure of the Albedo-dosimeter is shown in illustrations from 3 to 5. The casing of the Albedo-dosimeters consists of boron plastic. The boron plastic absorbs thermal neutrons via the process ^{10}B(n,α)^{7}Li with a high cross section of reaction, thus largely reducing the flux of thermal neutrons for calibration purposes.

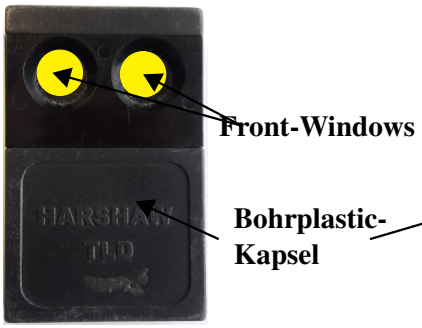

Fig.3 Albedo front

Fig.4 Albedo back

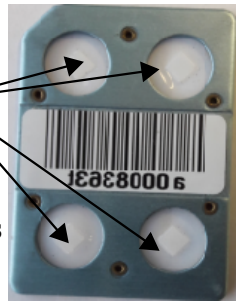

Fig.5 Dectectorcard

Albedo- dosimeters are worn close to the body, at a location suitable of the radiation field (e.g. the chest). On pair of TLDs is facing to radiation field, the other is facing to the body. For the neutrons the body serves as a moderator. The high-energy neutrons are decelerated there to thermal energies, backscattered and then detected by the TLD.

In order to return to the cross section already mentioned above, the isotopes containing the detectors of the Albedo-dosimeters are now considered.

4.2 Calculation of the Albedo response function in absolute values

For the calculation of a correction factor, for the Albedo-dosimeters, we use the same approach as for the calculation of the correction factor for our Anderson-Brown type neutron monitors. However, two problems have to be solved. The fluence to dose conversion coefficients of Hp(10) are defined in the IAEA report [9] only up to 20 MeV, and we have much higher neutron energies at BESSY (like at other synchrotron light sources).

We found these values in the paper from Olsher et al. up to $250\,\mathrm{MeV}$, which we use to produce a fluence to dose conversion curve from the meV range up to $250\,\mathrm{MeV}$.

The second problem is: We have the Albedo response function only in relative units normalized to the maximum [9]. In order to calculate the measured dose, we need it in absolute units.

The spectrum of the neutron source Cf252 has a maximum of about $1\,\mathrm{MeV}$, similar to the maximum of the giant resonance neutron spectrum. We selected for our calculations the Cf252 neutron reference spectrum of the PTB [9] which is also used to calibrate Albedo-dosimeters. In order to obtain reference values for the calculations, we first calculate the true dose eq. (2) by folding the Cf252 spectrum of the PTB with the Hp(10) values [9]

$$H_i = \sum_{i=1}^{N} \phi_i^{Cf252} \cdot H_p \tag{2}$$

with i as index for the energy bin,ϕ as group fluence, H_p as Hp(10) value for this energy bin. For the whole spectrum we receive a true dose value of $270.025\,\mathrm{pSvcm}^2$.

In the next step we calculate the relative measured dose by folding the spectrum with the relative response function:

$$H_m = \sum_{i=1}^{N} \phi_i^{Cf252} \cdot r \tag{3}$$

with r_i as relative response function for this energy bin, the other symbols have the same meaning as above. With this calculation we get the relative measured dose value of 0.09825 for the whole spectrum.

The factor X to calculate the relative units in absolute values is given by

$$X = \frac{H_t}{H_m} \rightarrow R_i = r_i \cdot \tag{4}$$

Inserting the numbers we get the factor X = 270.025/0.09725 = $2776\,\mathrm{pSvcm}^2$.

Altogether we obtain an expression for the dose measured by the Albedo-dosimeters in absolute values:

$$H_m = \sum_{i=1}^{N} \phi_i^{Cf252} \cdot R_i \tag{5}$$

The results are presented in fig. 6. In the upper diagram is plotted the fluence to dose conversion function of the Albedo-dosimeter in absolute values and the Hp(10) fluence to dose conversion function [9] together with the values of Olsher. In the lower diagram the Cf252 neutron reference spectrum of the PTB is plotted in lethargy units. Lethargy units are not used for the folding calculations.

In the two text windows of fig. 6 the values for the true dose (folding spectrum with Hp(10)) and measured dose (folding spectrum with Albedo response function in absolute units) are in very good agreement.

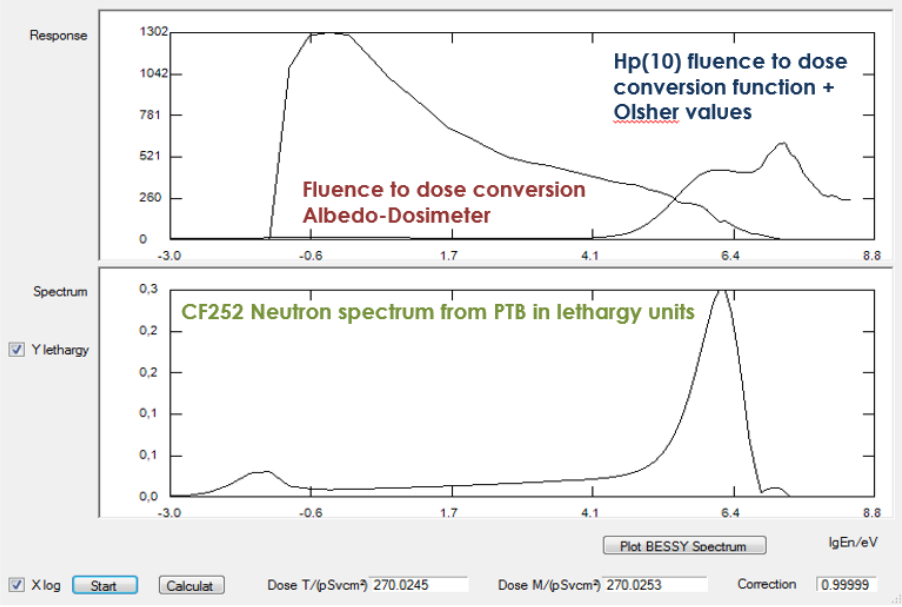

Figure 6: *Application of the proportionality factor X. Upper curves: Fluence to dose conversion Albedo-dosimeter and fluence to dose conversion function Hp(10) including the values of Olsher. Lower curve: Cf252 Neutron spectrum from the PTB in lethargy units.*

4.3 Calculation of the correction factor

We use FLUKA to calculate the neutron spectra at BESSY. This code gives the results in double differential fluence spectra ($\frac{d^2\phi}{dE_i d\Omega}$) values for the respective energy bin. The solid angle $d\Omega$ is used in relation to the boundary area in which the neutrons are counted. The solid angle 2π is used if the neutrons are to be counted from one direction and 4π if they are to be counted from two directions (forward and backward). To get the group fluences we multiply the numbers of the double differential fluence spectra by the energy difference of the bins, the solid angle and divide it by the counting area:

$$\phi_i = \Delta E_i \frac{2\pi}{A} \frac{d^2\phi_i}{dE_i d\Omega} \tag{6}$$

(For our plots ϕ is presented in lethargy units by dividing these numbers through the lethargy intervals)

We calculate now the true dose by folding the neutron spectrum at BESSY with the Hp(10) values including the expansion by Olsher et al. [6] using eq.(2) but instead of the Cf252 spectrum using the group fluence values of the BESSY spectrum eq. (6). The result is given in the text window Dose T in fig. 7. (left red circle)

The measured spectrum we calculate by folding the spectrum with the absolute respones function of the Albedo dosimeters in absolute units eq. (5) using the group fluence values of eq. (6). The result is given in the text window Dose M in fig. 7 (right red circle).

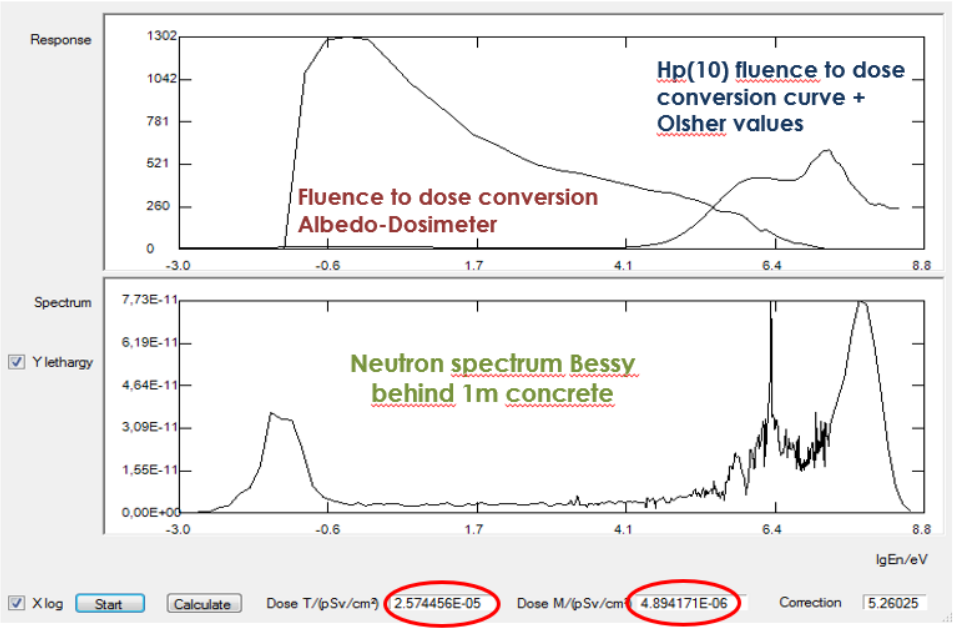

Figure 7: *Calculation of the correction factor for the Albedo-dosimeter. Upper curves: Fluence to dose conversion Albedo-dosimeter and fluence to dose conversion function Hp(10) plus the values of Olsher. Lower curve: Neutron spectrum BESSYII behind 1m concrete.*

The correction factor for the Albedo-dosimeters at BESSYII is the quotient of the true and the measured doses.

$$C_{F_{Albedo}} = \frac{H_t}{H_m} = \frac{2.574456E-05}{4.894171E-06} = 5.26 \tag{7}$$

5 Comparison Correction Factor of Ambient and Personal Doses

For ambient dose, we have obtained a correction factor of 2.98, for the personal dosimetry 5.26.The higher value for the Albedo-dosimeters is a consequence of the higher sensitivity of these to lower neutron energies, which can be seen by if we compare the response function of the Albedo-Dosimeters and the Biorem (fig 7 and fig 1). Based on these results it follows that a new factor is to be defined for the evaluation of the Albedo-dosimeters at BESSYII.

6 Summary

For both our Anderson-Brown type neutron monitors of the ambient dosimetry and the Albedo-dosimeter the high energy detection limit is defined by the ability of the moderators to decelerate neutron down to thermal energy. Therefore the upper detection limit is $10\,\mathrm{MeV}$.

Due to the pulsed beam structure our neutron monitor of the ambient dosimetry show considerable dead time effects which we solved by using faster preamplifiers and the derivation of correction formulas [11].

For the neutron monitors we calculated high energy correction factor [12]. We developed a moderator for our neutron monitors to increase the high energy detection limit from $10\,\mathrm{MeV}$ to several GeV [1]. Based on the resulting correction factor of 2.98 for the neutron monitors and the fact that neutron measurements in personal dosimetry are also carried out detecting thermalised neutrons, we came to the conclusion that we also need a correction factor for our Albedo-dosimeter.

We therefore calculated a high energy correction factor for the Albedo-dosimeters using a similar approach. But the response function of the Albedo-dosimeter had to calculated from relative units to absolute units by

using the Cf252 reference spectrum of the PTB and the fluence to dose conversion coefficient curve Hp(10) [9] that was extended with Olsher values up to $250\,\mathrm{MeV}$. With these calculations we were able to successfully define a new calibration factor of 5.26 for personal neutron dosimetry at BESSYII.

References

[1] M. Caresana, M. Helmecke, J. Kubanak, G.P. Manessi, K. Ott, R. Scherpelz, M. Silari, *Instrument Intercomparison in the High Energy Mixed Field at the CERN-EU Reference Field (CERF) Facility*, Rad. Prot. Dos. 161, 67-72 (2014)

[2] K. Ott, *FLUKA Calculations of Neutron Spectra at BESSY*, Proceedings EPAC (2006)

[3] K. Ott, Y. Bergmann, M. Martin, L. Pichl, *Upgrade of the Neutron Dose Measurement System at BESSY*, Proceedings IPAC (2017)

[4] ICRP publication 74, (New York: Pergamon Press 1996)

[5] A. Ferrari, M. Pelliccioni Rad. Prot. Dos. 77, p.159 (1998)

[6] R. H. Olsher, T. D. McLean, A. L. Justus, R. T. Devine and M. S. Gadd, *Personal Dose Equivalent Conversion Coefficients for Neutron Fluence over the Energy Range of 20 – 250 MeV*, Rad. Prot. Dos. 138, 199-204 (2010)

[7] G. Battistoni, S. Muraro, P.R. Sala, F. Cerutti, A. Ferrari, S. Roesler, A. Fasso, J. Ranft, *The FLUKA Code: Description and Benchmarking*, Proc. of Hadronic Shower Simulation Workshop 2006, Fermilab 6-8 September 2006, M. Albrow, R. Raja eds., AIP conference Proceeding 896, 31-49 (2007)

[8] A. Fassò, A. Ferrari, J. Ranft, P.R. Sala, *FLUKA: A Multi-Particle Transport Code*, CERN- 2005-10 (2005),INFN/TC_05/11,SLAC-R-773

[9] IAEA Techn. Rep. Series 403, IAEA Vienna (2001)

[10] A. Jankowiak et al, *The BESSY VSR Project for Short X-Ray Pulse Production*, Proceedings IPAC (2016)

[11] K. Ott, M. Helmecke, M. Luszik-Bhadra, M. Martin, A. Weber, *Dead Time Effects of Neutron Detectors Due to Pulsed Radiation*, Rad. Prot. Dosi., doi:10.1093/rpd/ncs326 (2012)

[12] K. Ott, Y. Bergmann, M. Martin, L. Pichl, *Measurement Errors and Upgrades of the Ambient Dose Measurement System at BESSY*, Proceedings RADSYNCH (2017)

Save acquisition of sacrificial absorber temperatures at PETRA3 beamline P61

Michael Dressel

Deutsches Elektronen-Synchrotron Notkestr. 85, 22607 Hamburg
October 2019

Abstract

At the PETRA3 beamline P61 a sacrificial absorber is facilitated to detect dangerous leaking of beam through a photon slit. Beam leaking through the photon slit is assumed to heat the sacrificial absorber. The talk outlines the implementation used to acquire the temperature of the absorber and to create signals to the personnel interlock system in a safety oriented way.

1 Concept

At beamline P61 wigglers are used to provide a white x-ray beam to four consecutively ordered experiment areas outlined in figure 1. A set of PS (photon slit), ABS (absorber), BS (beamshutter) is placed in front of every area.

The purposes of the three different shutter elements are:

PS : Adjustable aperture to control and absorb the white x-ray beam. The PS does not possess position switches.

ABS : Sacrificial Absorber, to safely sensor beam in case of PS failure. It is supposed to be hit by beam only in case of failure. It does possess closed and open position switches and two temperature sensors.

BS : Beam Shutter to absorb any stray-radiation. It must not be hit by beam. It possesses closed and open position switches.

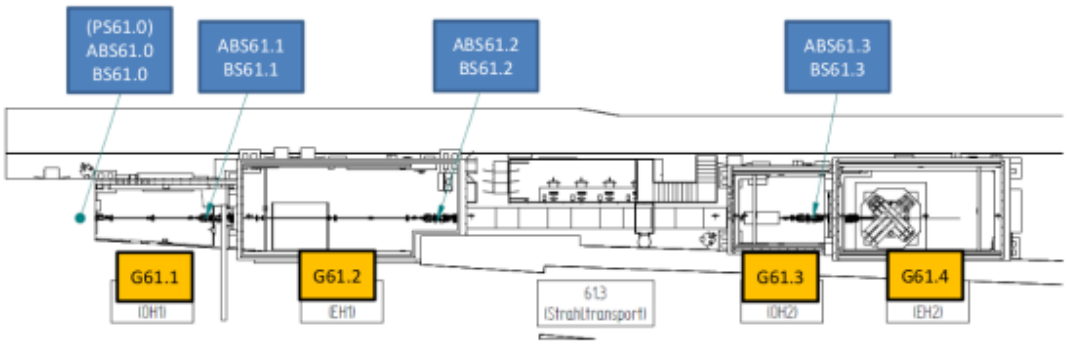

Figure 1: *Outline of P61 experiment areas.*

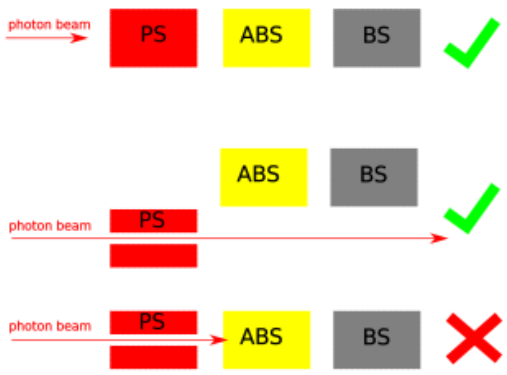

Figure 2: *Schematics of some allowed and forbidden shutter configurations. Green check: allowed, red cross: forbidden.*

Figure 2 schematically shows some allowed and forbidden shutter state configurations.

The PS may only be opened if both ABS and BS are open, allowing beam to be feed into the experiment area downstream. This requires the experiment area to have beam permission granted. Two different types of absorbers (ABS) are used. ABS61.0 used most upstream is connected to the PETRA3 machine vacuum system. In the dangerous case when the wiggler beam unintentionally leaks through PS61.0, it will burn a hole into the ABS61.0. This in turn will lead to a breakdown of the machine vacuum which in turn will dump the PETRA3 electron beam taking area G61.1 (and subsequent areas) into a safe state. Here, this type of absorber is not discussed any further.

The absorbers ABS61.1, ABS61.2 and ABS61.3 are separated from the PETRA3 machine vacuum system and therefore made of a second type of absorber.

The concept of the second type of absorber is based on the assumption that in case the PS fails to absorb the beam completely the leaking part of the beam will heat up the absorber. This concept was earlier investigated at ESRF [1]. Here we will focus on the temperature acquisition and how it is used to provide a safe signal to the personnel interlock system.

The requirements on the absorber are to sense the temperature and to allow for stopping the beam fast enough to not destroy the absorber such that beam would leak through it. This was further detailed to require that the absorber should stay below the melting point temperature of the absorber material (mainly copper) with a safety margin of factor two and furthermore to early detect an increase of temperature by requiring a maximum allowed rise of temperature in time.

Table 1 lists the basic requirements: Additionally thoroughly visual inspection of the absorber has to be per-

maximum absorber temperature $T_{abs,max}$	$500\,^{\circ}\mathrm{C}$
maximum temperature rise ΔT_{max}	$10\,^{\circ}\mathrm{C}/\mathrm{min}$

Table 1: *Basic requirements.*

formed in any case of activation by the temperature acquisition.

The ABS is designed to sense the heating by temperature sensors. The temperature values are acquired in a safety oriented way by a fail-safe PLC (F-SPS). The PLC will revoke the PETRA3 beam permission via the personnel interlock system if temperatures are outside defined limits. This way the PETRA3 beam is dumped and no x-rays are produced anymore.

Calculations [2] used to define limits on the actually measurable temperatures are summarized in section 2.

Some details on the safe temperature acquisition are given in section 3. Conclusions and outlook are given in section 4.

As a further important verification of the safety principle it is demanded to test the system with real wiggler

produced x-ray beam.

2 Heat conduction calculation

The temperature measurement position in the absorber is separated from the absorbing volume. Therefore the limits required from table 1 can not be applied directly but limits for the measurable temperatures have to be defined. Theoretical calculations [2] have been used to find appropriate limits.

Figure 3 shows the geometry of the absorber used in the calculations. In the drawing the beam is incident

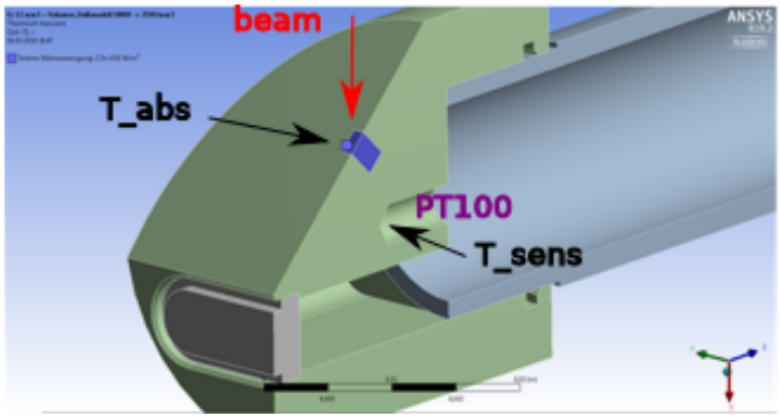

Figure 3: *Geometry used for calculations [2].*

on the absorber bulk from above. Three different volumes $4\,\mathrm{mm}^3$, $8\,\mathrm{mm}^3$ and $12\,\mathrm{mm}^3$ in size are used in the calculations for the conversion of radiation to heat. The position of these volumes is indicated in blue. The temperature calculated for the absorbing volumes is denoted T_{abs}. The position of the PT100 sensors is indicated and the temperature calculated at the PT100 position is denoted T_{sens}.

For heat conduction the ANSYS software and for radiation calculations SPECTRA was used.

2.1 Parameters

The fraction of absorbed beam power calculated by SPECTRA for the three different volumes used are displayed in table 2.

Volume [mm^3]	4	8	12
Absorbed [%]	60	80	90

Table 2: *Absorbed fraction of beam power obtained [2] with SPECTRA.*

The maximum x-ray beam power of $500\,\mathrm{W}$ will occur at the PETRA3 beam current of $100\,\mathrm{mA}$. For the calculations the beam power was varied between $100\,\mathrm{W}$ and $1000\,\mathrm{W}$.

The calculation was used to determine the maximum allowed temperature $T_{sens,max}$ at the sensor position while simultaneously keeping the temperature in the absorbing volume below the required $500\,^\circ\mathrm{C}$.

2.2 Results from calculations

According to the calculations [2], T_{abs} will stay below $500\,^\circ\mathrm{C}$ even in the worst case (the $12\,\mathrm{mm}^3$ absorbing volume) and the highest foreseen x-ray power of $500\,\mathrm{W}$ when the maximum sensor temperature $T_{sens,max}$ is chosen to be $60\,^\circ\mathrm{C}$.

Below two quantities are presented:

- the time t_l it takes to increase the temperature T_{sens} at the sensor position form $30\,°\mathrm{C}$ to the chosen $60\,°\mathrm{C}$ and
- the temperature T_{abs} reached in the volume assumed to absorb the x-ray beam at that moment.

Figure 4 displays t_l and figure 5 T_{abs} for the three different volumes and x-ray beam powers assumed. The $500\,\mathrm{W}$ Limit is indicated by a vertical red line. At $500\,\mathrm{W}$ beam power and $12\,\mathrm{mm}^3$ absorbing volume it takes a little less then $0.5\,\mathrm{s}$ to increase the temperature T_{sens} at the sensor position from $30\,°\mathrm{C}$ to $60\,°\mathrm{C}$. This puts limits on reaction time.

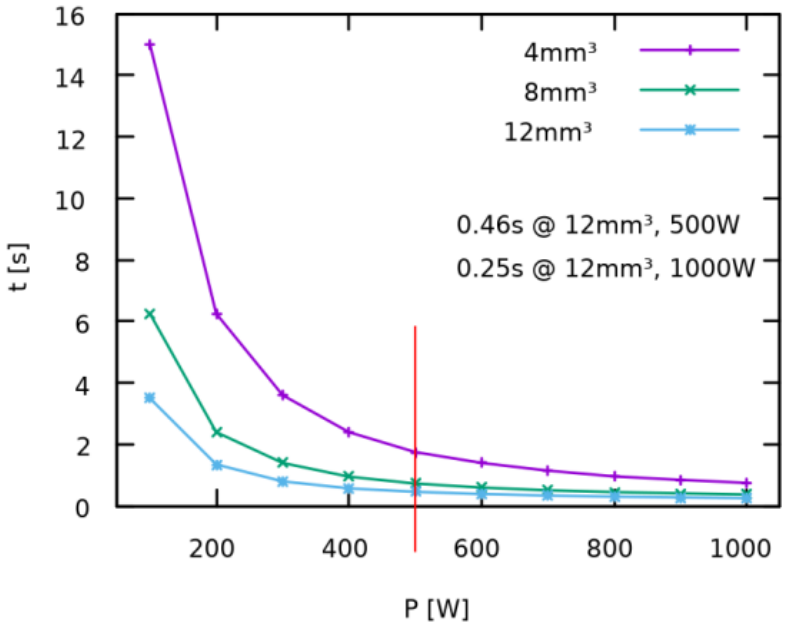

Figure 4: *Time vs. Power.*

As a cross check for the linearity of the calculations figure 6 displays T_{abs} versus the absorbing fraction for the three equally spaced beam powers $100\,\mathrm{W}$, $500\,\mathrm{W}$ and $900\,\mathrm{W}$.

Table 3 summarizes the limits obtained from the calculations to be achieved by the acquisition and safety functions.

$T_{sens,max}$	$60\,°\mathrm{C}$
reaction time	0.5s
$\lvert\Delta T_{max}\rvert$	$10\,°\mathrm{C/min}$

Table 3: *Limits.*

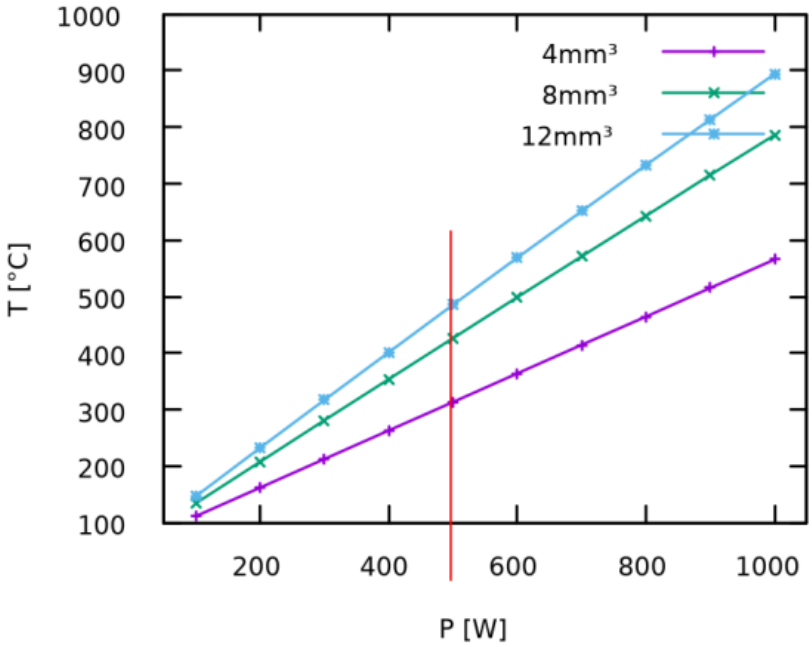

Figure 5: *Temperature T_{abs} vs. Power.*

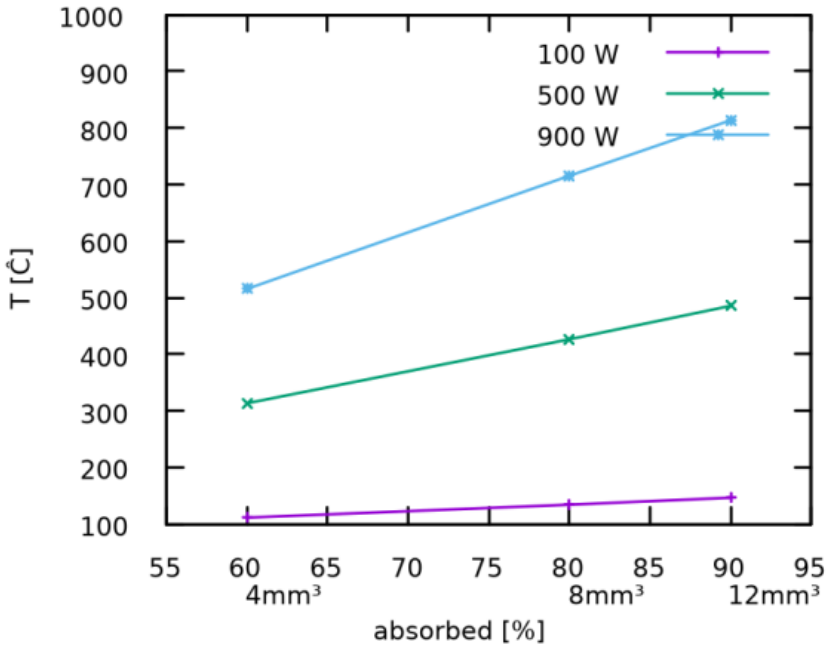

Figure 6: *Temperature T_{abs} vs. Absorbed Fraction.*

3 Temperature Data Acquisition

For measuring the temperature T_{sens} a probe with two integrated PT100 sensors is screwed into the absorber bulk at the position indicated in figure 3. The two PT100 are connected to a fail-safe current readout card (F-AI 4xI 0(4) ... 20 mA 2-/4-wire HF) attached to a fail-safe PLC (F-SPS). The PLC continuously checks for the temperatures to be within the limits.

Figure 7 shows an extract of the PLC logic implementing the safety function (described in section 1). The logic is augmented by the signal "ABS ok" indicating the temperature is within the limits. When the absorber aught to be closed "ABS ok" is required in addition to the "ABS closed" signal to form the "ABS closed validly" signal entering the beam permission logic for the area in front off the beam shutter.

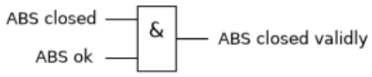

Figure 7: *ABS closed validly.*

3.1 Failure considerations

Figure 8 sketches possible failures on a four-wire measurement. Table 4 attributes to each failure if it is dangerous and if it can be detected.

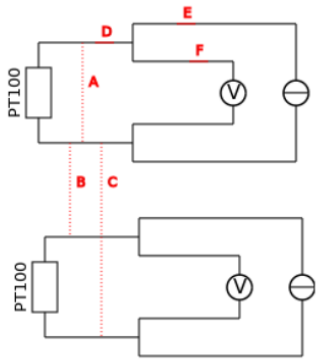

Figure 8: *PT100 readout and possible failures.*

A note on the possible failure **A** (bypass/resistance across PT100): In order to prevent this failure to be undetected a lower limit for the resistive value will be applied. This converts to a lower temperature limit. The lower limit mitigates the effect of failure **A**, the safety function will still work but only at a higher temperature. The most critical value of the resistivity due to failure **A** has been found to be around $1\,\mathrm{k\Omega}$. In addition to mitigate this failure by the lower limit failure **A** will be detected by comparing both channels.

3.2 Reaction times

The requirement $T_{abs,max}$ ($500\,^{\circ}\mathrm{C}$) can not be guaranteed because of the limited reaction time of the complete safety function (about some tens of a second).

In order to have enough safety margin the temperature limit was chosen to be less than half the absorber melting point temperature. Melting a hole all the way through the absorber will add additional time as safety margin to mitigate the limited reaction time.

A second issue is that the PT100 used is specified for a maximum temperature of $180\,^{\circ}\mathrm{C}$ only.

These issues underline the importance of the earlier stated requirement to thoroughly inspect the absorber in any case the measured temperatures lie above the required limits (except during the tests with hot air).

Failure	danger.	undang.	detect.	undetect.
A 0 Ω	x		x	
A 1 kΩ	x		x	
B 0 Ω	x		x	
B 1 kΩ	x		x	
C 0 Ω	x		x	
C 1 kΩ	x		x	
D Discon.		x	x	
D 100 Ω		x	x	
E Discon.		x	x	
E 100 Ω		x		x
F Discon.		x	x	
F 100 Ω		x		x

Table 4: *List of possible failures: dangerous/undangerous failure, detectable/undetectable failure.*

3.3 Discussion on failure rate estimation

The PT100 sensor manufacturer does not provide failure rates. Therefore we estimate the failure rate roughly by considering the PT100 as having failure modes equivalent to a coil and a resistor. Table 5 lists the assumed resistor and coil failure rates as well as the estimated PT100 failure rate.

Component	FIT
Resistors	1-3
PT100 (coil)	5
Estimated failure rate for a PT100	10

Table 5: *Estimation of PT100 failure rate.*

The failure rate of the PT100 two channel partial system considered conservatively without failure diagnostics can be roughly estimated according to type B basic architecture of EN 62061 [3]. Conservatively using $10\,000\,\mathrm{h}$ of operation between proof tests and the maximum common cause failure factor of $\beta = 0.1$ the PFH results to ≈ 0.5 FIT.

We assume a failure rate of 10 FIT for the series resistors additionally used in the circuit.

According to the manufacturer the current readout card failure rate is PFH = 1 FIT. It has to be noted that the nominal current range of the card is 0-20mA while the current range given by the PT100 and the series resistor used is just about 0.3mA. This range is below the specified card tolerances. Therefore the given failure rate seams not to be applicable directly. Nevertheless from continuously monitoring plausible temperatures measured at the three absorbers for a couple of month we are confident that the readout is sensitive. It is an open question how to evaluate the failure rate. For further discussions we use a ten fold higher than specified failure rate of PFH=10 FIT.

The failure rates of the PLC, the ProfiNet communication, input and output cards each are specified to be less than 1 FIT. Conservatively for the combination of these components we assume a failure rate of 10 FIT.

Table 6 presents the very preliminary estimation of the failure rate for the temperature acquisition.

The failure rate estimated in table 6 would fulfill the requirements for hardware failure rates up to SIL 3. It is

Partial system	FIT
two channel PT100	0.5
series resistors	10
current readout card	10
PLC and other cards	10
Estimated temperature acquisition failure rate	30.5

Table 6: *Temperature acquisition failure rate estimation, assuming 10000h proof test interval.*

clear that other important requirements to assign a SIL value like the safe failure fraction and most of all the systematic failure integrity have not been considered here.

Furthermore the safety function makes use of the existing PETRA3 personnel interlock system which has to be taken into account when considering the complete safety function.

3.4 Testing

Annual tests of the PETRA3 interlock as well as tests of the beamline interlocks are performed.

These tests have to be augmented in order to verify the proper functioning of the temperature detection. The additional tests are applied in the following three states of the life cycle:

Initial installation, proof of principle:

- Test the whole safety function with real beam. Therefore the x-ray beam will be positioned onto the absorber. This means the PS will have to be opened while the absorber is not opened. The function prohibiting this in normal operation will have to be disabled during the test.

Annual Testing:

- Test ABS reaction by heating with hot air.

Testing during operation, by F-SPS:

- Continues plausibility checks.
- Continues test for short circuits.

3.5 Temperature Plot

Figure 9 shows the temperatures of the three absorbers at P61 measured during a test with hot air. During the test both, the limit on the maximum allowed change in temperature over time ΔT_{max} and the maximum absolute temperature limit $T_{sens,max}$ have been verified.

4 Conclusion

The systems have been installed and the logic has been approved. It was decided to use the system without the four wire measurement since it was found to be running stable for a long time with a two wire measurement. It is still possible to implement the four wire measurement once it turns out to be needed.

The behaviour when temperatures change have been tested by heating the absorber with hot air. The crucial test with the wiggler beam pointing on the absorber for testing is planed and will be conducted in the near future.

The assessment has to be continued including the mechanical construction safety approval.

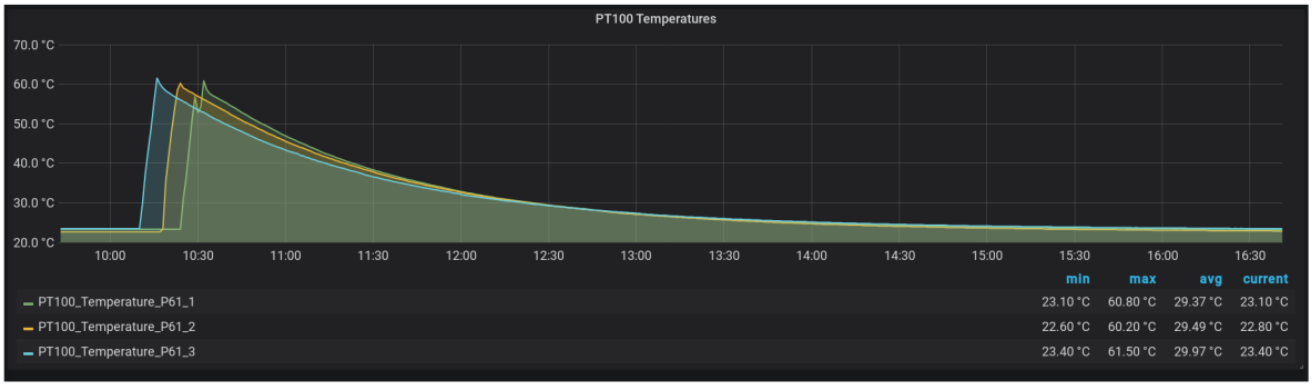

Figure 9: *Measurements of temperatures vs. time at the three absorbers of P61 during tests with hot air.*

References

[1] Christian Amann, Ulrich Hahn, Albrecht Leuschner, Hans-Bernd Peters, Horst Schulte-Schrepping
Sacrificial Absorbers for the PETRA III Beamline Safety
unpublished

[2] Horst Schulte-Schrepping and Paul Wiesener,
Private note on heat conduction calculations and conversion of x-ray to heat in copper.

[3] *Sicherheit von Maschinen*
Funktionale Sicherheit sicherheitsbezogener elektrischer, elektronischer und programmierbarer elektronischer Steuerungssysteme
DIN EN 62061:2013-09

Radiation safety exercise in Beamline and some learning points

Sanjeev Faruk[1], Richard Doull

Diamond Light Source Ltd
Harwell Science and Innovation Capus
Didcot, Oxfordshire, OX11 0DE,
October-2019

[1] For correspondence: E-mail: sanjeev.faruk@diamond.ac.uk

Abstract

Ionising Radiations Regulations 2017 (IRR17) and other health and safety legislation encourage to a rehearsal of contingency plan in a regular interval. Diamond starts doing this exercise to comply with the law and as part of the safety culture. This is to make aware of the beamline staff of the danger of accidental radiation exposure. So far, 19 beamlines participated until to date. A scenario of someone accidentally locked in the hutch with the beam in the hutch. Member of beamline staff asked to respond to the incident and the observation was noted. At the end of the exercise, we highlighted the actions needed to be prioritised to save lives and reduce the exposure level. It was observed that they managed to make the situation safe from 3 to 130 seconds with an average response time of 54 sec. Consequently, the casualty received exposure level from 9 to 390 mSv depending on the hutch with average dose of 161 mSv, which could cause detectable chromosome changes in blood cells. A series of recommendation and problem raised from all these exercises, which will need to be debated before incorporating in future beamline and PSS design.

1 Introduction

This rehearsal is to comply with IRR17 and make sure that all members of Beamline staff are familiar with the contingency plan in the Beamline and Experimental Hall local rules and in the event, of a radiation overexposure emergency, they can act more effectively. *This is not a test.*

All Beamline staff were briefed before the exercise as to what was going to happen without giving any information about the scenario. They were split into several groups and asked to respond to the incident so that all of them could have a chance to experience this exercise. At the end of the exercise, they were de-brief about the expected exercise response.

2 Scenario

We change scenario depending on the beamline setup. Here is one example - A contractor was missed during the search and locked in the hutch. Beamline staff spotted the contractor in the hutch through the view panel while they were taking beam in the hutch. The rehearsal started as soon as they spotted the contractor. Or they could receive a phone call from inside the hutch...

> 'Hello! Hello! I'm a contractor that is new on-site and I followed a rat/mouse into one of the yellow rooms and someone closed the door behind me, which seems to be locked. The room lights went blue, I'm very confused and scared. Do you know what is happening? Can you help me?'...

The timer starts counting to record the response of the beamline staff.

3 Observation

The actions taken during the emergency exercise by the groups are listed in Table 1.

Table 1: *Contingency exercise observation list : An example from one of the recent exercise responses.*

Steps	Expectations	Observations
Press 'Beam Off' button /Shutter off from control panel	Yes	Yes
Remove Beamline enable key	Yes	Yes/No
Enter Hutch and Monitor Radiation in the Hutch	Yes	Yes
Check casualty (do not leave casualty if possible)	Yes	Yes
Call Control room (8899/8999) (ask for a First Aider and ambulance, if required)	Yes	Yes
Collect information from the casualty/ anyone else	Yes	Yes
Collect any Dosimeter if worn	Yes	Yes/No

We discuss the actions the participants took during the exercise and highlight where they could improve to stop/ minimise radiation exposure. Answer any questions they have or concern raised during the exercise.

4 Exercise Report

We provide a report at the end of each exercise to explain the importance of the exercise and to assist them in realising the consequences of radiation exposure if someone gets locked inside the hutch and exposed for a certain amount of time before someone could stop the beam. We also explain the quickest response one could do by pressing EBOB (Emergency Beam of Button) instead of trying to close the shutter from the control or any other means. Following section, we usually include in the report in the context of historic radiation exposure.

Response analysis: Consequence of radiation exposure in the hutch

It is necessary to explain the consequences of accidentally trapping someone in the hutch and are exposing them to radiation. The calculated dose could be typically $10\,000\,\mathrm{mSv/h}$ ($3\,\mathrm{mSv/sec}$) at a meter distance from the scatter point inside the hutch.

Example from a recent exercise -

> The maximum time of quickest response to press the emergency beam of button EBOB on this exercise observed was $\mathbf{130\,sec}$ contributing exposure of $\mathbf{390\,mSv}$ this could cause detectable chromosome changes in the human cell.

An experiment in B16 beamline indicated that the maximum radiation exposure at the point of sample position could reach up to $9\,\mathrm{mSv/s}$ for $15\,\mathrm{keV}$ DCM and $12\,\mathrm{mSv/s}$ for White Beam mode.

Following Table 2 explains [2] the consequence of some common reason or symptoms one could expect from radiation exposure damage in relation to the hutch exposure effect (daily life, early or late).

Table 2: *Typical effect of radiation exposure*

Dose (mSv)	Typical Effect
10,000	Observable damage to the exposed organ; death probably within weeks, if the whole body exposed
390 mSv	*From this exercise response*
200	Detectable chromosome changes in blood cells
50	Chromosome aberration
20	Annual dose received by individuals from radon in certain areas of the UK
2.75	**Typical annual dose from the natural background**
2	Typical x-ray examination of the lumbar spine

5 Conclusions

In the event of a radiation exposure incident in a hutch, the response should be very prompt with a proactive attitude. It is very unlikely that every member of Beamline staff will respond according to the contingency plan in Beamline local rules. To overcome this a flow chart of the important steps (Fig 1) is provided in each beamline to follow in case of a radiation emergency. This exercise was to mimic a real incident situation to give an understanding of what actions to take safely and effectively to sustain any ionising radiation incident casualty before the emergency support team arrives. With this exercise, we hope that, in future, the participant will take these actions (Table 1) effectively without any hesitation in case of radiation overexposure incident.

We also advise the beamline staff to make sure the flowchart is available in the control room or next to each hutch entrance in a visible location, which highlights the steps to take in case of suspected radiation over-exposure incident.

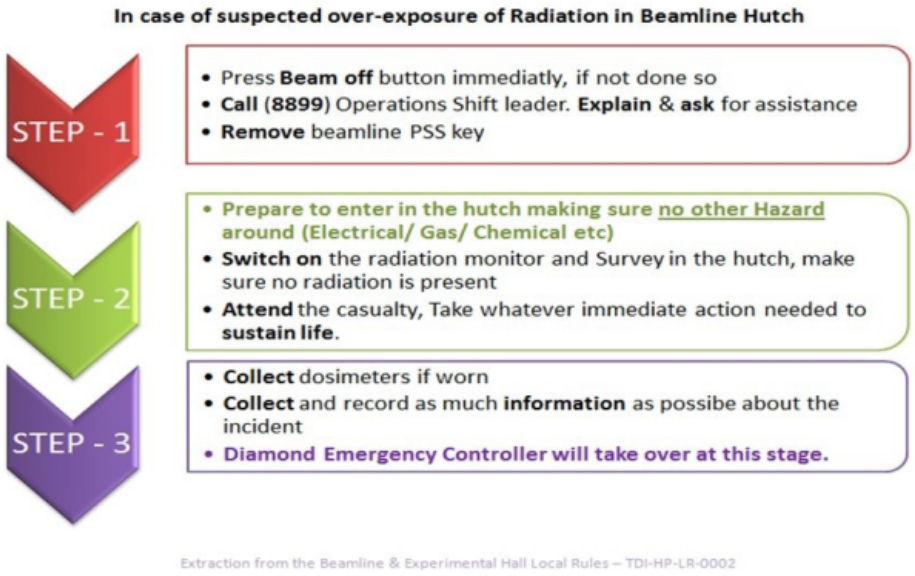

Figure 1: *Contingency steps flow chart.*

References

[1] DLS Safety Organiser, RA (TECH-PHYS-DLS-RA-2011/00005).

[2] HSE, The tolerability of risk from nuclear power stations, page 18, 1992.

Initial experience for 3.5 GeV Diamond II shielding calculations

Sanjeev Faruk, Richard Doull

Diamond Light Source Ltd. UK
October-2019

Abstract

Diamond is planning to replace its current storage ring with a new Double-Triple Bend Achromat (DTBA) known as Diamond II. With a plan to build this within the existing shielding this study calculates if the current shielding is sufficient and if any increases are required.

The current Diamond storage ring and beamlines are shielded to run at an energy of $3.0\,\mathrm{GeV}$ and $500\,\mathrm{mA}$ current. The plan for Diamond II is to increase the energy to $3.5\,\mathrm{GeV}$ and reduce the maximum current to $300\,\mathrm{mA}$. Currently, Diamond has two ID straights ($15.6\,\mathrm{m}$ and $18.6\,\mathrm{m}$), Diamond II will have three different ID straight sections of $3.9\,\mathrm{m}$, $6.5\,\mathrm{m}$ and $9.5\,\mathrm{m}$. Health Physics did the initial shielding calculation for the storage ring using Shield 11 (electron loss), semi-empirical formula and FLUKA for Gas bremsstrahlung (GB) in the stage ring and optics hutches and STAC 8 for synchrotron radiation on the beamlines. The initial calculation indicates the shutter thickness could decrease in Booster to storage (BTS) and the front end shutters. However, there will be an increase in shutter thickness in place of all current bending magnet beamlines. Most of the optics hutch lead wall thickness will not need any modification except those with superconducting wigglers and all current bending magnet beamline hutches (which will be ID beamlines on Diamond II). For the assessment, we used a dose constraint of $1\,\mathrm{mSv/year}$.

1 Introduction

The current Diamond storage ring and beamlines are shielded to run at an energy of $3.0\,\mathrm{GeV}$ and a stored current of $500\,\mathrm{mA}$. This paper assesses if the current shielding will be adequate for Diamond-II which will run at an energy of $3.5\,\mathrm{GeV}$ and $300\,\mathrm{mA}$ stored current. For the assessment we will use the current dose constraint of $1\,\mathrm{mSv/year}$, the justification for this is set out in TDI-HP-GEN-PRO-0003 [1].

2 Sources of Ionising Radiation in Diamond-II Accelerators

There are several processes that produce ionising radiation within the booster, storage ring, and beamlines.

2.1 Electron Losses

High energy electrons can impact parts of the machine they strike, this sets off an electromagnetic cascade of Gamma and Neutron radiation, which dominates the shielding requirement. Electrons are lost in a number of ways:

- Beam dump, these can be intentional i.e. beam dump prior to machine development, or unintentional i.e. RF trip.
- Losses of the stored beam due to finite lifetime.
- During injection, and extraction from the booster, because of less than $100\,\%$ injection/extraction efficiency.

2.2 Gas Bremsstrahlung

When high energy electrons interact with residual gas molecules within the vacuum vessel they emit high energy x-rays up to the energy of the incident electron. The x-rays are highly focused in the direction of travel of the electrons, this, therefore, dominates in the calculation of the thickness of the front end shutters and to a lesser extent, the upstream ratchet wall.

2.3 Synchrotron Radiation

This is produced when electrons pass through a bending magnet or insertion device, the direction of the x-rays is tangential to the electron trajectory.

In beamline optical hutches shielding is defined by the Gas Bremsstrahlung and synchrotron radiation, in experimental hutches shielding is defined by synchrotron radiation only. A full assessment is ongoing, but a summary of the work done so far is given below.

2.4 Activation

High energy electrons can induce radioactivity in parts of the machine that they strike. The current procedures for protecting against exposure from activation products should be sufficient for Diamond-II. This is not a hazard to anyone outside of the shielding and is not considered further in this document

3 Assessment Methods

3.1 Electron Losses

We have calculated the dose outside the storage ring and booster shielding using the equations contained in the modelling code SHIELD 11 [2]. SHIELD11 is a computer code for shielding analysis around high energy electron accelerators developed by Stanford Linear Accelerator Centre (SLAC). It takes inputs of beam parameters and shielding thicknesses and dimensions, it then outputs dose rates for Neutron (three different energy ranges), direct gamma, and indirect gamma outside the shielding at specified points. For convenience, we have taken the equations used in the code and developed an Excel version for the Diamond-II shielding calculations.

3.2 Gas Bremsstrahlung

The shielding requirement is calculated using several methods:

- Known expressions, used in other accelerators and synchrotrons to assess photon fluxes and thus shielding requirements. Holbourn [3]
- Established computer-modelling codes, used in other accelerators and synchrotrons to calculate the dose rate in a semi-empirical manner. Tromba and Rindi [4] , Ipe [5].
- Monte Carlo modelling using FLUKA (use of this method is in the early stages and is not used for the calculations in this document).

Several expressions in published papers were compared and the average shielding thickness is taken. Some assumptions have been made as the quantities required in the expressions are not currently known. These include vacuum pressure and residual gas composition.

3.3 Synchrotron Radiation

The shielding requirement for beamlines is calculated using a Fortran code developed at SPRING 8 called STAC8. By inputting machine, ID, mirror, filter, and shielding parameters the dose rate at any point on the outside of the shielding can be calculated. A trial and improvement method is used to calculate how much shielding is needed to reduce the instantaneous dose rate to $<0.5\,\mu\mathrm{Sv/h}$ ($1\,\mathrm{mSv}$ per $2000\,\mathrm{h}$ working year).

4 Results

4.1 Storage ring

Table 1 below shows the current shielding thickness of the storage ring concrete walls and roof. Annual doses outside of the shielding due to electron loss have been calculated using the SHIELD11 code. The dose rates are calculated at a number of angles from the loss point, the dose rate stated below is highest out of all the angles calculated. We have assumed that the machine will run for $5160\,\mathrm{hours}$ per year and the total electron loss over the run time is 1.54×10^{16} (corresponding to $8.27 \times 10^{8}\,\mathrm{electrons/s}$). We have calculated the average annual dose for both the machine run time and a typical $2000\,\mathrm{hours}$ working year. The target dose rate is $<1\,\mathrm{mSv/year}$.

Table 1: *Storage ring wall shielding and dose distribution.*

Location	**Current material thickness (mm)**		**Occupation (2000 hrs)**	**Machine run time (5160 hrs)**
Storage ring shield wall	Ordinary Concrete	Barytes Concrete	Total (mSv/y)	Total (mSv/y)
Inner wall	1250		0.0043	0.01
Side wall		950	0.0325	0.08
End wall		1550	0.0000	0.00
Roof	1430		0.0054	0.014

5 Booster

5.1 Booster Wall

The booster is also undergoing a change of design, not only will the maximum electron energy increase to $3.5\,\mathrm{GeV}$, the booster circumference is increasing. As it will be housed in the existing shielding, the vacuum vessel will be closer to the outer shield wall.

We estimate only a factor 2.8 times more loss in the Diamond-II booster than the current Diamond booster; calculated doses are in Table 2 below.

Table 2: *Booster wall shielding and dose distribution.*

Location		**Current material thickness / mm oridinary concreate**	**Total annual dose (mSv/y)**
Booster	Outer wall	1900	0.01
	Roof	2050	0.012

The figures above were calculated using a larger loss rate than the current estimate, so the existing shielding

will be adequate, which is consistent with the fact that it is rare that any dose outside the booster is recorded.

5.2 Booster to Storage (BTS) ring shutter

So that the storage ring can be entered when the booster is running, a shutter is in place in the booster enclosure on the BTS line. Electrons are deflected away from this shutter into the Faraday cup if they are not injected into the storage ring. This shutter will need to stop gas bremsstrahlung that will be generated in the BTS line. Table 3 shows that the current thickness of the shutter exceeds the requirements for Diamond-II.

Table 3: *BTS shutter thickness. Material is Mallory 1000, a tungsten alloy.*

Straight Section leading to BTS shutter	Current thickness (mm)	Diamond-II required thickness (mm)
$8.6\,\mathrm{m}$	316	271

The above calculations will be checked against the final booster design in the TDR phase.

5.3 Port/Optics Shutters

Port/optics shutters or front end shutters are located at the downstream end of the front end, each shutter can operate independently. The thickness required is dominated by gas bremsstrahlung.

Table 4 shows the current thickness and the minimum thickness required for Diamond-II for the various ID straight lengths.

Table 4: *Port/Optics shutter thicknesses. Material is Mallory 1000, a tungsten alloy.*

Diamond, bending magnet of ID straight length	Diamond current thickness (mm)	Diamond-II bending magnet to bending magnet length	Diamond-II required shutter thickness (mm)
Bending magnet	180	$3.95\,\mathrm{m}$	271
$18.581\,\mathrm{m}$	316	$6.59\,\mathrm{m}$	279
$15.581\,\mathrm{m}$		$9.59\,\mathrm{m}$	286

Front end shutters on all ID beamlines are therefore adequate for Diamond-II. In the case of bending magnet beamlines, however, the majority, or possibly all, will move to insertion devices located in the new mid straights and therefore will require an upgrade of the shutters.

6 Beamline shielding

Calculations of beamline shielding is currently incomplete as not all the information required for the calculations is currently available.

6.1 Optics Hutches

The lead thicknesses required to reduce the dose rate to below $1\,\mathrm{mSv/y}$ in Diamond-II are shown in Table 5. All existing Optics hutches on insertion device beamlines have been built to '9.5m straight' specifications, and therefore require no modification, with the following exceptions. I19 and I24 have reduced thickness optics hutches as canting have been used, if canting is not employed on Diamond-II this may need to be increased. The

superconducting wiggler beamline I12 needs some additional shielding to that stated above and it is anticipated that I15, also a superconducting wiggler beamline, will also need additional shielding; calculations have not yet been finalised.

Table 5: *Optics hutch shielding required for the three lengths of ID straight in Diamond-II.*

Location	**Lead thickness required for Diamond-II (mm)**		
	9.59 m straight	**6.59 m straight**	**3.95 m straight**
End wall	50	43	31
Additional lead $1\,\mathrm{m}^2$ around beampipe	50 (100 total)	15 (58 total)	13 (44 total)
Lateral wall	30	18	10
Roof (assuming $2.6\,\mathrm{m}$ above beampipe)	10	10	8
GB collimator/stop thickness (Mallory 1000)	286	279	271

The current shielding on bending magnet beamlines is $8\,\mathrm{mm}$ lead for all walls and roof, with an additional $25\,\mathrm{mm}$ around the beam pipe. All bending magnet beamlines that move to an insertion device on the new mid section straights will therefore require additional shielding on the end wall, lateral wall and beam pipe. The required thickness of the collimators and stops are listed above. All existing GB collimators/stops in insertion device beamlines and B16 are thicker than '$9.5\,\mathrm{m}$ straight' specifications, and therefore require no modification. B24 has $370\,\mathrm{mm}$ thick bremsstrahlung stops in the front end. The current thickness on all other bending magnet beamlines is $180\,\mathrm{mm}$ and so all beamlines that move to an insertion device on the new mid straights will require thicker GB collimator/stops.

All other dimensions of GB collimators and their location will be determined by ray trace.

6.2 Experimental Hutches

Experimental hutch shielding is calculated on a case-by-case basis and is dependent on not only the machine parameters but also the insertion device, mirrors, and hutch dimensions. Calculations have not been concluded, as specifications have not been finalised.

Based on what has been done so far the current shielding of most experimental hutches is sufficient for machine operation at $3.5\,\mathrm{GeV}$, $300\,\mathrm{mA}$. The shielding was originally calculated for $3\,\mathrm{GeV}$ and $500\,\mathrm{mA}$. Some beamlines with more powerful insertion devices will need thicker experiment shutters of the order of a few mm.

As with its optics hutch, I12 will need thicker shielding in some areas. It is anticipated that I15 will also need additional shielding. Calculations have not yet been finalised.

7 Conclusions

The results above show that the current concrete shielding for the storage ring and booster is adequate for operation at $3.5\,\mathrm{GeV}$ and that most shutter thicknesses are also adequate to shield the highly penetrating Gas Bremsstrahlung x-rays.

Most beamlines will not need any additional shielding.

Many factors can affect the intensity of the scattered radiation. While simulations have been shown to predict dose rates to a fair degree of accuracy, certain factors cannot be predicted. Of particular concern is the level of vacuum in long narrow insertion device (ID) straights of the storage ring. For these calculations, a vacuum

of $1 \times 10^{-8}\,\mathrm{mbar}$ has been used. The vacuum will be worse than this during the initial conditioning of the machine until several ampere-hours have elapsed. In the early stages, whilst the storage ring is undergoing conditioning, it will be necessary to run the machine with the shutters closed and to possibly restrict access to synchrotron building until sufficient experience has been gained of the machine's performance. The machine is likely to require several tens of ampere- hours of conditioning before the vacuum has reached an adequate level to permit the port shutters to be opened without producing excessive radiation. Health Physics will need to perform extensive measurements once the machine starts operation to ensure that radiation levels are kept As Low As Reasonably Practicable (ALARP).

8 Further work

8.1 Monte Carlo Models

To confirm the above calculations we are developing a Monte Carlo model of Diamond-II using MCNP (Monte Carlo N-Particle Transport Code).

We have also started modelling the various interactions using FLUKA (Monte Carlo code developed by CERN).

8.2 Beamline Shielding

Continue with the calculation of the adequacy of the current beamline shielding as new ID and mirror specifications are submitted.

8.3 Ray Tracing

Ray tracing will need to be performed on all front ends and beamlines to ensure sufficient gas bremsstrahlung and synchrotron radiation collimation.

8.4 Environmental Impact Assessment

An assessment will need to be made of the potential for activation of the air, cooling water and groundwater. This was done for Diamond and will be repeated for Diamond-II using the new machine parameters.

References

[1] TDI-HP-GEN-PRO0003 Strategy for the Implementation of Radiation Safety Legislation at Diamond

[2] The SHIELD11 Computer Code (https:// www.slac.stanford.edu/cgi-wrap/getdoc/slac-r-737.pdf)

[3] Holbourn, M. P. *Gas Bremsstrahlung Measurements at the ESRF*, 1994.

[4] Tromba, G and Rindi, A. *Gas Bremsstrahlung From Electron Storage Rings: A Monte Carlo Evaluation and Some Useful Formulae.* Nuclear Instruments and Methods in Physics Research **A292**, (1990).

[5] Ipe, N and Fasso, A. Impact of Gas Bremsstrahlung on Synchrotron Radiation Shielding at the Advanced Photon Source. SLAC-PUB-6410, (1994).

Radiation Protection Interlock Systems at the KIT Synchrotron

Michael Hagelstein, Erik Bründermann, Albert Gies, Richard Kubat, Wolfgang Mexner,
Anke-Susanne Müller, Robert Ruprecht, Marcel Schuh, Pawel Wesolowski, Olaf Zwernemann

Karlsruhe Institute of Technology KIT, Karlsruhe, Germany
October-2019

Abstract

The radiation safety and protection system of the KIT Synchrotron in Karlsruhe, Germany, is composed of three interlinked systems: the Personnel Interlock System of the machine and the Beamline Personnel Safety System of the beamlines, together with an independent system to control the status of all front-end shutters. The Personnel Interlock System consists of hard-wired linked hardware controlled by a programmable logic controller and is in operation since the start-up of the facility in the year 1998. Its design follows safety standards and the principle of good engineering practice.
The Beamline Personnel Safety System controls the exclusive access of either ionizing radiation or persons to the beamline radiation hutches. The reliability of components and the overall system obeys the terms of safety categories and the risk analysis by the standard EN ISO 13849. It links the Safety Integrity Level concept to Performance Levels defining an approach in terms of probabilistic failure rates for components and systems. The personnel safety system for the currently commissioned new accelerator FLUTE of KIT is based on the same concepts.
We plan to refurbish the Personnel Interlock System for the accelerator of the KIT synchrotron and adapt the new system to current standards defined by the machqinery directive and following good engineering practice.

1 Introduction

The Karlsruhe Institute of Technology (KIT) in Karlsruhe, Germany, operates the KIT synchrotron with its storage ring called Karlsruhe Research Accelerator KARA. The KIT synchrotron is in its 20th year of operation. The electron accelerator complex consists of a $53\,\mathrm{MeV}$ microtron, a $0.5\,\mathrm{GeV}$ booster synchrotron, and the $2.5\,\mathrm{GeV}$ storage ring KARA with a circumference of $110.4\,\mathrm{m}$. The Institute for Beam Physics and Technology (IBPT) takes the responsibility to operate the accelerators safely. IBPT also delivers synchrotron radiation to 20 beamlines, conducts accelerator research, and develops innovative accelerator technology (see i.e. [1, 2]). As part of the KIT Accelerator Technology Platform other technologies, like superconducting insertion devices and detectors for accelerators are developed. You may watch the video [3] for current activities and strategies.

IBPT also constructs and currently commissions the linear accelerator test facility called FLUTE (German acronym for Ferninfrarot Linac Und Test-Experiment), a $50\,\mathrm{MeV}$ linear accelerator and a source for coherent, high power THz radiation [4].

Several institutes of Campus North of KIT operate the beamlines of the KIT synchrotron. Two examples of current materials research on catalysts is given in Zimina et al [5] and on XAFS investigation on nuclear waste forms in Rothe et al [6].

The operating personnel has acquired comprehensive experience with the different types of safety systems.

2 The Personnel Interlock System of the KIT Synchrotron

The keys, doors, search switches, emergency stop switches, automatic audio system, and warning lamps of the Personnel Interlock System (PIS) are hard-wired linked and controlled by a central programmable logic controller (PLC). The system components are shown in figure 1. The operators search the area following a defined scheme (4 search switches for the inner area with the booster synchrotron, 10 switches for the outer area of the storage ring KARA) and visible as well as audible warning signs are activated before the injection may commence. A process field bus (Profibus) links the individual safety components to the PLC.

3 The Beamline Personnel Safety System of the KIT Synchrotron

The Beamline Personnel Safety System (BPSS) is a Safety Instrumented System (SIS) to control the exclusive access of ionizing radiation or persons to the beamline radiation hutches. The reliability for components and the overall system was defined in terms of safety categories and based on the risk analysis by the standard ISO 13849. The standard links the Safety Integrity Level (SIL) concept to Performance Levels (PL) defining an approach in terms of probabilistic failure rates for components and systems. The BPSS assures the following requirements [7]:

- At least one upstream radiation shutter, which is closed and interlocked in front of an accessible hutch.
- Downstream access doors or monitored radiation shutters, which are kept closed and interlocked if a safe shutter state is not reached in a fixed time span.
- An accelerator beam dump, which is initialized in case of interlock break of shutter or hutch door, component or subsystem failure.
- The use of a redundant frontend shutter safety controller supervising local beamlines in repair mode, if the local beamline safety controller is switched off.
- All the components, subsystems and the whole BPSS are monitored with Diagnostic Coverage (DC) at the highest possible level of $>99\,\%$.

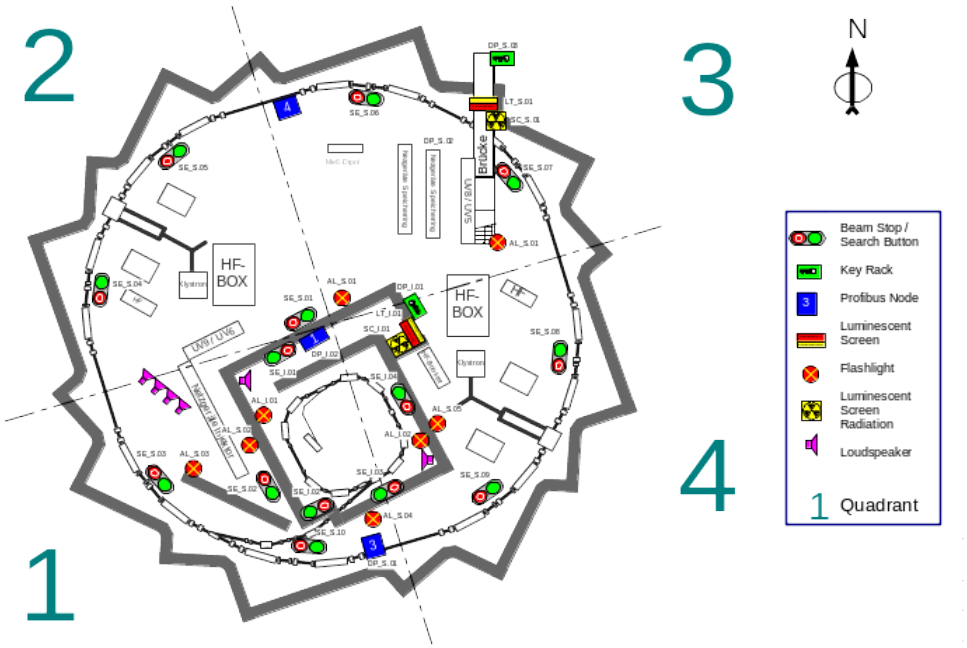

Figure 1: *Components of the Personnel Interlock System PIS of the storage ring KARA of the KIT Synchrotron. The components of the safety system are singled out.*

The overall layout with the main nodes of the system is shown in figure 2. A central safety relay and controller unit (brand name PNOZ of the company Pilz [8]) is connected via a redundant safety bus to four local safety controllers (Pilz PSS SB 3006-3) inside the area of the storage ring mend to control the status of the beamline front-end radiation safety shutters independently of individual beamline controllers. This configuration allows to set the local beamline safety controllers into a safe repair mode individually without compromising the operation of the whole facility. Each beamline is controlled with a local safety controller (Pilz PSS3100, PSS4100). Each of the beamline controllers is connected to the central safety relay and controller unit. The controllers contain a CPU and a set of input/output modules (see figure 3 [9]). The status of beamline components is supervised as well as the hutch doors and search status. Always two sensors and actors (subsystem 1 and 3) in parallel assure the safe function of the hardware redundantly. If a failure of any of the single electric circuits is detected during the search, the hutch cannot be closed nor switched to operation mode. In case the preceding shutter of a hutch is open and synchrotron radiation is already introduced into the hutch, a failure of the central controller or the system components leads to a beam dump. The controller hardware, the software modules and the safe fieldbus (Safety-BusP, [10]) are certified according to the safety integrity level SIL 4.

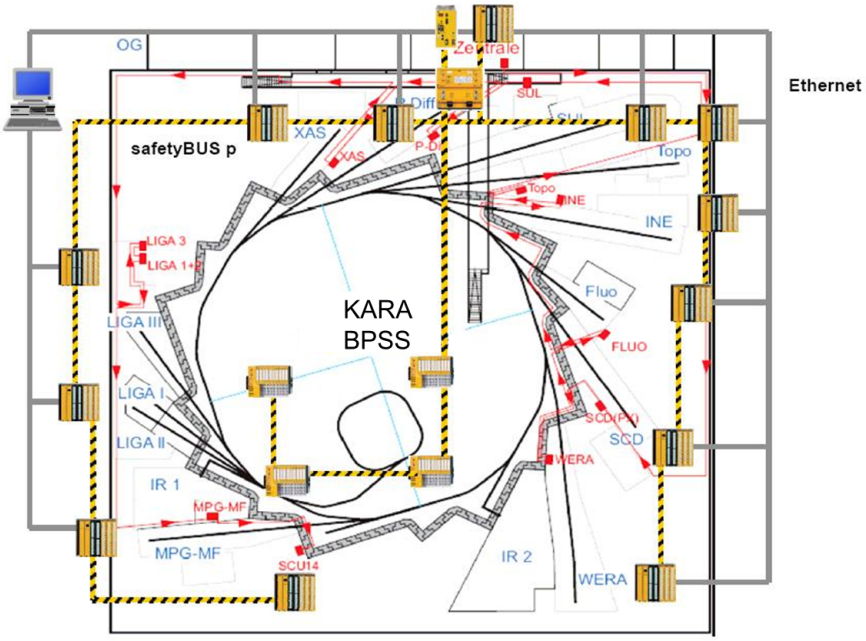

Figure 2: *Schematic drawing of the Beamline Personnel Safety System BPSS with an inner bus composed of four cabinets to control the state of the front-end shutters and an outer ring with one cabinet each to control the beamline operation.*

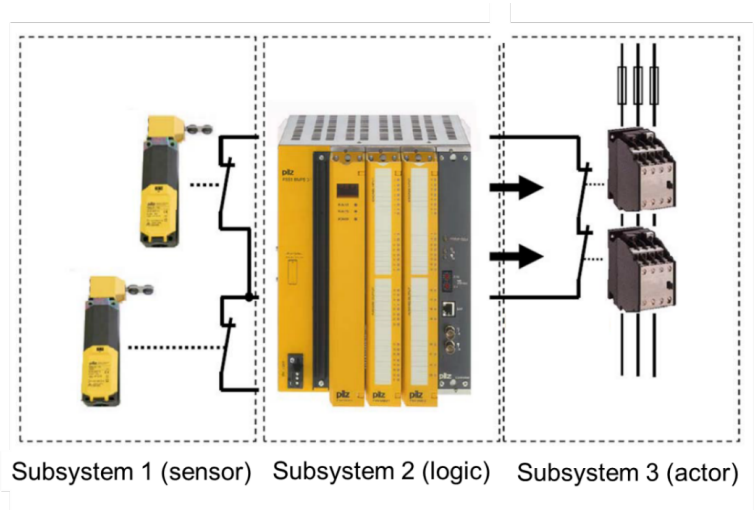

Figure 3: *Schematic description of the safety logic controller consisting of a CPU and the input/output modules (subsystem 2) to control a beamline. A field bus links the central logic to pairs of sensors and actors.*

The safety system control law is to assure that radiation and personnel access at the same location at the same time are excluded fail-safe [7]:

- Time invariant probability of unknown dangerous risk
- Performance Level PL: 1×10^{-8} undetected dangerous events per hour over the planned lifetime of the safety system

The safety integrity of the whole system is constructed and verified in the framework of the control standard EN ISO 13849 [11]. The software tool SISTEMA is available to assess the safety integrity [12, 13]. The Institute for Occupational Safety and Health of the German social accident insurance provides the software.

A manufacturer software tool including the applied safety bus [14] is used to assess the safety integrity of the systems at KIT.

The conception and assessment contains the following steps:

- Determine required PL_r (Performance level)
- Draft of the safety circuitry
- Determination of the safety category using MTTFd (Mean Time To Failure to dangerous), DCavg (average diagnostic coverage) , CCF (Common Cause Failure)
- Determination of the total MTTFd using the Parts Count scheme

The state of the beamline, its components and the BPSS is displayed using the platform-independent supervisory control and data acquisition (SCADA) system WinCC-OA [15].

4 Summary

The Karlsruhe Institute of Technology applies a state of the art safety systems composed of programmable logic controllers for the safe operation of accelerators and beamlines. A safety system control law is applied for the Beamline Personnel Safety System and realized based on fail-safe electronics. Dangerous events did not occur yet.

References

[1] N. Hiller, E. Huttel, A.-S. Müller, A. Plech, F. L. Müller, P. Peier, V. Schlott, *A setup for single shot electro optical bunch length measurements at the ANKA storage ring*, proceedings of IPAC2011, San Sebastián, Spain.

[2] T. Boltz, M. Brosi, E. Bründermann, P. Schönfeldt, M. Schwarz, M. Yan, and A.-S. Müller; "Studies of longitudinal dynamics in the micro-bunching instability using machine learning"; IPAC2018, Vancouver, BC, Canada

[3] https://www.youtube.com/watch?v=BztxS8pbxcM

[4] M. J. Nasse, M. Schuh, S. Naknaimueang, M. Schwarz, A. Plech, Y.-L. Mathis, R. Rossmanith, P. Wesolowski, E. Huttel, M. Schmelling, and A.-S. Müller, *FLUTE: A versatile linac-based THz source*, Rev. Sci. Instrum. 84, 022705 (2013), http://dx.doi.org/10.1063/1.4790431

[5] Zimina, A. et al. *CAT-ACT - A new highly versatile x-ray spectroscopy beamline for catalysis and radionuclide science at the KIT synchrotron light facility ANKA*. Review of scientific instruments, 88 (11), doi:10.1063/1.4999928, 2017

[6] Rothe, J.; Altmaier, M.; Dagan, R.; Dardenne, K.; Fellhauer, D.; Gaona, X.; González-Robles Corrales, E.; Herm, M.; Kvashnina, K.O.; Metz, V.; Pidchenko, I.; Schild, D.; Vitova, T.; Geckeis, H. *Fifteen Years of Radionuclide Research at the KIT Synchrotron Source in the Context of the Nuclear Waste Disposal Safety Case.* Geosciences 9, 91; https://doi.org/10.3390/geosciences9020091, 2019

[7] K. Cerff, D. Jakel, R. Stricker, M. Hagelstein, I. Birkel; *EVALUATION OF THE BEAMLINE PERSONNEL SAFETY SYSTEM AT ANKA UNDER THE AEGIS OF THE 'DESIGNATED ARCHITECTURE' APPROACH*, Proceedings of ICALEPCS2013, San Francisco, CA, USA

[8] www.pilz.com, PNOZ

[9] D. Jakel, *Functional safety at the NANO beamline for experimental research with synchrotron radiation*, batchelor thesis, 2013

[10] M. Brinkmann, *SafetyBUSp–the first safe fieldbus system – CAN in automation*, 2000

[11] D. J. Smith, K. G. L. Simpson, *The safety critical systems handbook*, Elsevier Ltd, 2011

[12] Huelke, M.; Hauke, M.; Pilger, J.: *SISTEMA: a Tool for the Easy Application of the Control Standard* EN ISO 13849-1, 2008

[13] M. Hauke et al, "Funktional safety of machine controls", BGIA Report 2/2008e

[14] www.pilz.com, PAScal Safety Calculator

[15] https://new.siemens.com/global/en.html

Design of the ThomX PSS – Use of a complete Safety PLC System

Harold BZYL[a], Pierre ROBERT[b], Jean-Michel HORODYNSKI[b]

[a] CNRS-IN2P3-IPNO, Centre Universitaire Paris-Sud, 15 rue Georges Clemenceau, 91406 Orsay
[b] CNRS-iRSD, Centre Universitaire Paris-Sud, Building 201 Door 1, BP34 91898 Orsay Cedex
October 2019

Abstract

ThomX [1] is a facility producing high-flux and high-energy X-rays using Inverse Compton Scattering effect between an electron beam (energy: $50-70\,\mathrm{MeV}$; charge by pulse: $1\,\mathrm{nC}$; repetition rate: $50\,\mathrm{Hz}$) and a highly amplified laser (Fabry-Perot cavity [2]). This facility could be used as an intermediate light source between synchrotron facilities and conventional X-rays sources. The compacity of the accelerator (greater diagonal of about $7\,\mathrm{m}$ length) is a key feature in order to be used in sensitive areas, for instance hospitals, museums.

ThomX is located in the same building as another accelerator, Andromede[3] (Van der Graaf Generator accelerating protons, nanoparticles of gold or fullerenes up to 4 MeV). Both facilities will be used independently while workers could go in the common area between the two hutches. Thus, the biological shielding is designed in order to comply with the radiation protection objectives [4] and the PSS is designed to comply with the exploitation constraints. In the same time, the use of a beamline for X-rays and the needs to operate on various critical sub-systems (like the Fabry-Perot cavity or the pulsed magnets) imply a complex safety design to cover the entire scope of maintenance and exploitation mode.

Use of safety PLC to design PSS for light source facilities is constantly rising. The main advantages of this kind of systems are real-time auto-checking and diagnostic of the complete system, flexibility and ease for upgrade. Feedbacks showed the high robustness and availability of safety PLC. Thus, the ThomX and Andromede PSS design is completely based on the use of safety PLC and SIL-3/PLe relays. Interconnexion between the Profinet compliant devices is based on an MRP ring to ensure continuous communication even with a single link failure. This system complies with the current French standard for accelerators PSS conception (NF M 62-105 [5]) but its innovative design will lead the incoming new version.

1 ThomX, a compact Compton backscattering X-rays source

Various applications needs high-flux and high-energy X-rays, for instance chemical analysis [6], medical diagnostic or therapy [7,8], crystallography[9], radioactive waste management [10] or museology [11]. The aim of ThomX is to demonstrate the feasibility of a compact facility producing X-rays up to 45-90 keV with a flux up to 1013 photons per second (Fig. 1) using the Inverse Compton Scattering effect. A LINAC will produce electrons up to 50 MeV (70 MeV in a future upgrade) whose are injected then into a ring. At the interaction point, electrons will interact with a highly amplified laser (thanks to a Fabry-Perot cavity) to produce x-rays in the opposite direction of the laser photon (Fig. 2).

The machine will soon start the commissioning phase as soon as the French authority (ASN – Autorité de sureté nucléaire) gave the license to use the acceleratorq. The shielding design will provide a complete lack of radiative exposure for people outside the main building, called Igloo. Outside the ThomX bunker, monitored area will be delimited when the accelerator will be on (Fig. 3).

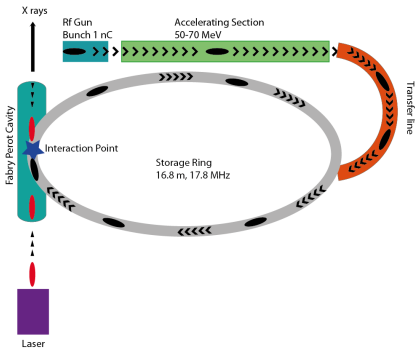

Figure 1: Schematic design of the ThomX accelerator. Electron produced by the photocanon (RF gun) are accelerated by the accelerating section. A transfer line injects the primary beam into the storage ring. Bunch are stored during 20 ms in the ring and will collide with the amplified laser at the interaction point to produce X-rays by Compton backscattering effect.

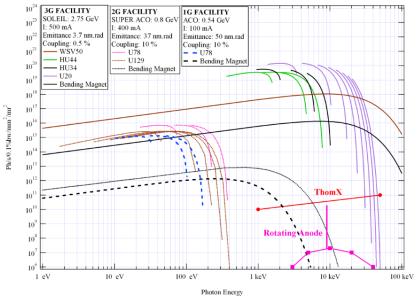

Figure 2: Photon flux vs energy for different synchrotron facilities [2] compared with ThomX performances. X-rays flux and energy produced by the ThomX facility are intermediate between synchrotron facilities and commercial X-rays generators.

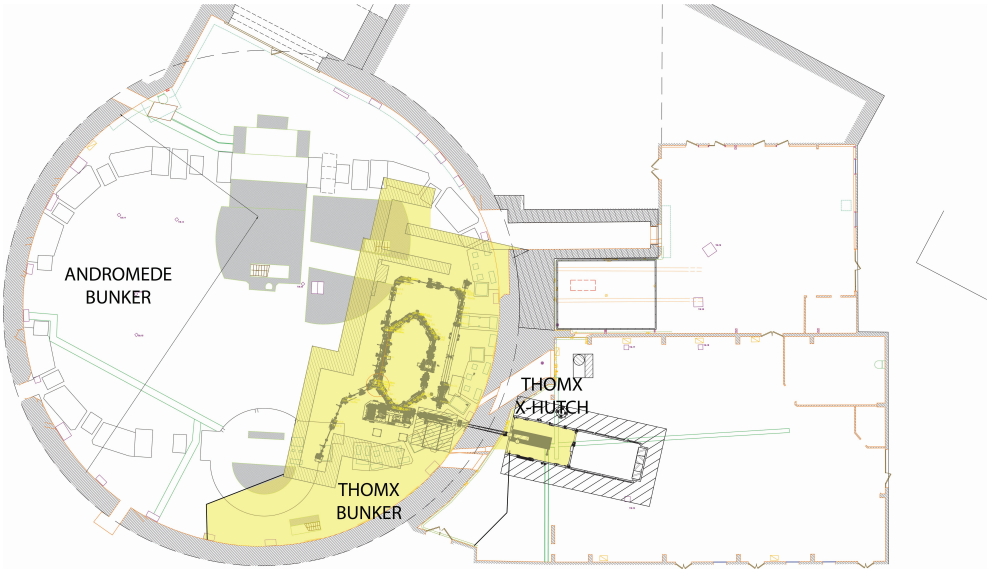

Figure 3: *Actual view of the ThomX accelerator into its bunker (shielding design process described in [2]). The ThomX Bunker is located inside the Igloo with another accelerator called Andromede. X-rays produced will be characterized and used into the X-Hutch.*

2 Safety PLC system for particle accelerators

The aim of a PSS for particle accelerators is to forbid people to be inside the irradiation area of a machine when it is on and to ensure the safety of the surrounding areas. Technologies mainly used to design these systems are based on mechanical and electromechanicals interlocks, locked keys and relays, all connected with wired logic. French standards were edited (NF M 62-105, current version in 1998, a new version is pending) giving the recommendations to design an efficient PSS for particle accelerators. It must be designed following those rules: forbidden access to areas where irradiation occurs; positive safety, meaning that protections occurs in case of failure acting directly on the accelerating field; redundancy of security devices.

PLC systems can manage automated systems by controlling the signals coming from detectors and communicating with actuators following a programmable logic. This kind of devices is widely used in industrial applications to control automated processes. Safety PLC (Fig. 4) were created in order to control safety processes with two more goals than simple PLC: the system must not fail, if not the system must fail in a safe

and predictable way. They look like the same as PLC, but part of the software is dedicated to managing safety aims as well-functioning status of detectors/actuators, communications between devices, integrity of PLC and detectors/actuators. In the same time, it needed to use devices with a high-level of performance and integrity to ensure the weakest percentage of failure. Then standards were defined to design safe and reliable safety systems based on safety PLC (IEC 61508 [12], IEC 62061 [13], ISO 13849 [14], ISO 14119 [15] and others).

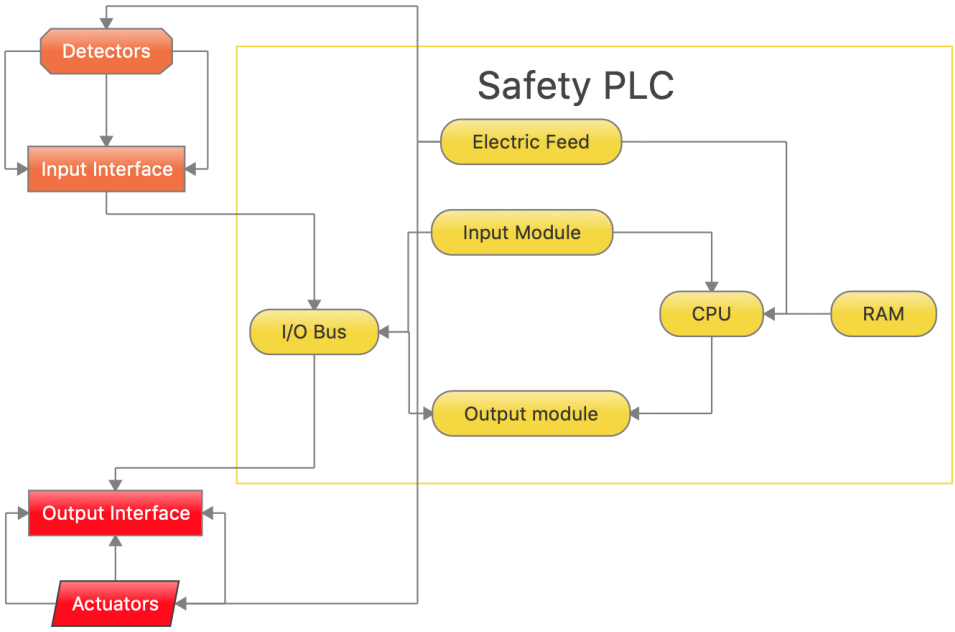

Figure 4: *Safety PLC topology. Yellow shapes are the main components of the safety PLC. Orange shapes are detectors, red ones are actuators.*

For particle accelerators, the more predictable way to reach the best level of safety is to stop the production and the acceleration of particles or the accelerating fields. Thus, safety PLC must act on sub-systems related to the production of particles or accelerating fields like guns, RF sources... based on positive safety to manage the access of the irradiation areas of the facility.

3 Design of the ThomX PSS

Based on the feedbacks of use of safety PLC systems for PSS in various facilities (ALTO (CNRS/IN2P3/IPNO, Orsay), CLIO (CNRS/INC/LCP, Orsay)) and availability of devices compliant with high level of safety performances (PLx/SILx), choice was made to design the PSS of ThomX and Andromede based on a complete safety PLC system. The following criteria were critical too for the decision to be made:

- The PSS needs to evolve with the facilities: creation of new beamlines, use of the machines for new applications... Safety PLCs could easily be modified following an iterative process of software development to ensure at least the same level of safety as the initial one.
- As the facilities were conceived from scratch, an innovative PSS could be designed.

The first step to define the design of the PSS was to assess the risks related to the facility and the personal safety in order to define the level of PLx/SILx needed for the safety devices. A conservative choice was made to reach the best level of safety: PLe and SIL3.

Next was the design of the PSS itself based on:

- the different areas and their accesses; in the case of ThomX, two hutches needed to be managed altogether

with a shared building with Andromede facility inside, underground corridors... a common area was defined in addition to the two hutches in the Igloo building (Fig. 5).

- the critical sub-systems for personal safety: X-rays beamline, RF source, Fabry-Perot and photocathode lasers, dipoles of the ring;
- the Radiation Monitoring System;
- the other safety systems;

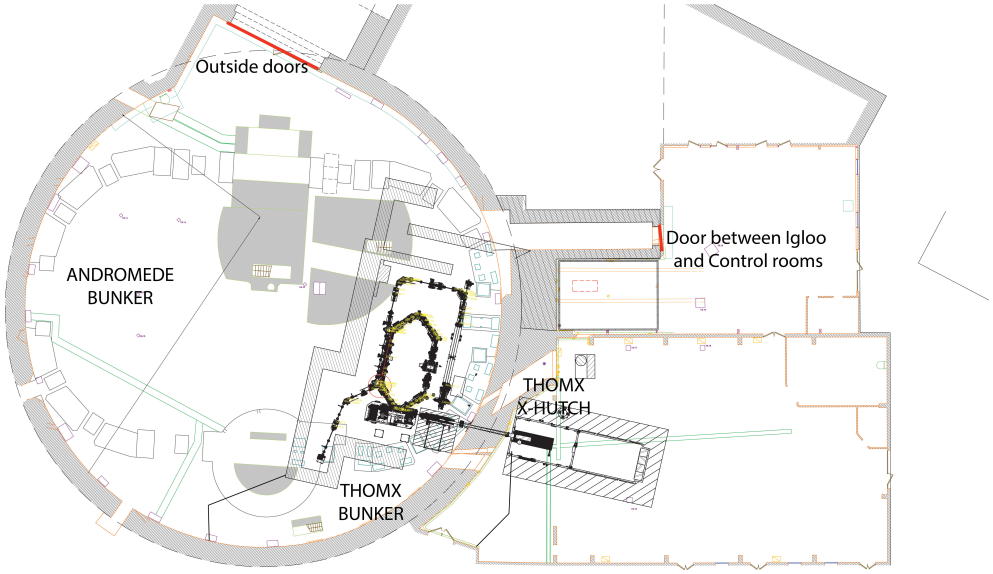

Figure 5: *Top view of the Igloo building and the surrounding areas. Location of the doors (in red) for the common area between ThomX and Andromede hutches.*

This step needs the contribution of all the project team to express all their needs and constraints to identify the detectors/actuators needed and to define the different exploitation mode (restricted access, identification of dangerous combination of sub-systems that could produce ionizing radiations if used in the same time...). As the project evolve, the design needs to be reviewed periodically to check the compliance with the high level of safety defined.

The logic of the ThomX PSS is described on the figure below (Fig. 6). Detectors were defined for each bunker, accelerator and X-rays experimental line. In case of failure, meaning wrong configurations, actuators dysfunctions or communication failure, the safety PLC will act on the different interlocks placed on the different sub-systems producing accelerating fields and primary beam. In the case of the X-hutch, one more interlock was added to close the X-shutter and to forbid the possibility to move it.

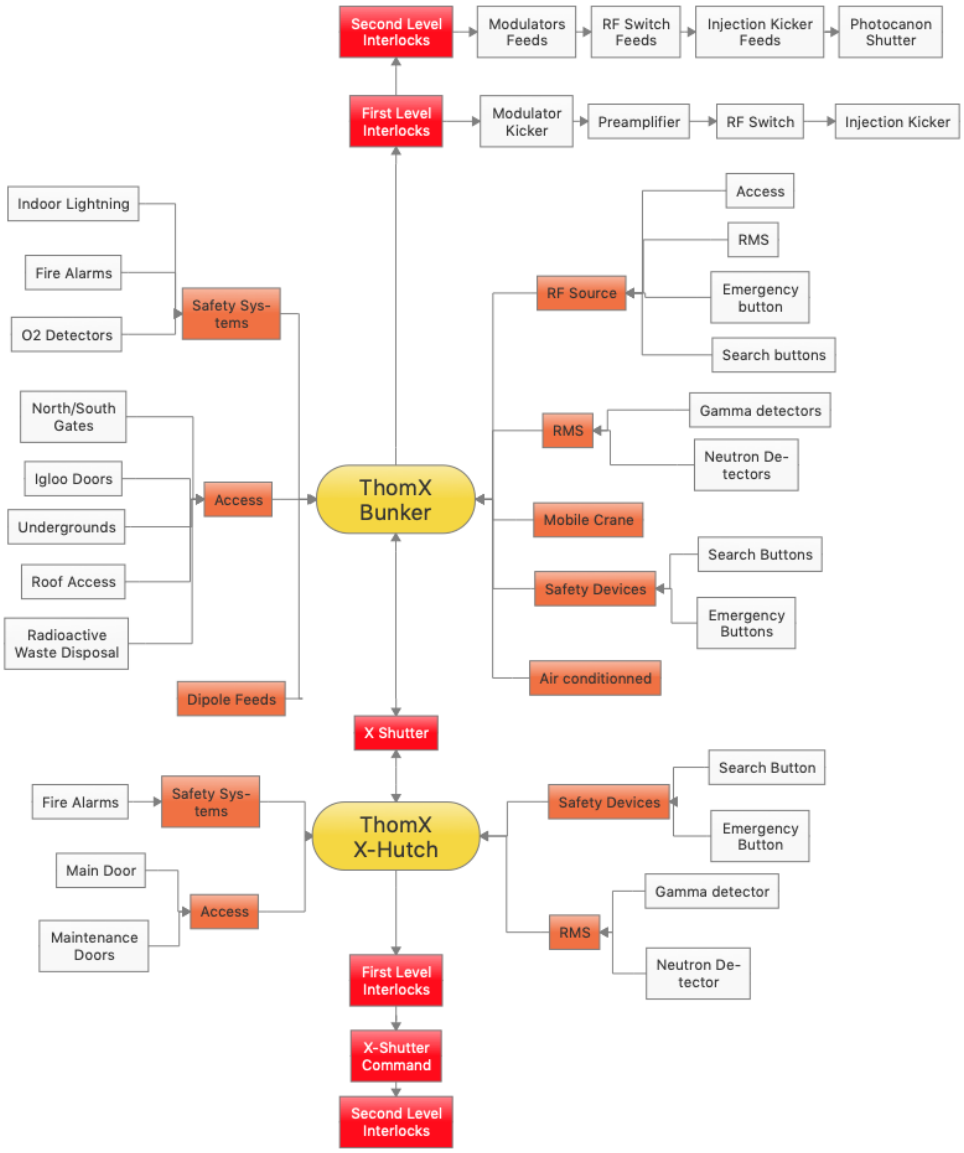

Figure 6: *Detectors (in orange) and actuators (in red) logic for the ThomX PSS. Two areas have been defined, one for each bunker (in yellow).*

Accesses to the bunkers are managed with two kind of locking: locked keys for technical access, as caged ladder for instance, and electromechanical locking (Fig. 7 - Fig. 8) for the inside doors (access to the bunker...). In addition to that, two position detectors, based on RFID with encrypted keys (SIL3/Ple) are put on each door. Despite the use of electromechanical and mechanical systems, exit of people inside areas are always possible thanks to emergency push-button on every locks.

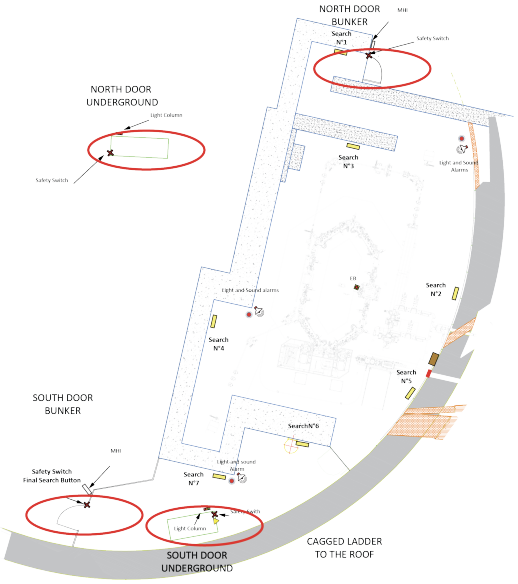

Figure 7: Location of electromechanical locking around the ThomX accelerator bunker (red circles).

Figure 8: North door of the ThomX accelerator bunker. The electromechanical locking indicates the status of the access (green light: authorized access; red light: access denied). In the right side, a screen indicates different status related to the PSS (access and search status) and the RMS (dose rate in real-time)

Monitored and exclusive accesses have been defined: authorized workers could enter the ThomX accelerator hutches without deactivating search buttons for short-time operations. Very strict conditions have been defined:

- In case of monitored acces, the accelerator is shutdown and cannot be restarted;
- At least two workers must access the hutch, each carrying an identified key (monitored access keys - Fig. 10). Keys are only freed if the accelerator is off and the gamma detector inside the hutch measure dose rate complying with the radiation protection zoning.
- Only the South access could be used. This door could only be opened if at least two monitored access keys are removed. If the door is opened after the first authorization, then search buttons are deactivated.
- In exclusive mode, only two workers could enter into the accelerator hutch. Access is authorized only with specific keys (exclusive access keys).

The ThomX PSS managed maintenance mode too. For some sub-systems, maintenance work needs to be done with interlocks shunted e.g. with the possibilities to feed the sub-systems parts when the accelerator is shutdowned. For this purpose, safety keys are used in order to put the facility into maintenance mode (Fig. 9). In this case:

- the accelerator is shutdowned and cannot be restarted until all the keys are returned to exploitation mode locks;
- only precise combinations of maintenance mode is authorized. For instance, it is impossible to put the preamplifier and the modulator in maintenance mode in the same time. In this case, every sub-systems are shutdowned.

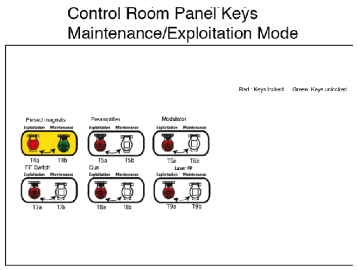

Figure 9: Panel keys managing the maintenance and exploitation mode for some sub-systems. This panel is located inside the ThomX control-command room.

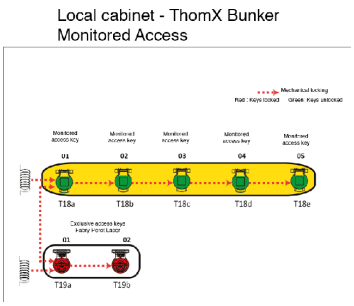

Figure 10: Panel keys managing the monitored and exclusive accesses to the ThomX accelerator hutch.

HMI developed for the ThomX PSS is designed to help the operators easily identified any failures on the sub-systems managed by the PSS (Fig. 11). A diagram indicate the status of each sub-system. Clicking on a red circle (directly on the touchscreen) indicates the different state managed by the PSS as the well-functionning status and the real state of the detectors. Other screens indicate the RMS status, the status of the positions detectors on each access, and the status of the PSS.

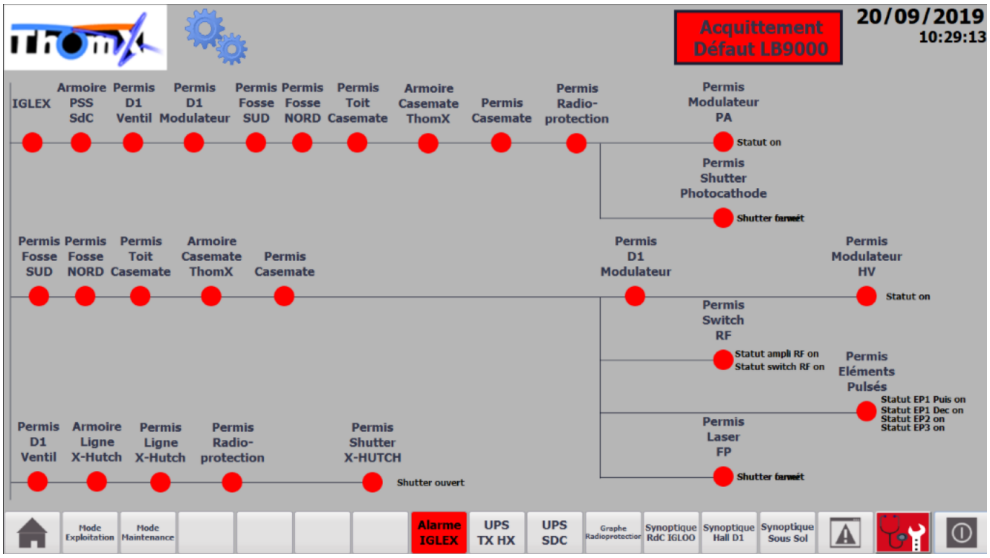

Figure 11: *HMI screen in the ThomX Command-control room. Each red circle indicate the status of one sub-system. Clicking on it give the status of the different detectors related to the sub-systems. The accelerator could be started only if the five first red circle at the end of the tree are totally green.*

4 First feedbacks

The first campaign of test validation for the PSS was done at the end of July 2019. Some minor tweaks needed to be made in order to improve the PSS design, especially the HMI. Nevertheless, some detectors were not yet ready to be tested so the PSS was not validated. A new campaign will be made in October 2019 with the missing detectors.

Use of PSS based exclusively on Safety PLC systems is rising on particle accelerators as the feedbacks on their reliability and safety are mainly positive: for instance, MAX IV (Lund, Sweden) [16], CEBAF (Newport News, USA) [17,18], ALBA (Barcelona, Spain), CEMTHI (Orléans, France). French nuclear authority changed their minds on the use of safety PLC for PSS design as standards are now well defined and positive feedbacks came from other industries. The work done with the ThomX PSS is used as a feedback for the new version of the French norms regarding the design of PSS for particle accelerators.

References

[1] A. Variola, J. Haissinski, A. Loulergue et F. Zomer, ThomX : Technical design report, Orsay: LAL, 2013.

[2] J. Bonis, R. Chiche, R. Cizeron, M. Cohen, E. Cormier, P. Cornebise, N. Delerue, R. Flaminio, D. Jehanno, F. Labaye, M. Lacroix, R. Marie, B. Mercier, C. Michel, Y. Peinaud, L. Pinard, C. Prevost, V. Soskov, A. Variola et F. Zommer, *Non-planar four-mirror optical cavity for high intensity gamma ray flux production by pulsed laser beam Compton scattering off GeV-electrons*, Journal of instrumentation, Janvier 2012.

[3] M. J. Eller, E. Cottereau, V. Verkhoturov, A. Delobbe, J. Renaud, E. A. Schweikert et S. Della-Negra, *Andromede Project : Surface analysis and nano-particle surface interactions in the keV to Mev Energy Range*, Leuven, 2014.

[4] J.-M. Horodynski and S. Wurth, "Shielding Design and Radioprotection for Andromede and ThomX accelerators," no. EPJ Web of conferences, 2016.

[5] AFNOR, Accélérateurs industriels - installations, Paris: AFNOR, 1998.

[6] M. Cotte, E. Welcomme, V. A. Solé, M. Salomé, M. Menu, P. Walter et J. Susini, *Synchrotron-based X-ray spectromicroscopy used for the study of an atypical micropigment in 16th century paintings*, Analytical Chemistry, vol. 79, pp. 6988-6994, 15 septembre 2007.

[7] P. Suortti et W. Thomlinson, *Medical applications of synchrotron radiation*, Physics in medecine and biology, vol. 48, No 13, 7 juillet 2003.

[8] M. Ando, E. Hashimoto, H. Hashizume, K. Hyodo, H. Inoue, T. Kunisada, A. Maksimenko, K. Mori, E. Rubenstein, J. Roberson, D. Shimao, H. Sugiyama, K. Takeda, F. Toyofuku, E. Ueno, K. Umetani, H. Wada et W. Pattanasiriwisawa, *Clinical step onward with X-ray dark-field imaging and perspective view of medical applications of synchrotron radiation in Japan*, Nuclear instruments and methods in physics research, vol. 548, N^o 11-2, pp. 1-16, August 2005.

[9] P. Mc Gee, *Automating, miniaturizing X-ray crystallography*, 09 juin 2007. [En ligne]. Available: http://www.dddmag.com/articles/2007/09/automating-miniaturizing-x-ray-crystallography. [Accès le 25 février 2015].

[10] R. Hajima, T. Hayakama, N. Kikuzawa et E. Minehara, *Proposal of nondestructive radionuclide assay using a high-flux gamma-ray source and nuclear resonance fluorescence*, Journal of nuclear science and technology, vol. 45, N^o 15, pp. 441-451, mai 2008.

[11] L. De Viguerie, P. Walter, E. Laval, B. Mottin et V. Armando Solé, *Revealing the sfumato technique of Leonardo da Vinci by X-ray fluorescence spectroscopy*, Angewandte chemie, vol. 49, N^o 13, pp. 6125-6128, 16 août 2010.

[12] IEC, Functionnal safety of electrical/electronic/programmable electronic safety-related systems, Geneva: IEC, 2005.

[13] IEC, IEC 62061 - Safety of machinery - Functionnal safety of safety - related electrical, electronic and programmable electronic control systems, Geneva: IEC, 2015.

[14] ISO, ISO 13849-1 - Sécurité des machines - Parties des systèmes de commande relatives à la sécurité, Genève: ISO, 2015.

[15] ISO, ISO 14119 - Safety of machinery - Interlocking devices associated with guards - Principles for design and selection, Geneva: ISO, 2013.

[16] A. Rosborg, *The MAX IV personnel safety system,* chez Ninth International Workshop on Radiation Safety at Synchrotron Radiation Sources, Hsinchu, 2017.

[17] K. Mahoney et H. Robertson, *Jefferson Lab IEC 61508/61511 Safety PLC Based Safety System,* chez Proceedings of ICALEPCS2009, Kobe, 2009.

[18] Jefferson Lab - Safety Systems Group, *Jefferson Lab Personnel Safety Systems - Systems Requirement Specification,* Jefferson Lab, Newport News, 2015.

Comparison and Expansion of Semi-Empirical Shielding Formulas with FLUKA Calculations

H. Huck, K. Ott

Helmholtz-Zentrum Berlin, BESSYII, Berlin, Germany
October-2019

Abstract

In the advent of diffraction-limited storage rings (DLSR) [1], long-term plans for a possible successor of the BESSY II storage ring are under investigation. Such a facility would have a significantly reduced beam lifetime compared to a standard third-generation light source, placing stringent requirements on radiation protection, especially on controlling the annual number of injected electrons per year and on shielding design.

A complex facility like this cannot be simulated in total and in necessary detail in a reasonable time frame. Therefore, semi-empirical shielding formulas [2-6] can be an essential tool for designing an overall shielding concept. Existing formulas had been mostly devised for and fitted to different parameter regimes than those common to next-generation light sources. In this paper, we present recent FLUKA [7, 8] simulations tailored to adapt the existing formulas to the specific needs of a possible BESSY II successor. For example, source terms for niobium, and the giant resonance neutron yield as function of target length for different materials are derived.

1 Shielding formulas

Shielding formulas to estimate the dose equivalent of ionizing radiation behind the shielding wall of an electron accelerator have been devised decades ago. They all share some general assumptions, in particular a single point source of ionizing radiation and simple exponential attenuation in the shield. Usually, with the exception of beam dump formulas, no attenuation in the target and no additional source or build-up in the shield are considered. The simplest form of a shielding formula consists of a source term S specific to the loss scenario and radiation type, a $1/r^2$ dependency for isotropic sources, and an exponential decay in the shielding material:

$$H = \frac{S}{r^2} \exp\left(\frac{-d}{\lambda}\right) \tag{1}$$

with the shielding thickness d seen by the radiation and the attenuation coefficient λ depending on shielding material, radiation type and spectrum. In general, S depends on target material, geometry and observation angle, but sometimes a conservative maximum or average is chosen. While most literature treats S and the resulting dose equivalent H as proportional to the primary electron energy, this is only true for rather limited parameter ranges due to varying cross sections and mean free paths.

In this paper, we will focus on the neutron dose behind a lateral (i.e., not in forward direction of the primary particle beam) shielding of an electron accelerator. Corresponding formulas have been published e.g. by Tesch [3, 4], in the NCRP report No. 144 [9], and in the Landolt-Börnstein Vol. 11 [6]. We will quote here the last one (eq. 2), since it is the most comprehensive and detailed one, and - according to our simulation results - also the most accurate one, as presented later:

Table 1: *Giant resonance source terms Sn for different target materials [6]. The value for Niobium was derived by scaling the value for Lead with our simulation results from table 2.*

	Al	Fe	Cu	Nb	W	Pb
S_n [Sv cm^2 / GeV^{-1}]	6.0e-12	7.7e-12	1.1e-11	1.7e-11	2.0e-11	1.9e-11

$$H_T\,[Sv/h] = \frac{3600 \cdot I_s \cdot E \sin^2\theta}{(a+d)^2}\Big[1.1 \cdot 10^{-12} \ln Z e^{-1.9\theta} t^{0.19 \ln\theta + 2.35} e^{\frac{-\rho d}{\sin\theta \cdot \lambda_g}} + S_n e^{\frac{-\rho d}{\sin\theta \cdot \lambda_n}} + \frac{7.5 \cdot 10^{-13}}{(1-0.75\cos\theta)^2 M^{0.4}} e^{-\rho d} \sin\theta \cdot \lambda_h\Big] \tag{2}$$

In eq. 1, the thickness d [cm] of the shielding wall and its distance a [cm] from the beam pipe are measured perpendicularly, regardless of the observation angle θ [rad]. Is is the electron beam intensity in s^{-1}, E its energy in GeV, Z and M the atomic number and mass of the target material, t the length of the target in radiation lengths, and ρ the shielding wall density in g/cm^3. The three terms within the brackets correspond to the dose contribution due to bremsstrahlung, giant resonance neutrons and high energy neutrons, with their attenuation coefficients λ_g, λ_n and λ_h, respectively. The giant resonance source term S_n can be taken from table 1.

Eq. 1 is valid for an energy range from 1 to 1000 GeV and for observation angles between 30 and 120 deg. While the giant resonance source term is isotropic, the high energy neutron source term is about 8 times larger at 30 deg than at 90 deg. Only the photon term depends on the length of the target.

2 Neutron yield vs. target size

Existing shielding formulas for neutrons hardly or not at all take into account target geometry and material. We conducted dedicated FLUKA simulations to analyze the dependence of the neutron source term on these parameters, set up as follows. 3 GeV electrons hit the front side of a cylindrical target of varying length and diameter, placed in vacuum, and the resulting neutron yield was evaluated separately in a low (LEN) and high (HEN) energy group, with the energy cut at 20 MeV. The left plot in fig. 1 shows this neutron yield as function of target radius for an Iron target with a fixed length of 20 radiation lengths X_0 (approx. 35 cm). The HEN maximum is located at about 1 Moliere radius r_M, the LEN maximum at approx. 4 r_M. LEN production depends much more on target size, it clearly needs more space, but for thin rods (r<4 mm) also the HEN yield drops significantly. Furthermore, grazing incidence on a 2 mm vacuum chamber wall (open circles in fig. 1) yields even less than perpendicular incidence on a cylinder with 0.86 mm radius, namely 15 % and and 45 % of the maximum LEN and HEN yield, respectively.

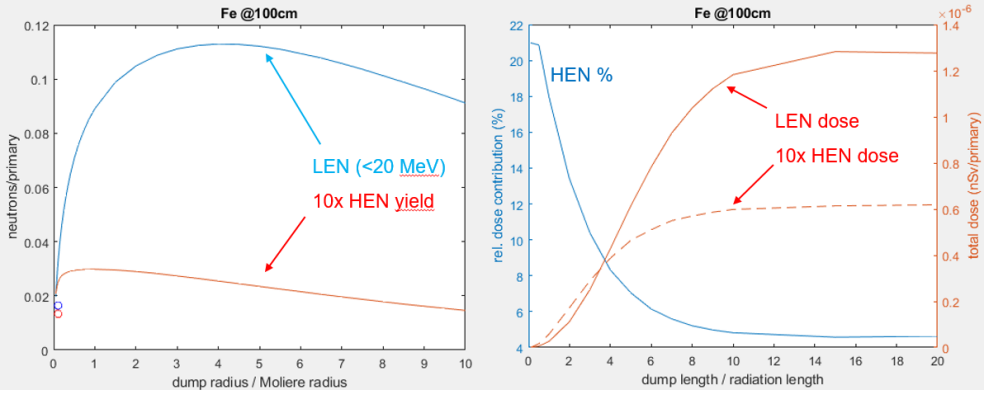

Figure 1: *Neutron yield per primary electron vs. target radius in units of the Moliere radius for a* 35 cm *long cylindrical Iron target (left), neutron dose per primary vs. target length (right, red), and HEN contribution to the total dose (right, blue). The open circles in the left plot refer to grazing incidence on a 2-mm chamber wall.*

A target length scan for a cylindrical Iron target with a radius of 1 Moliere radius is shown in the right plot of fig. 1. Here as well the high energy neutrons are generated earlier, with their contribution to the total dose dropping from 20 % to 5 %, but a significant target length dependence exists for both neutron groups. This dependence is investigated in more detail in fig. 2-4. Here, the total neutron yield leaving cylindrical targets (r = 2 r_M) made of different materials is plotted versus the target length X. The top plots (fig. 2) are normalized to the maximum yield at X = 30 X_0, the center plots (fig. 3) show a zoomed view up to X = 1 X_0, and in the bottom plots (fig. 4) both axes feature absolute units.

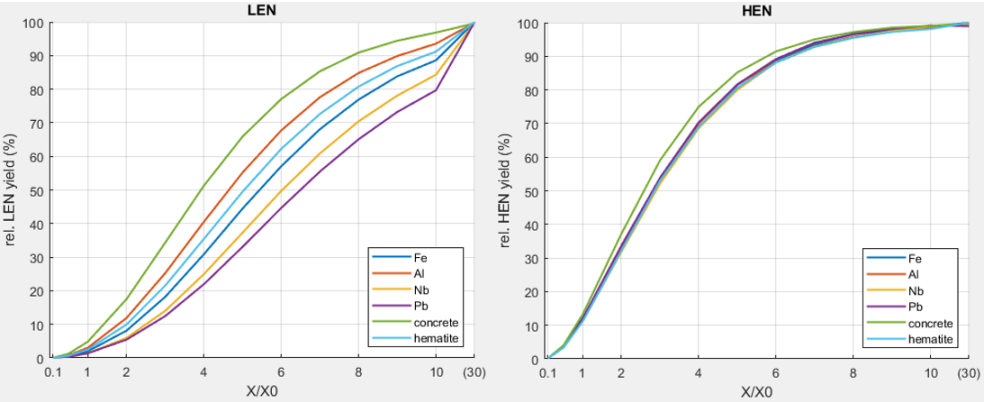

Figure 2: *Relative neutron yield (target efficiency factor) from cylindrical targets (r = 2 r_M) as function of target length X normalized to the radiation length X_0, for targets made of Iron, Aluminum, Niobium, Lead, normal and heavy concrete (hematite).*

These curves can be used as "target efficiency factor" for the neutron terms in semi-empirical shielding formulas. Note that even for the high energy neutrons, which are generally considered to be generated very early in the cascade, the target efficiency drops below 50(5)% at approx. 3(0.6) X_0, corresponding to an Iron target of (5 ± 1) cm thickness. For the giant resonance neutrons, the 50 % and 5 % levels vary depending on target material, between 4.0-6.5 X_0 and 1-2 X_0, respectively. The maximum yield depends on target material, and is summarized in table 2. These HEN data are in good agreement with Dinter [10] and with the (1/M$^{0.4}$)-scaling from eq. 1 [6]. The LEN data are somewhat higher than [10], but in very good agreement to Swanson [11]. Unlike proposed in literature [6], ordinary concrete does not yield the same amount of giant resonance neutrons as aluminum, but rather three times less.

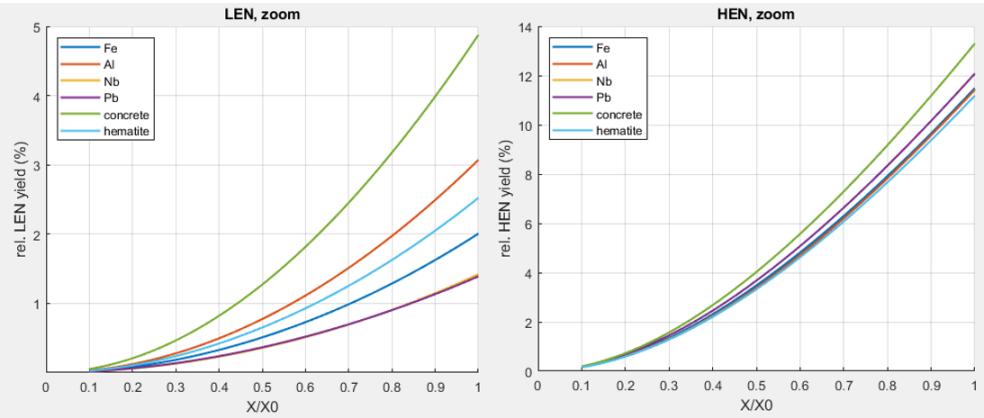

Figure 3: *Zoomed view of fig. 2.*

Table 2: *Maximum (i.e. for thick targets, compare fig. 4) low- and high-energy neutron yield per primary electron from different materials, normalized to* 1 GeV. *The last two rows show the yield of grazing incidence (1 mrad) electrons on a 2-mm target, normalized to the first two rows.*

	Al	Fe	Cu	Nb	concrete	hematite
LEN pp/GeV	0.17	0.11	0.32	0.36	0.04	0.11
HEN pp/GeV	6.0e-3	9.0e-3	5.0e-3	3.9e-3	8.6e-3	7.2e-3
LEN/HEN	28	12	64	92	5	15
g.i. LEN %	15%	8%	16%			
g.i. HEN %	45%	33%	48%			

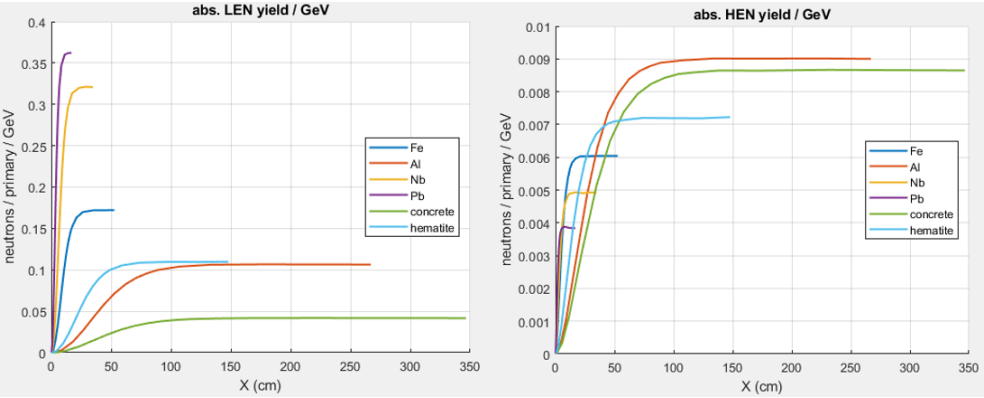

Figure 4: *Neutron yield per GeV from cylindrical targets (r = 2* r_M*) as function of target length in absolute units.*

3 Neutron doses behind lateral shielding

At synchrotron light sources, almost all electrons are lost not on thick targets, but on either the residual gas or the vacuum chamber wall, typically 2 mm thick. Forward doses are usually dominated by photons, but the dose behind the lateral shielding walls by neutrons. For a more accurate dose estimation, it is worthwhile to compare shielding formulas with simulations of these lateral neutrons originating from a thin chamber wall.

Table 3: *Neutron attenuation coefficients for concrete in g/cm^2. Best average values for* $50-200\,\mathrm{cm}$ *shielding strength and neutron spectra resulting from* $3\,\mathrm{GeV}$ *electrons lost on different target materials (first four columns). The last three columns show literature values.*

	Al	Fe	Cu	Nb	[6]	[3,4]	[9]
λ_n (LEN)	55	48	46	42	42	40	30-55
λ_h (HEN)	118	118	118	118	117	100	55-120

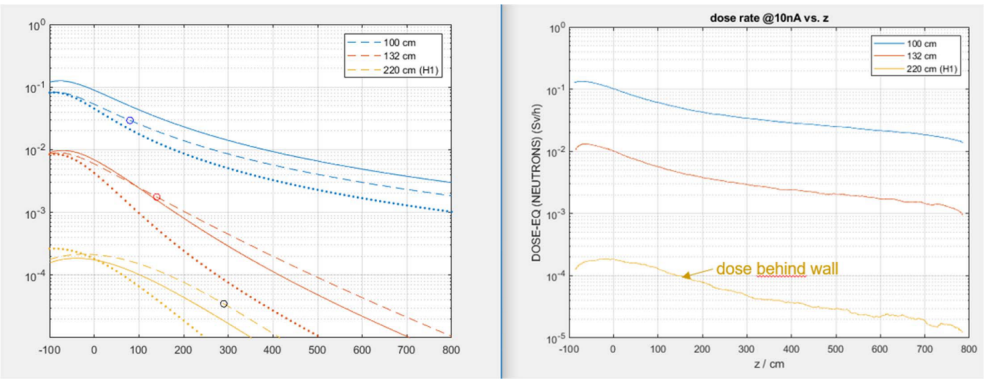

Figure 5: *Lateral neutron doses in front of (blue), inside (red) and behind (yellow) a* $100\,\mathrm{cm}$ *thick concrete wall vs z, the longitudinal position along the wall. The target is a* $2\,\mathrm{mm}$ *thick Iron chamber wall hit by* $3\,\mathrm{GeV}$ *electrons at one meter distance from the wall. The right image shows results from FLUKA, the left image the corresponding results from the shielding formulas given by the NCRP report [9] (solid lines), Landolt-Börnstein [6] (eq. 1, dashed lines) and Tesch [3, 4] (dotted lines), modified with the grazing-incidence correction factors from table 2.*

In a first step, we applied the grazing-incidence correction factors from table 2 to Eq. 1 and to the formulas from [3, 4] and [9], and plotted the resulting total neutron dose as a function of the longitudinal coordinate z (fig. 5). All curves agree well with the FLUKA results in the 30-120 degree range, and much better than they would without the correction factors. The best agreement behind the wall shows the Landolt-Börnstein formula (eq. 1), which was used for the following investigations.

Since shielding design should always be conservative, not the $1\,\mathrm{mrad}$ case but rather the angle of incidence which yields the highest dose rate outside the shielding wall is of special importance. Therefore we conducted further simulations of a $3\,\mathrm{GeV}$ electron beam hitting a 2-mm vacuum chamber wall at angles varying between $1\,\mathrm{mrad}$ and 2 deg. Furthermore the strength of the concrete wall was varied between $50\,\mathrm{cm}$ and $200\,\mathrm{cm}$, in order to find the best average attenuation coefficients for the two neutron groups under these conditions. All this was done for the four most prominent vacuum chamber materials Aluminum, Iron, Copper and Niobium. Simulation results were evaluated as curves of neutron dose vs. z at fixed lateral coordinate, the dose averaged at each z over $5\,\mathrm{cm}$ on the lateral axis and over $10\,\mathrm{cm}$ on the other axes. Two curves were then fitted simultaneously to each simulation result at two distances: The first curve (GR dominated) always $50\,\mathrm{cm}$ away from both the pipe and the wall, in order to minimize both the errors due to backscattering and to finite source size, and the second curve (HEN dominated) at observation distances varying between $20\,\mathrm{cm}$ behind the wall and $390\,\mathrm{cm}$ lateral distance from the beam pipe. The fit functions were the sum of the low- and high-energy neutron terms of eq. 1, but each term scaled with a separate correction factor as fit parameter. Alternatingly, the fits were done with fixed correction factors but variable attenuation coefficients.

While the resulting attenuation coefficient for the high-energy group averages to $118\,\mathrm{g/cm^3}$ (in agreement with [6]) for all target materials, the coefficients for low-energy neutrons were different for each target material, but did not change too much by observation distance and wall strength. The averaged values are summarized in table 3 together with values from literature.

The fitted correction factors to eq. 1, which can be understood as target efficiency factors, are plotted in fig. 5-7 versus the angle of incidence. For a conservative shielding design, we recommend to use the maxima of these

Table 4: *Maximum target efficiency factors (fig. 6) for neutrons generated by* 3 GeV *electrons lost on a 2-mm vacuum chamber wall.*

	Al	Fe	Cu	Nb	Cu (1 mm)
f_n (LEN)	0.085	0.275	0.245	0.239	0.158
f_h (HEN)	0.83	0.97	1.03	0.92	1.0

plots, summarized in table 4, together with the best average attenuation coefficients from table 3, as extension of eq. 1. With these modifications, the validity of the formula is also extended from "the surface of the shielding" as stated in [6] to arbitrary observation distances up to at least four meters from the target.

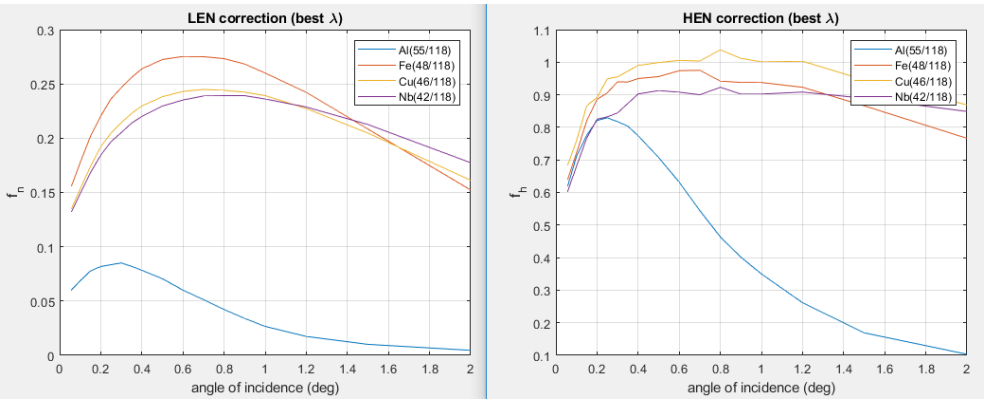

Figure 6: *Neutron correction ("target efficiency") factors for a 2-mm thick target, obtained by using the optimized attenuation coefficients.*

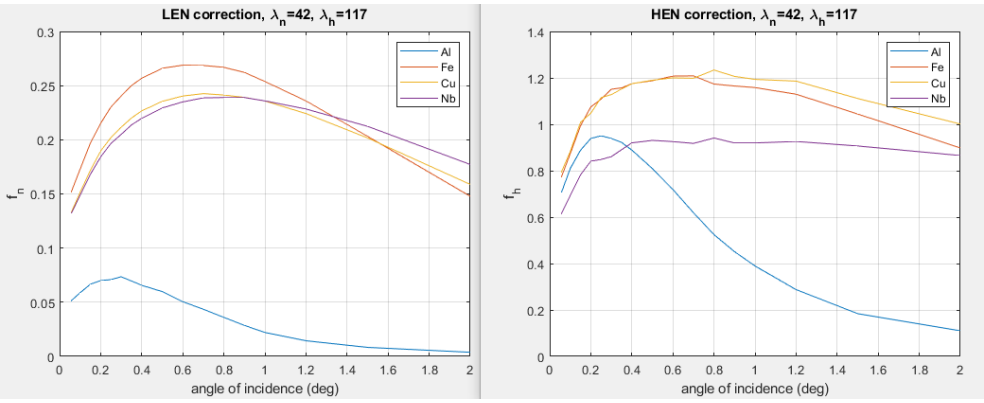

Figure 7: *Neutron correction ("target efficiency") factors for a 2-mm thick target, obtained by using the original Landolt-Bŕnstein attenuation coefficients.*

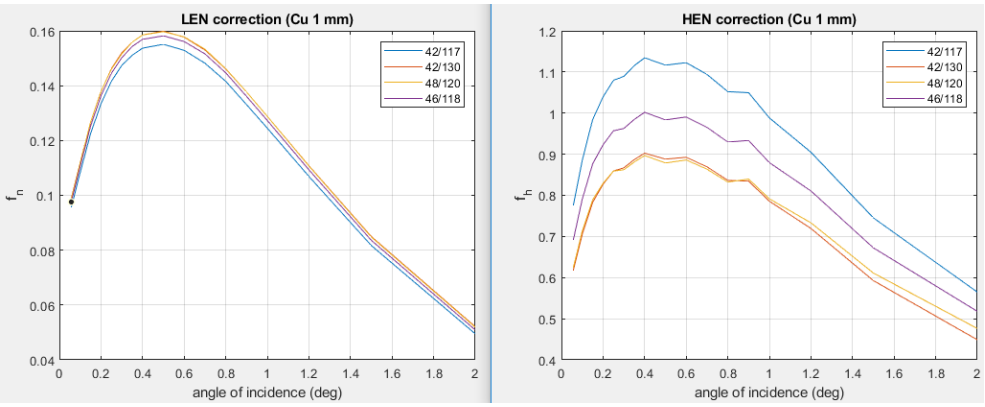

Figure 8: *Neutron correction ("target efficiency") factors for a 1-mm thick copper target, obtained by using four different combinations of attenuation coefficients ("42/117" are the original Landolt-Börnstein values).*

4 Lateral EM doses

For the common electron loss scenario described above (between 1 mrad and 2 deg incidence on $2\,\mathrm{mm}$ vacuum chamber wall), the dose equivalent due to bremsstrahlung and electrons does not seem to be modeled very well by existing formulas, although [2] and [6] (eq. 1) take into account target material and thickness. In fact, we observed much larger discrepancies (than for the neutron terms) between our simulation results and the predictions from [2], [6] and [9], both in magnitude and in shape of the curves (dose vs. z). The discrepancies are largest for grazing incidence, since the model of a single point source, the base of all formulas, is not valid here.

Without giving a detailed analysis, it seems that entering a fixed target length of approx. $4\,\mathrm{cm}$ into eq. 1, instead of the actual value which depends on the angle of incidence, gives the best agreement to simulations with $3\,\mathrm{GeV}$ electrons hitting a 2-mm iron chamber wall at various angles.

5 Conclusion

We conducted extensive FLUKA simulations to analyze the dependence of the lateral neutron dose on target geometry and material, with a focus on a loss scenario common to electron storage rings, the grazing incidence on a thin vacuum chamber wall. Several semi-empirical shielding formulas were compared to the simulation results. By fitting the one from Landolt-Börnstein [6] (eq. 1) to the results, we obtained target efficiency factors for the low- and high-energy neutron terms, as well as target-material dependent (i.e. spectrum dependent) attenuation coefficients for the low-energy group.

For practical purposes, we recommend to use eq. 1 with an unmodified high-energy neutron term, but with the giant-resonance source terms from table 1 multiplied with the correction factors from table 4, and attenuated with the values from table 3. For the EM term, we recommend a fixed t=2.5. These recommendations are for the estimation of the dose equivalent behind a $50-200\,\mathrm{cm}$ thick concrete shielding wall, due to $3\,\mathrm{GeV}$ electron losses on a 2-mm vacuum chamber.

To estimate doses in forward direction, we recommend to generally use dedicated simulations with accurate geometry instead of formulas, since the actual dose values in this case are very sensitive to small deviations in source parameters, observation location and averaging, and because a large fraction of the energy is deposited inside the shielding wall, which becomes a significant second source of radiation.

References

[1] . F. Tavares et al., *Commissioning and first-year operational results of the MAX IV 3 GeV ring*, J. Synchrotron Rad. 25, 1291-1316 (2018)

[2] H. Dinter, J. Pang, K. Tesch, *Calculations of Doses due to Electron-Photon Stray Radiation from a High Energy Electron Beam behind Lateral Shielding*, Radiat. Prot. Dosim. 25, 107 (1988)

[3] K. Tesch, *Shielding against High Energy Neutrons from Electron Accelerators – A Review*, Radiat. Prot. Dosim. 22 No.1, 27-32 (1988)

[4] K. Tesch, *Data for Simple Estimates of Shielding against Neutrons at Electron Accelerators*, Part. Accel. 9, 201-206 (1979)

[5] M. Sakano et al., *Calculations of Dose Equivalents due to Stray Radiation from a High Energy Electron Beam in a Forward Direction*, Radiat. Prot. Dosim. 37 No.3, 165-173 (1991)

[6] A. Fasso et al., *Shielding against electrons*, Landolt Börnstein – Group 1, Vol. 11, 309 (1990)

[7] G. Battistoni, S. MurWiklaczaro, P.R. Sala, F. Cerutti, A. Ferrari, S. Roesler, A. Fassò, J. Ranft, *The FLUKA Code: Description and Benchmarking*, Proc. of Hadronic Shower Simulation Workshop 2006, Fermilab 6-8 September 2006, M. Albrow, R. Raja eds., AIP conference Proceeding 896, 31-49 (2007)

[8] A. Fasso, A. Ferrari, J. Ranft, P.R. Sala, *FLUKA: A Multi-Particle Transport Code*, CERN-2005-10 (2005), INFN/TC_05/11, SLAC-R-773

[9] National Council on Radiation Protection and Measurements, *Radiation protection for particle accelerator facilities.*, NCRP Report No. 144, 2003

[10] H. Dinter et al., NIM-A 455 (2000) 460-469.

[11] W.P. Swanson, Health Phys. 37 (1979) 347.

Radiation safety issues at SwissFEL

L. Pedrazzi, Dr. E. Hohmann, A. Karcher

Paul Scherrer Institute
October-2019

Abstract

The Swiss Free Electron Laser (SwissFEL) is a new large-scale facility currently under commissioning at the Paul Scherrer Institute (PSI). The two beamlines, ARAMIS and ATHOS are in the commissioning phase respectively ATHOS in the construction phase.

Accessible areas surrounding the accelerator tunnel together with the pulsed time structure of the primary beam, lead to new challenges to ensure that the radiation level in these areas remains in compliance with legal constraints defined by the Swiss radiation protection ordinance.

1 Introduction of SwissFEL

The project SwissFEL was approved in 2012 and the first light from the ARAMIS Beamline was seen on December 5, 2016. The experimental program started in 2017. In 2020, the second beamline ATHOS will be expected to operate.

SwissFEL is a building, which is located at the Eastern side of the PSI boundary. It is integrated in a regional recreational area, surrounded by a jogging path and various biotopes (Fig. 1). The facility is more than $720\,\mathrm{m}$ long and divided into four parts, the Injector section, Linac section, Undulator section and experimental areas.

The planned electron energy of the accelerator is $7\,\mathrm{GeV}$ with a charge per pulse of $800\,\mathrm{pC}$ and a repetition rate of $100\,\mathrm{Hz}$. The two beamlines, ARAMIS and ATHOS, are operated with two micro bunches and three spectrometer beam dumps. Additionally, the facility use important diagnostic elements in front of the beam.

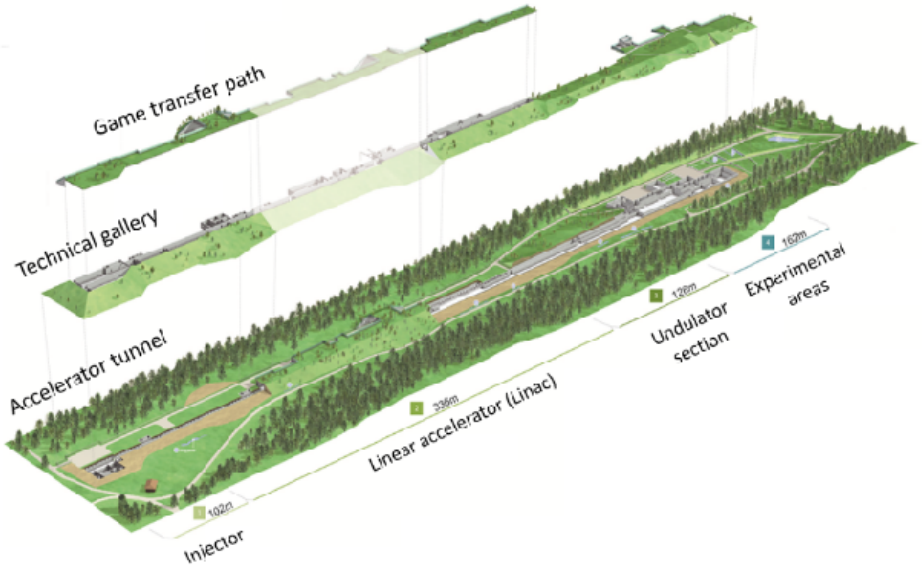

Figure 1: *Overview of the SwissFEL building in the recreational area, surrounded by a jogging path, game transfer paths, various biotopes and a BBQ station on the beginning of the facility.*

2 Radiation safety issues

Since the facility is in a recreational area with game transfer paths, various biotopes and public areas, an effective dose guidance value of $1\,\mathrm{mSv/y}$ must apply. Furthermore, it is not allowed to install detectors or other devices in the public area, so the dose rate must be measured inside the tunnel. With a calibration factor, the dose rate in the controlled and public area will be calculate.

Figure 2: *The facility with the public area.*

To determine the calibration factor, the complex structure of the building with all technical shafts or ducts, shielding penetrations, stairs and reduction in the shielding was dimensioned in an early stage of the project. It ensures the compliance with guidance values for nominal full beam losses for less than a few seconds.

3 Safety systems

The facility has two safety systems for radiation protection, the personnel safety system (PSYS) for the safety system inside the beam tunnel and the dose rate protection system (DRPS) for the safety outside the tunnel.

- PSYS: ensures no beam transport is possible while the protected area is accessible.
- DRPS: raises alarms (online monitoring) and switch off the beam when the dose rate approaches the guidance values imposed on the ambient equivalent dose in the accessible areas close to the beam tunnel.

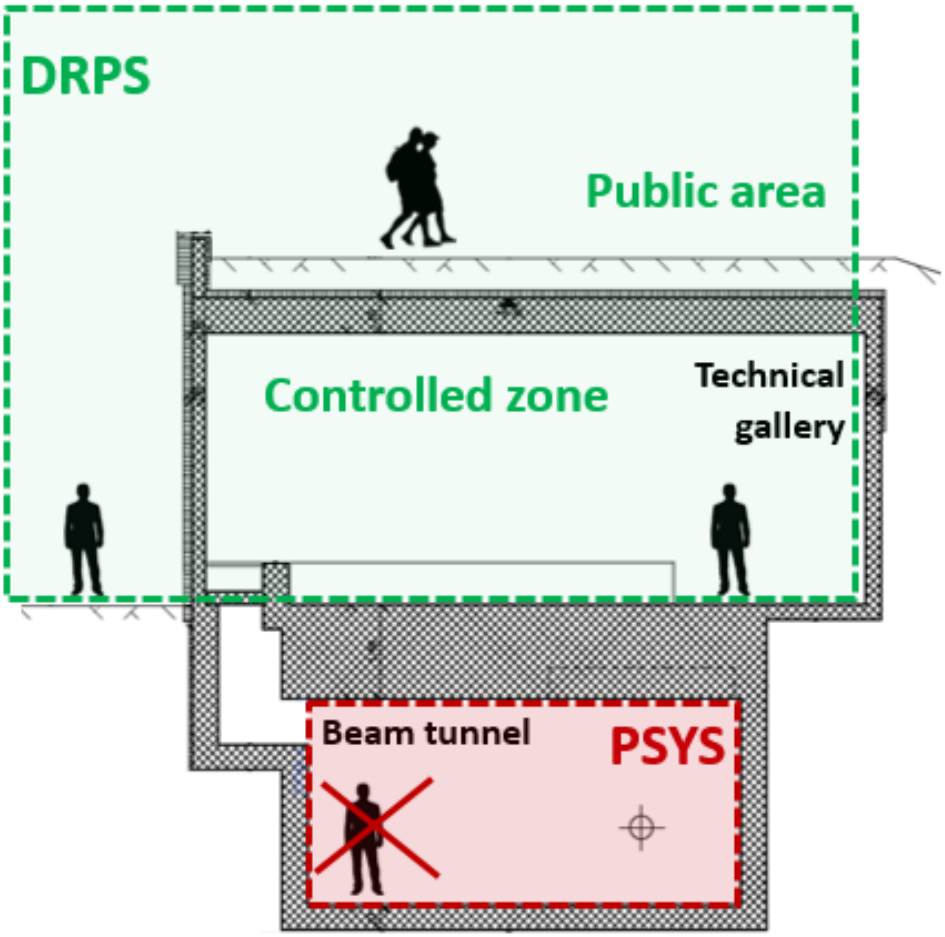

Figure 3: *The safety system DRPS and PSYS for the safety inside and outside the tunnel.*

For the measurement of the neutron dose inside the beam tunnel, the DRPS employs neutron rem counters LUPIN 5401 BF^3 – NP (ELSE Nuclear) adapted for pulsed mixed fields (linearity up to $7.5\,\mu Sv/pulse$) according to the environment as present at SwissFEL [1].

4 Dose monitoring: Basic concept

The SwissFEL uses the safety system DRPS in order to ensure that the dose rate in the surrounding accessible areas of the facility is in compliance with the guidance values by the Swiss protection regulations [2]. The structure of the DRPS can be divide in three independent subsystems. The detectors are using Ethernet PLC-based protocols to the DAQ, which is surveys the correct function of the detectors by checking various parameters. Additionally, the dose values are compared to the calculated alarm thresholds using different algorithms. The third system is the archive and visualization, which archives in intervals of 1 second the mean dose rate and the parameters (threshold, calibration factors and detector information).

5 Calibration factor and shielding classes

The calibration factor is derived for all shielding classes (SC) using analytical or Monte Carlo methods. The facility use six shielding classes:

- SC0: normal tunnel ceiling
- SC1: reduced tunnel ceiling
- SC2: lateral shielding wall
- SC3: shafts and ducts
- SC4: special cases (stairs, elevator)
- SC5: RF-feedthroughs

These factors are verified by dedicated measurements done while causing intentional beam losses near the positions of interest.

6 Verification

The goal of the measurements is to verify the DRPS in terms of model assumptions and calibrations factors. Therefor a maximal loss has to be intentionally produced at the investigated position, which has to be representative for other positions. Neutron and gamma radiation measurements are performed in accessible areas around the investigated position. These measurement's campaigns allows to compare dose rates with different beam parameters and to generate specific scenarios.

7 Measurement setup

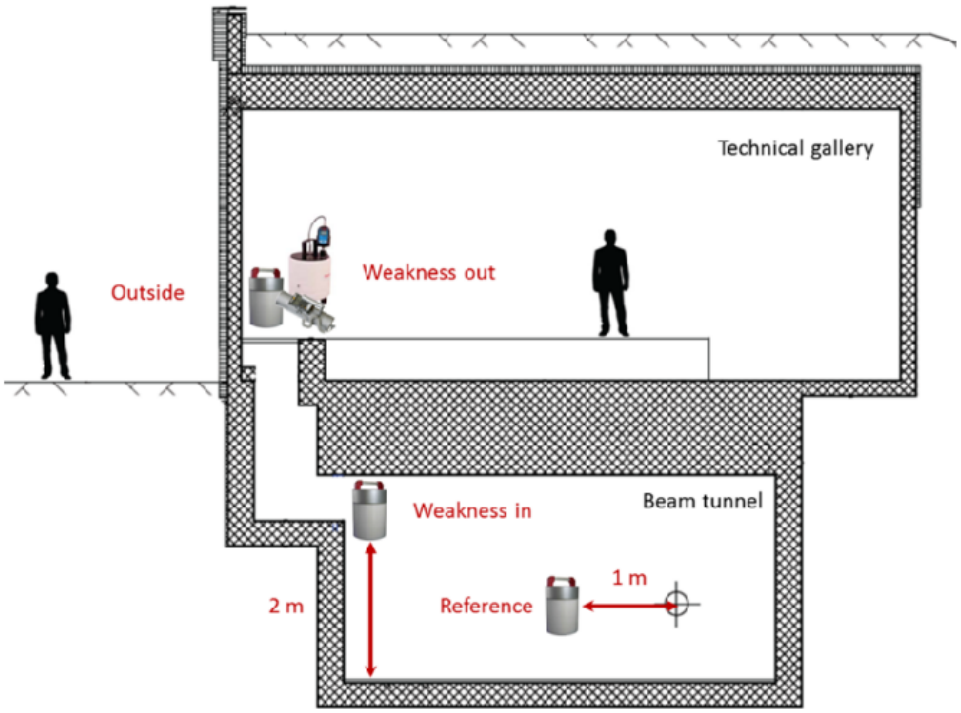

Figure 4: *Measurement set up during an intentionally produced beam loss near the investigated position.*

For the dose rate outside the beam tunnel, neutron and photon detectors are used. The calibration factor is the neutron dose rate outside ($DR_{n,out}$) divided by the neutron dose rate inside ($DR_{n,in}$) the beam tunnel:

$$CF_{SC} = \frac{DR_{n,out}}{DR_{n,in}} \tag{1}$$

The measured and the calculated values are then compared.

8 Results

Figure 5 shows an example of a measurement campaign with a comparison of measurements and Monte Carlo simulations. In this example, the investigated position is a shielding class SC3 with “reduced” shielding i.e. with penetrations (in this case an airshaft). During this campaign following measurements were performed:

1. Neutron dose rate inside the tunnel at a reference point to monitor the beam loss;
2. Neutron dose rate at the weak position inside the tunnel;
3. Neutron and gamma dose rate outside the tunnel.

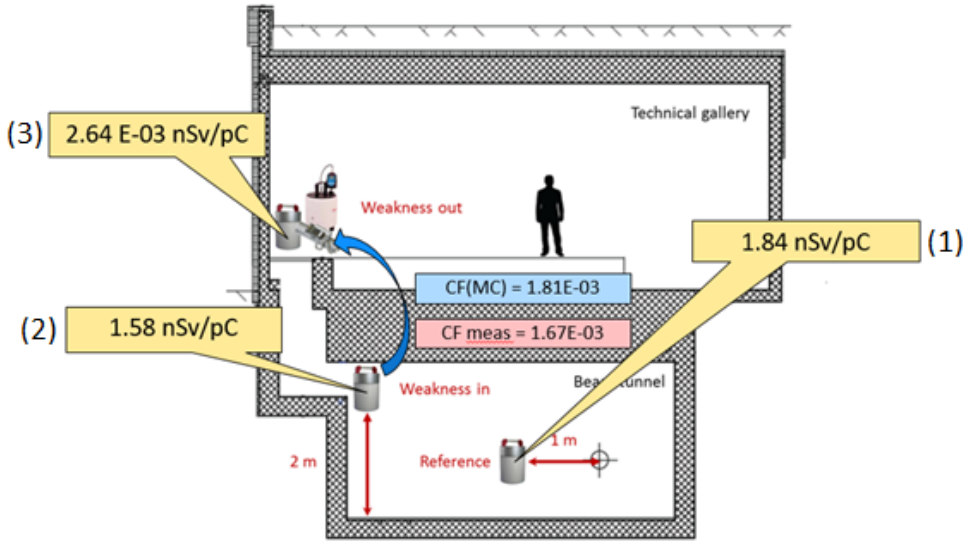

Figure 5: *example of a measurement campaign with results*

The calibration factors calculated the Monte Carlo simulations (CF(MC)) and measured (CF meas) are shown in figure 5 too. In this case, the measurements confirms the simulated calibration factor.

9 Conclusions and outlook

SwissFEL is a new facility with a complex shielding structure, which is currently under commissioning. Two safety systems - DRPS and PSYS - ensure radiation safety for the public and employees:

- PSYS – concept is comparable to other facilities and well-established system at PSI
- DRPS – new approach, setup and method
  - Verification measurements have confirmed assumptions (ongoing).
  - Employed survey instruments are able of operating in the SwissFEL environment.

References

[1] Manessi, Diacomo Paolo & Cassell, Christopher & Ferrarini, Michele & Hohmann, Eike & Mayer, Sabine & Silari, Marco & Varoli, Vincenzo. (2014). A new version of the LUPIN detector: Improvements and latest experimental verification. Review of Scientific Instruments. 85.065102. 101063/1.4879936.

[2] Radiological Protection Ordinance 2018

Beamline shielding design and safety protection at TPS

J.C. Liu, A.Y. Chen, P.J. Wen

National Synchrotron Radiation Research Center, Hsinchu, 30076, Taiwan
October 2019

Abstract

Beamline shielding at Taiwan Photon Source (TPS) is designed to protect against intensive bremsstrahlung and synchrotron radiation in a separate manner. With space constrain inside the hutch and cost of shielding taken into consideration, different calculation approaches and shielding arrangements are adopted to effectively attenuate these two intrinsically different radiation sources. This paper illustrates the shielding design at TPS that is aimed to provide a safe research environment outside the beamline hutches. Other safety concerns at TPS beamlines, such as oxygen deficiency and ozone production, are also addressed.

1 Introduction

Taiwan Photon Source (TPS) is a $3\,\mathrm{GeV}$ synchrotron light source designed to operate at $500\,\mathrm{mA}$ with top up mode that provides stable and consistent synchrotron to users for various disciplines of research experiments. The 24 fold double bend achromat lattice is able to provide 24 straight sections for insertion device with 48 beam ports available for beamlines in total. Currently, we have 7 Phase I beamlines operational for users and another 10 phase II beamlines under commissioning or installation in 2019.

The goal of TPS beamline shielding is to protect users at the vicinity of beamline will not receive radiation dose higher than $1\,\mathrm{mSv}$ in a year assuming $2000\,\mathrm{hours}$ of beam time annually [1]. The derived dose rate limit on the surface of TPS beamline shielding hutch is $0.5\,\mu\mathrm{Sv/h}$ taking the contribution of bremsstrahlung and synchrotron into consideration. The strategy of beamline shielding at TPS is to deploy collimator made of heavy metal at proper location to contain the primary bremsstrahlung with minimum divergent angle, and to terminate the bremsstrahlung with a stopper as early as possible. For optical components intercepting sufficient amount of bremsstrahlung power, secondary bremsstrahlung shielding will be required to attenuate the scattering bremsstrahlung. The hutch shielding at TPS is designed to attenuate synchrotron radiation only without any credit against scattering bremsstrahlung. This will significantly reduce the cost of shielding hutch without jeopardizing radiation protection.

2 Radiation Sources

Two intrinsically different radiation sources are encountered in the shielding design for synchrotron beamlines, they are high energy bremsstrahlung and extremely intense synchrotron with much lower energy compared with bremsstrahlung. Due to the variation of interaction properties between photons and materials at different energy ranges, the requirements of shielding thickness against bremsstrahlung and synchrotron are quite different either in the beam axis or in the lateral direction. If shielding design has to consider both radiation sources, the shielding thickness of beamline hutch will be dominated by the bremsstrahlung and its cost will be inevitably high.

Gas bremsstrahlung (GB) originating from the interaction of circulating electrons with residual gas molecules in the accelerator orbit is forward peaked with a characteristic emission angle $1/\gamma$ which is $0.167\,\mathrm{mrad}$ for

TPS operated at 3 GeV. The energy spectra of GB from TPS straight section of 13 meters in length and gas pressure at 1 nTorr was simulated by FLUKA [2] Monte-Carlo code as shown in Fig.1. The GB spectrum is inversely proportional to the photon energy and its maximum energy can reach to the electron energy. The average GB energy at TPS is a few MeV that we adopt attenuation factor of shielding at Compton minimum for conservative consideration.

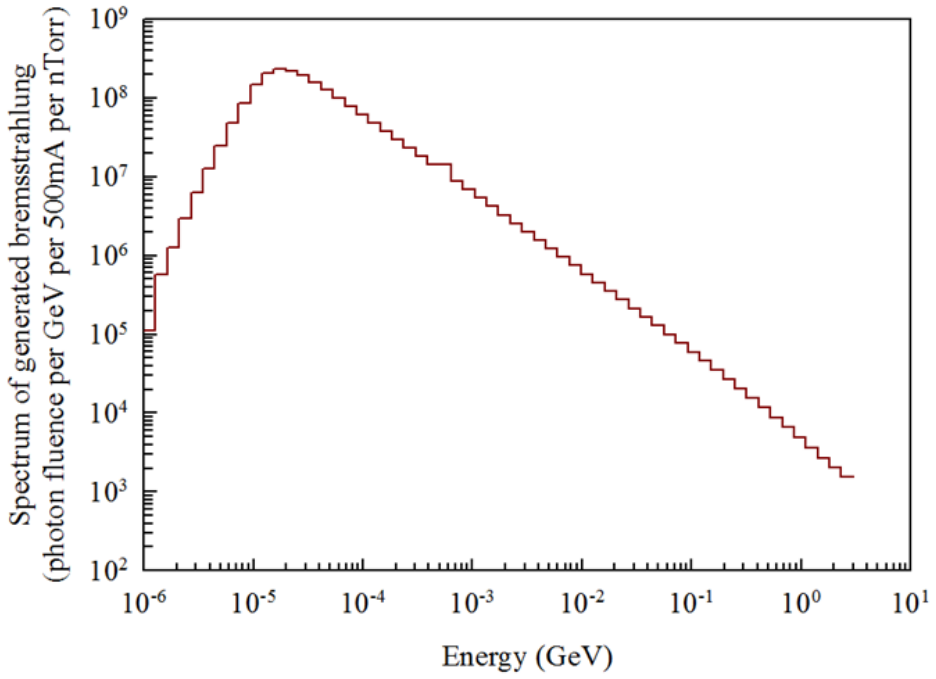

Figure 1: *Energy spectra of gas bremsstrahlung from 13m straight section at TPS.*

Synchrotron is the useful photon beam guided into beamline for user application, unfortunately synchrotron and GB share the same trajectory that shielding must consider high energy photon contribution before optical element can deflect synchrotron with sufficient offset to effectively differentiate these two radiation sources. The energy spectra of synchrotron from TPS in-vacuum undulator IU22 at different operational gap are calculated by STAC8 [3,4] program and illustrated in Fig.2. The majority of TPS phase I and II beamlines utilize undulator as the synchrotron source and the critical energy of these synchrotron spectrum is lower than 7 keV which is the critical energy of bending magnet beamline.

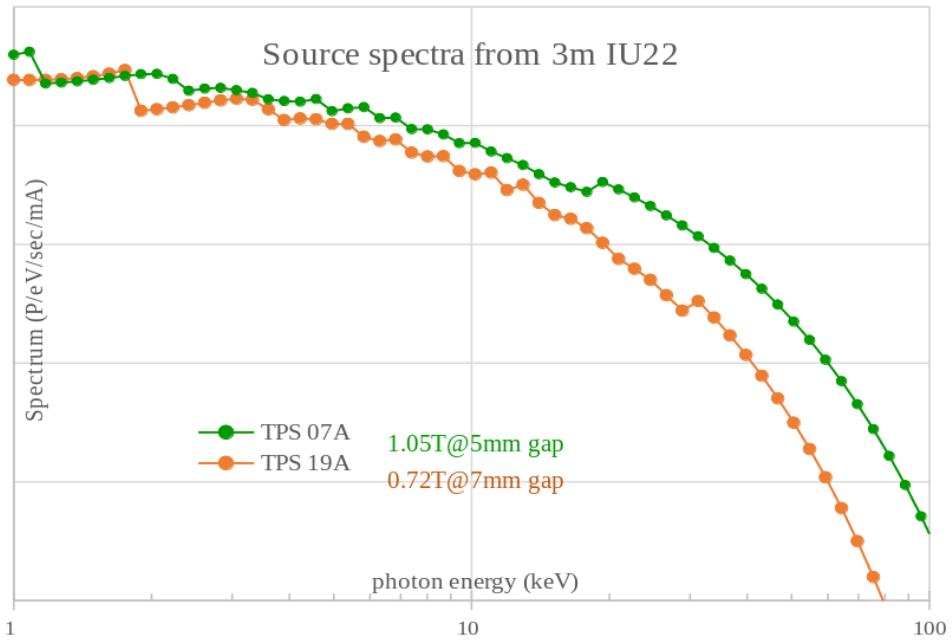

Figure 2: *Synchrotron source spectra from In-vacuum Undulator IU22 at TPS, orange circles denote synchrotron from TPS 19A beamline using IU22 with magnetic strength of* $0.72\,\mathrm{T}$ *when gap is operated at* $7\,\mathrm{mm}$ *and green circles denote TPS 07A source spectrum from IU22 at* $1.05\,\mathrm{T}$ *with §5mm gap.*

The dose rates of primary GB and synchrotron are listed in Table 1 where synchrotron dose rate is calculate by STAC8 code and GB dose rate is approximated by the following equation [5]:

$$D_{GB}(Sv/h) = 2.5 \times 10^{-27} \left(\frac{E}{0.511}\right)^{2.67} \frac{I \times L}{d(d+L)} \tag{1}$$

where E is the electron energy in MeV, I is the beam current in e/s (TPS at $500\,\mathrm{mA}$), L is the effective length of the air path in meter, d is the distance from dose point to the end of the air path, and the vacuum pressure is normalized to 10-9 torr. It is a rule of thumb at TPS that any shielding against primary GB requires tungsten of $22\,\mathrm{cm}$ or lead of $30\,\mathrm{cm}$ to effectively attenuate the GB dose rate below $0.5\,\mu\mathrm{Sv/h}$.

Table 1: *Dose rate for gas bremsstrahlung and Synchrotron at TPS beamlines.*

Gas bremsstrahlung	Long straight	Standard straight	Bending
Length of air path (m)	18.8	13.0	6.1
Distance from dose point to air path (m)	13.1	13.5	13.4
Bremsstrahlung dose rate at 1 nTorr (Sv/h)	4.06	3.28	2.13
Dose rate behind $20\,\mathrm{cm}$ W stopper ($\mu\mathrm{Sv/h}$)	0.68	0.54	0.35
Synchrotron	IU22 (3m) × 2	IU22 (3m) (1.05T)	Dipole (1.19T)
Synchrotron dose rate (Sv/h)	1.32×10^9	6.62×10^8	6.9×10^6

3 Shielding design

TPS bremsstrahlung ray tracing and shielding design starts from the defining of model source size in the electron orbit as shown in Fig.3. The source point is located at the entrance of bending magnet where electron trajectory starts to curve, rather than the actual source point for insertion device is at the end of undulator or wiggler. To simplify the shielding design against GB, the source size of TPS beamline is a rectangular plane perpendicular to the beam orbit, although the actual vacuum chamber is elliptical. The source size for insertion device beamline is $30\,\mathrm{mm}$ vertically and $68\,\mathrm{mm}$ horizontally which is the actual dimension of TPS electron orbit, for bending magnet beamline we add a secondary GB source size with 66mm in the horizontal direction toward accelerator center to accommodate the intrusion section of vacuum antechamber inside the dipole.

The first bremsstrahlung shielding as shown in Fig. 4, from right to left, is a front-end lead collimator with $20\,\mathrm{cm}$ of thickness locating as close to the electron orbit as possible to augment the shielding ability of ratchet wall normal to the bremsstrahlung direction. The size of this collimator should be sufficient to intercept the bremsstrahlung originated from any source point in the straight section upstream. A tungsten heavy-metal shutter (HMS) with $22\,\mathrm{cm}$ of thickness is followed before the 1.2 meter concrete ratchet wall and the dimension of HMS should be large enough to intercept possible scattering radiation from the electron orbit in any possible angle. HMS is a critical safety device for radiation safety which bridges the front-end interlock and beamline interlock [6].

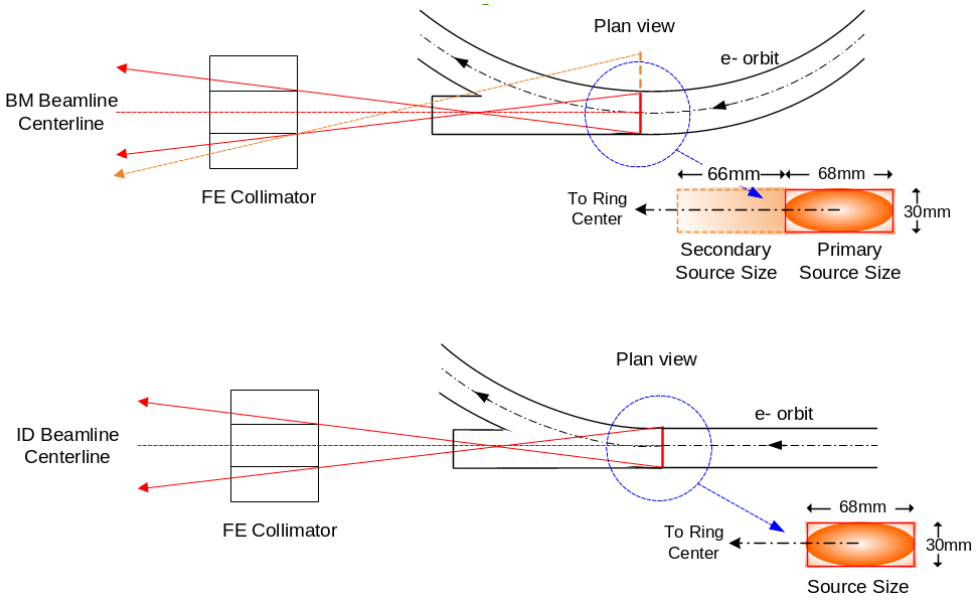

Figure 3: *TPS Bremsstrahlung source size.*

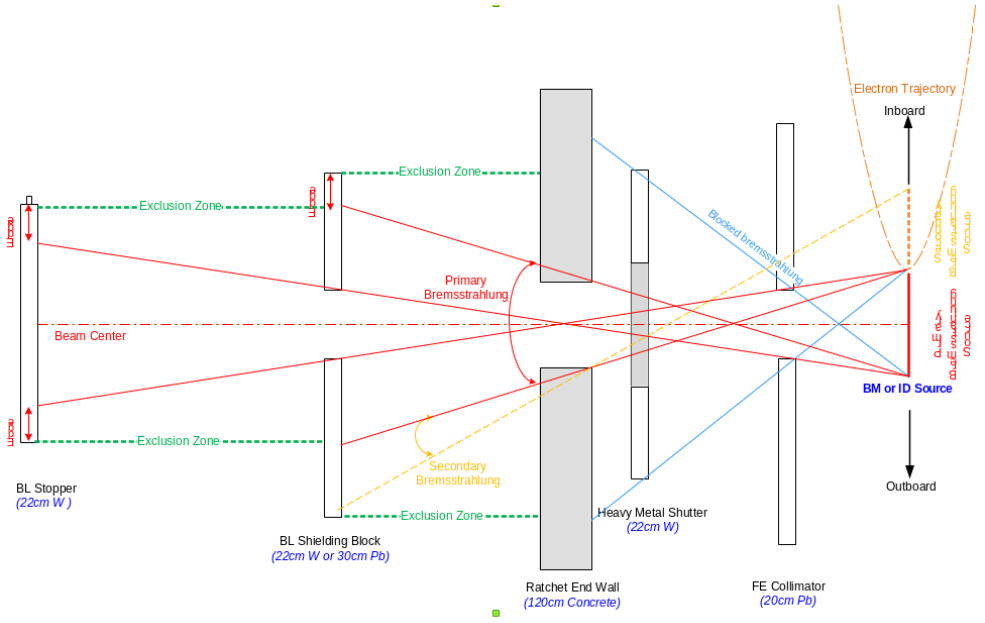

Figure 4: *TPS Bremsstrahlung ray tracing and shielding design.*

For beamline bremsstrahlung shielding as shown in Fig. 4, ray tracing of two extreme boundary lines were drawn from the edges of primary bremsstrahlung source through the near edges of shielding wall with respect to the source. The area inside these two extreme lines is where primary bremsstrahlung may theoretically exist and we use 30 cm of lead or 22 cm of tungsten against primary GB in the beam direction at TPS. At Taiwan Light Source (TLS), a 1.5GeV synchrotron accelerator operated at 360mA, we installed exclusion zone to prevent access into primary GB area if hutch is not required. Due to the complicated optics design in the TPS beamlines, several separated sets of collimators are arranged in sequence to narrow the divergence of GB angle which will significantly reduce the dimension of the stopper after which the bremsstrahlung is fully terminated.

Neutron production from primary GB interacting with optical elements is possible [7] especially those components intercepting significant portion of bremsstrahlung power, e.g. the mask, slits or DCM in the upstream of a beamline. Polyethylene of 10 cm in thickness is required at TPS to surrounding the heavy metal collimators and the stopper to attenuate neutron as shown in Fig.5.

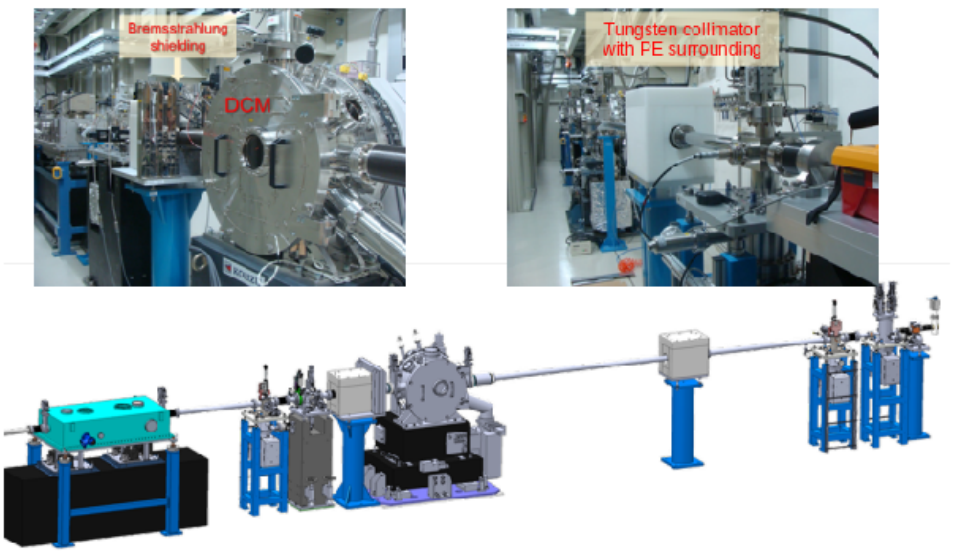

Figure 5: *Bremsstrahlung shielding design in TPS beamline.*

4 Safety conerns

Shielding hutch can turn into a potential confined space and pose hazard of oxygen deficiency when liquid nitrogen is used for purge or cooling optical devices for a long period of operational time without proper ventilation, especially in case of accidental leakage of significant amount of liquid nitrogen. To ensure safe oxygen concentration inside the hutch, oxygen detectors are installed in TPS hutches to provide audio alarm to warn users from entering the hutch.

Ozone production is a safety concern when intense synchrotron, especially white light, passing through air path in a beamline due to radiolysis process [8]. TPS 02A is a bending magnet beamline for micro-tomography experiment using white light, and there is a long air path in the end-station hutch for accommodating biological sample. Users complain about unusual odor when they entered the hutch that leads us to suspect possible production of ozone when white light cause oxygen molecules to decompose then to form ozone. We have measured the ozone concentration by placing detector on top of the air path of TPS 02A hutch with different distances and the results are shown in Fig. 6. This measurement was performed on February 13^{th} and 15^{th} of 2019 when TPS was operated at storage current of $500\,\mathrm{mA}$ and the exposure time was 300 seconds with hutch ventilation turned off.

The maximum ozone concentration at TPS 02A hutch can reach more than 100 ppm when detector was placed less than $15\,\mathrm{cm}$ from the beam center. It is clear that a steady state or saturated ozone concentration may exist for each detector location. As soon as the photon beam was shut off, the concentration of ozone rapidly decrease to several ppm within 60 seconds and continue to decrease.

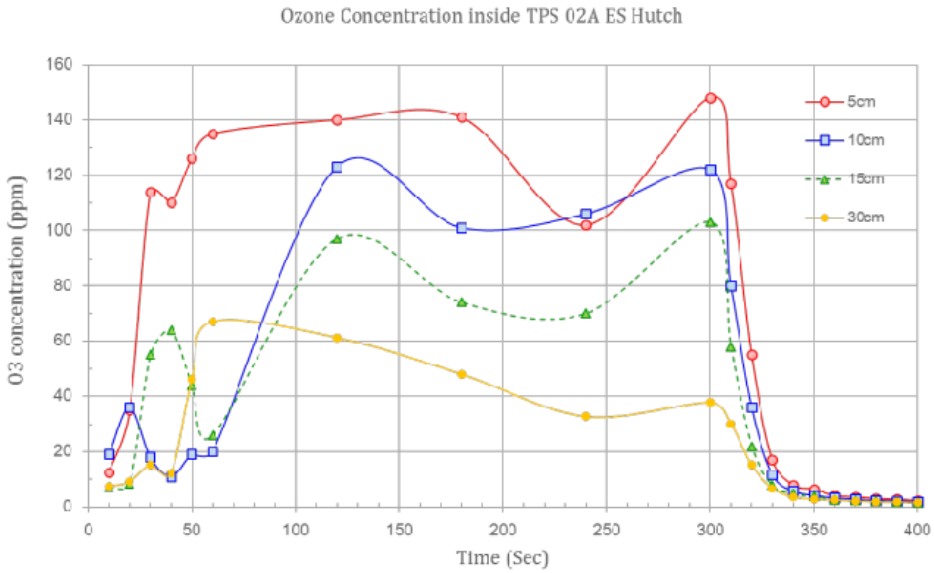

Figure 6: *Ozone measurements at TPS 02A beamline.*

5 Conclusions

Radiation sources from accelerator, both bremsstrahlung and synchrotron, are intensive and pose severe threat, however, the useful beam into experimental station is relative small in term of beam power. Minimize beam power as small as possible and terminate bremsstrahlung as early as possible, such as using slits in the front end or mask in the optics hutch, will reduce radiation burden on the bremsstrahlung shielding and significantly eliminate scattering bremsstrahlung into hutch walls. Hutch shielding design for synchrotron scattering is feasible if bremsstrahlung is well contained. Ozone is an issue when white beam is present, ventilation and detection is advised.

References

[1] R.J. Sheu, J. Liu, C.R. Chen, F.D. Chang, K.S. Kao, M.S. Chang, J.P. Wang, *Taiwan Photon Source (TPS) Radiation Safety Analysis Report*, Technical Report NSRRC-TR00073 (2009).

[2] A. Fasso, A. Ferrari, J. Ranft, P.R. Sala, FLUKA, *A multi-particle transport code*, CERN-2005-10, INFN/TC_05/11, SLAC-R-773 (2005).

[3] Y. Asano and N. Sasamoto, *Development of Shielding Design Code for Synchrotron Radiation Beamline*, Radiat. Phys. & Chem. 44 133-137 (1994)

[4] Y. Asano, *A Study on radiation shielding and safety analysis for a synchrotron radiation beamline*, Japan Atomic Energy Research Institute, Ibaraki, Japan, JAERI-Research 2001-006 (2001).

[5] N.E. Ipe, A. Fasso, *Gas Bremsstrahlung Consideration in the Shielding Design of the Advanced Photon Source Synchrotron Radiation Beamlines*, Nucl. Instr. Meth. A, p.534-544 (1994).

[6] J.C. Liu, et.al, *Design Guidelines of TPS Beamline Radiation Safety Interlock System*, Technical Report NSRRC-TR00199 (2013)

[7] A.Y. Chen and J.C. Liu, *The radiation dose measurement for the coherent X-ray scattering beamline in TPS*, Proceedings of the 9th International Workshop on Radiation Safety at Synchrotron Radiation Sources, Hsin-Chu, Taiwan, pp.175-181 (2017/4/19 2017/4/21)

[8] J. T. Sears and J. W. Sutherland, *Radiolytic formation and decomposition of ozone*, Phys. Chem., 72 (4), pp 1166–1171 (1968)

Radiation Protection Issues of BESSY VSR

K. Ott, Y. Bergmann, A. Bundels, H. Huck, L. Pichl

Helmholtz-Zentrum Berlin, BESSYII, 12489 Berlin, Germany
October-2019

Abstract

Depending on the experiment, the focus of the users of synchrotron light sources is on different parameters. Some experiments require high flux X-rays while the pulse length is of no concern. On the other hand a large and growing fraction of BESSY's user community focuses on functional materials where dynamics on the picosecond and sub picosecond range are essential. To fulfill both requirements BESSY plans a major upgrade to provide high-flux and picosecond-pulse beams simultaneously [1,2]. The unique feature of the BESSY Variable pulse-length Storage Ring (BESSY VSR) will be the simultaneous operation of long ($15\,\mathrm{ps}$ rms) and short ($1.7\,\mathrm{ps}$ rms) pulses. This approach is complementary to the concept of Diffraction Limited Storage Rings (DLSR). DLSRs reduce the emittance by two orders of magnitude, but require to lengthen the bunches up to the 100 ps range to reach acceptable life times.
The impact this project has on the overall radiation safety at BESSY is discussed. The major aspect is that the number of electrons injected into the storage ring per year will not be increased, thus keeping the annual radiation level through the shielding walls the same. We present the way this number will be controlled by our top-up interlock. The inclusion of super conducting cavities in the storage ring will require additional safety measures, because of possible field emissions whose radiation level we calculated with FLUKA [3,4]. Finally, we present FLUKA calculations for the shielding design of a new facility to test the super conducting cavities of the VSR modules.

1 Introduction

There are two fundamental prerequisites for experiments conducted at synchrotron light sources: For those who require small emittance and for those who require short pulses for time resolved picoseconds experiments or as a source of coherent synchrotron radiation (CSR) for THz experiments. For the latter type of experiments BESSY offers dedicated low α shift operation during three weeks per year. The bunch length is reduced by the low α operation from $15\,\mathrm{ps}$ to $3\,\mathrm{ps}$. There are two low - α operation modes with the maximum current of $100\,\mathrm{mA}$ (bursting mode: high power fluctuating CSR) and of $15\,\mathrm{mA}$ (stable mode). BESSY VSR is a solution to fulfill both types of requirements. The idea is to have $15\,\mathrm{ps}$ and $1.5\,\mathrm{ps}$ bunches simultaneously in the ring and up to hundred times more current in the short bunches in comparison with the low α mode thus increasing the THz power by four orders of magnitude.

Many existing SR facilities in the 2^{nd} decade of operation are aiming for an upgrade as diffraction limited storage thus improving the emittance, brilliance and spatial coherence. The need for a new multi-bend achromat lattice requires a new magnet system, a new vacuum system due to smaller apertures, sometimes a new injection or even the reduction of the number of sections. This is a global upgrade which requires one to two years of dark time of the SR facility.

BESSY VSR will conserve brilliance for all users and add short intense pulse operation at all beam lines in parallel. The shaping of the longitudinal phase space is possible by additional cavities in storage ring and booster. This local upgrade does not require an additional dark time to the usual summer shut down.

2 Top-up operation of BESSY

During the former decay mode it was possible to hold the $1\,\mathrm{mSv/a}$ limit in the accessible parts of the experimental hall at BESSY. Non-accessible parts are hutches at beamlines of superconducting insertion devices or the areas close to the front-ends at beamlines of dipoles or normal undulators without hutches. The top-up interlock is based on two pillars: 1) To keep the number of injected electrons/year on the same level as it was during the decay mode (same annual dose for radiation through the walls) 2) To avoid high dose rates by crash conditions during the injections (in Germany the dose rate limit for accessible areas is $3\,\mathrm{mSv/h}$).

We have summarized the electron losses for the two modes in table 1. The injected and successfully stored charge for the top-up mode is 3.2 times higher than it is for the decay mode. This has to be compensated by increasing the injection efficiency from $30\,\%$ to $90\,\%$ for the top-up mode to inject about the same number of electrons into the storage ring per year. Otherwise the annual dose through the walls would rise by the same factor. The top-up injection scheme ($0.5\,\mathrm{mA}$ every $30\,\mathrm{sec}$) corresponds to a life time of $5\,\mathrm{h}$.

Table 1: *Overview of BESSY annual electron losses [5]*

	Decay mode	Decay mode	Top-Up mode	Top-Up mode
Operation time	250 days/a	6000 h/a	250 days/a	6000 h/a
Injections	3 day	750/a	2880/day	720000/a
Current added in SR	150 mA/injection	112.5 A/a	0.5 mA/injection	360 A/a
Charge		9.0×10^{-5} C/A		2.88×10^{-4} C/a
Efficiency		30 %		90 %
Electrons	5.62×10^{14} e^-/a	$\mathbf{1.9 \times 10^{15}}$ $\mathbf{e^-}$**/a**	1.80×10^{15} e^-/a	$\mathbf{2.0 \times 10^{15}}$ $\mathbf{e^-}$**/a**

Because the number of injected electrons per year is about the same for the two modes, the doses through the shielding walls will be the same for the top-up mode as it was for the decay mode.

Not to predict is the annual dose around the front-ends because this depends on the loss scenarios of the electrons in the straight sections and there relative frequency of occurrence. We considered three scenarios with the highest probability: 1) Loss at a thin target in the straight section (e.g. dipole chamber or taper), 2) Loss at an undulator chamber with a small angle, 3) Loss at the vacuum system down-stream of the first dipole.

We calculated the resulting annual doses of these scenarios with FLUKA [3, 4] at the fence of the interlock saved exclusion areas for all injected electrons divided by 16, the number of sections at BESSY. The result is given in table 2:

Table 2: *Annual doses at the fence of the exclusion areas around the front-ends [5]*

Scenario	Gamma dose (average of range)	Neutron dose (average of range)	Sum
Thin target	$6.6\,\mathrm{mSv/a}$	$7.3\,\mathrm{mSv/a}$	$13.9\,\mathrm{mSv/a}$
Undulator Chamber	$0.66\,\mathrm{mSv/a}$	$1.6\,\mathrm{mSv/a}$	$2.26\,\mathrm{mSv/a}$
Downstream dipole	$0.066\,\mathrm{mSv/a}$	$0.16\,\mathrm{mSv/a}$	$0.226\,\mathrm{mSv/a}$

The average of the three scenarios results in an annual dose of $5.46\,\mathrm{mSv/a}$ for $6000\,\mathrm{h/a}$ or $1.82\,\mathrm{mSv/a}$ for $2000\,\mathrm{h/a}$. During the test operation the experimental hall is therefore radiologically controlled area and the

users and employees working there are considered as radiation workers category B who are allowed to get up to 6 mSv/a during work. It has been verified by measurements during the test operating phase that the $1\,\mathrm{mSv}$ limit is hold also around the front-ends in the accessible part of the experimental hall.

Because of the considerable errors of measurement due to the pulsed radiation structure and the high energy radiation, we control the top-up operation by the control of the number of injected electrons. The injection efficiency eq. (1) is measured for every injection shot,

$$\eta = \frac{2.5 \cdot \Delta I_{SR} \cdot 100\%}{I_{SY}} \tag{1}$$

An average of $90\,\%$ should be reached in a $4\,\mathrm{h}$ time period. $\eta < 60\,\%$ stops top-up operation immediately. At $4\,\mathrm{h}$ average η value $<90\,\%$ switches to the decay mode for a penalty time. The duration is calculated using eq(2):

$$\Delta t = 4h\frac{90\% - \eta}{100\% - 90\%} \tag{2}$$

In the following list the top-up conditions (and their reasons) are summarized:

1. Linac charge $\leq 2\,\mathrm{nC/shot}$ (limits dose rate to the values of the former microtron)
2. Booster charge $>0.1\,\mathrm{nC/shot}$ corresponds to $0.3\,\mathrm{mA}$ (measurement accuracy)
3. Max. injection rate $0.1\,\mathrm{Hz}$ (decay mode $10\,\mathrm{Hz}$, reduces max dose rate by factor 100)
4. Top-up only if I $>200\,\mathrm{mA}$ multi bunch (avoid severe error conditions)
5. Injection efficiency $90\,\%$ in $4\,\mathrm{h}$ average (annual dose)
6. Min. life time e.g. $5\,\mathrm{h}$ at $300\,\mathrm{mA}$ eq.(3) (annual dose)
7. Injection eff. $<60\,\%$ stops next shot (stop top-up if one shot failes, avoid severe error conditions)
8. Interlock saved exclusion areas (bremsstrahlung, beam dumps, injections)

3 Ambient dose measurement at BESSY, an overview

Measurements of radiation doses of accelerators can imply considerable systematical and stochastical errors. Neutron measurements that are conducted by the common Anderson-Brown or Leake type monitors cannot measure high energy neutrons (E $>10\,\mathrm{MeV}$) due to the fact that the detection occurs within a counting tube by nuclear reactions of thermalized neutrons. After passing some concrete shielding the neutron spectra at accelerators have beside the giant resonance maximum at $1\,\mathrm{MeV}$ a second broad maximum at about $100\,\mathrm{MeV}$. We solved this problem by the calculations of high energy correction factors [6] and by developing an additional moderator that extents the measurement range from $10\,\mathrm{MeV}$ to several GeV [6, 7].

The usage of the counting tubes of the neutron monitors as proportional counters can lead to dead time effects which can cause considerable errors too. The injection pulses are shorter than the dead-times and the time between the injection shots is much longer then the dead-time, so only a small number of neutrons can be detected during each injection shot [9]. We develop correction formulas that are valid even in the saturation range [9] and improved our neutron monitors by the replacement of the preamplifiers by those of a shorter dead-time [6].

Because of their functionality ionisation chambers have much less detection losses due to pulsed radiation than proportional counters. The comparative small recombination losses are neglectable in gamma radiation fields that are possible in the accessible parts of synchrotron light sources. High energy gamma radiation that is beyond the high energy limit of $7\,\mathrm{MeV}$ has to be considered though. We calculated correction factors for high

energy gamma radiation for different directions and shielding and found values between 2.6 (transversal) and 17 (forward) [10].

Stochastic beam dumps can also contribute to the dose in the experimental hall. We selected a position by FLUKA calculations where the dose by such dump is highest at the fence of the exclusion area close to the front-end. (In forward direction the dose is higher but is shielded by a combination of lead and PE). We use a cylindrical PE phantom (diameter 20 cm) with an Albedo-dosimeter mounted on the surface. This passive dosimeter has the advantage that it can detect short high intense pulsed gamma and neutron doses. These type of Albedo-dosimeters are also used for personal dosimetry at BESSY and as such are also evaluated by the authorities. We also calculated correction factors for the high energy neutrons for them (the results are presented at this workshop [8]).

In 2018 the in-vacuum undulator CPMU17 has been included into the storage ring. Also under these new circumstances the top up conditions can be hold.

With our improved measurement system and methods we can prove that we hold the $1\,\mathrm{mSv/a}$ limit in the accessible part of the experimental hall. We will therefore approve to end the test operating phase we introduced at the start of the top up operation and which we continued during operation tests of the in-vacuum undulator.

4 Radiation protection aspects of the upgrade to VSR

Short bunches will in principal reduce the life time because the electron density in the bunches is higher and therefore the Touschek loss rate. (The Touschek loss rate is proportional to the electron density in the bunch). The consequence is a higher amount of injected electrons per year resulting in a higher annual dose. A VSR bunch pattern is foreseen with reduced current in the short bunches thereby lengthening the overall life time to the actual top-up conditions. The intended bunch pattern is shown in fig. 1.

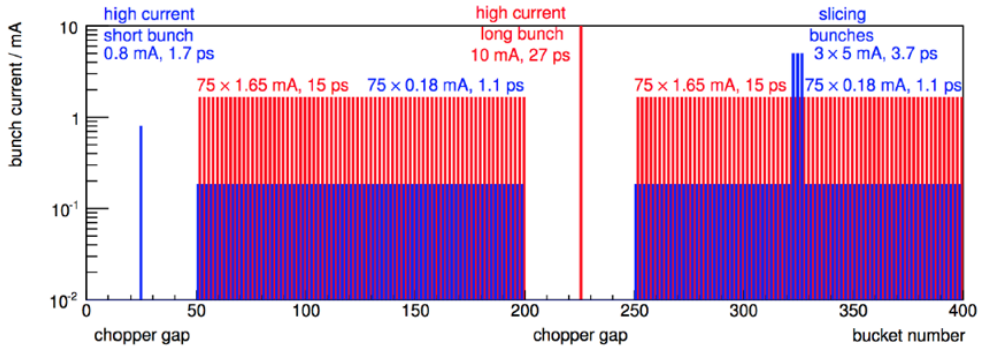

Figure 1: *Bunch pattern VSR: Blue short bunches* 1.1 ps*, red: long bunches* 15 ps

Besides the alternating long (red) and short (blue) bunches there are foreseen three high current short slicing bunches and a high current camshaft bunch. The bunch pattern preserves the BESSYII emittance (5nm rad) and the top-up capabilities (injection efficiency $>90\,\%$ with a lifetime $>5\,\mathrm{h}$).

BESSY VSR will be installed in two steps: During the so called preparation phase only the two $1.5\,\mathrm{GHz}$ cavities will be included in the VSR module. With this configuration only a bunch pattern is possible where all buckets are filled by short bunches. Also in this mode it is possible to comply with the top-up conditions. The acceptable life time τ for the top-up interlock depends on the ring current:

$$\tau = -t/\frac{I(t)}{I_0} \qquad \text{with } I(30s) - I_0 = 0.5mA \tag{3}$$

For e.g. I_0 = 300 mA, t = 30 s and $I(t)$=299.5 mA (current top-up conditions) it follows from eq.(3) that τ= $|5|$ h. If all buckets are filled with short bunches we get from fig. 1 the current of $54\,\mathrm{mA}$ or $69\,\mathrm{mA}$ if we add the slicing bunches. For this current using the same calculation τ= $1.15\,\mathrm{h}$ and it is acceptable for the top-up conditions.

Preliminary experiments show that this is possible to accomplish. Because of using only two cavities (instead of four) the bunch length will be approximately $2.5\,\mathrm{ps}$ which lengthen the life time by a factor of two.

The bunch length in the booster is larger than the length of the short bunches in the storage ring. Therefore the injection efficiency is reduced and again this requires more injected electrons resulting in a higher annual dose. Therefore two additional normal conducting PETRA cavities as shown in fig. (2) are foreseen for the synchrotron to reduce the length of the synchrotron bunches to increase the injection efficiency.

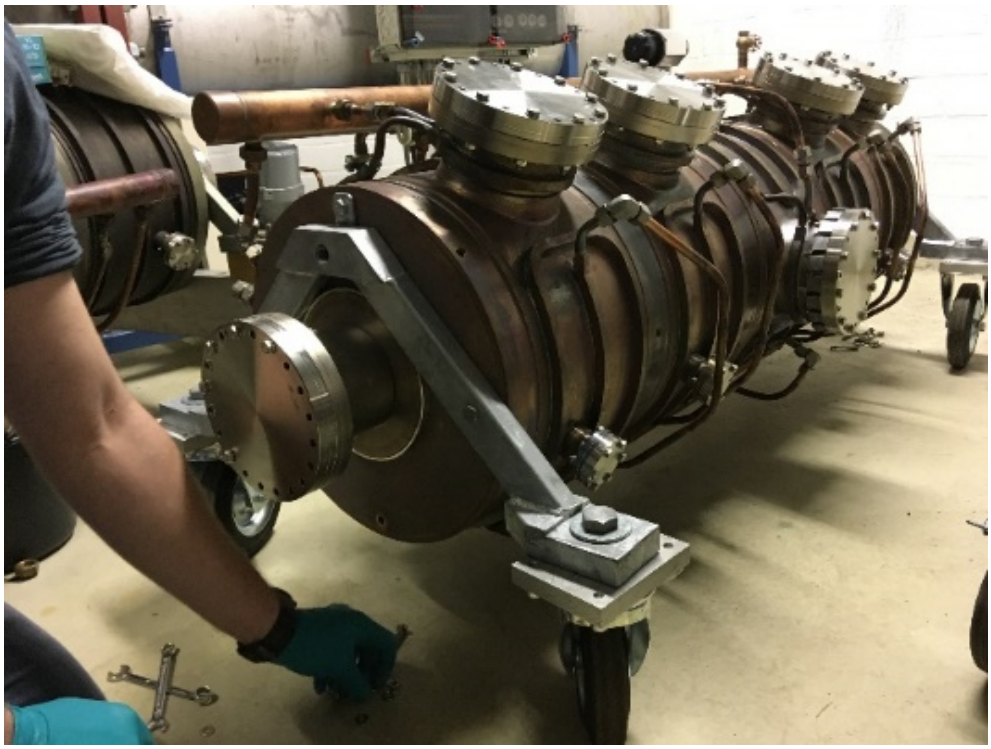

Figure 2: *Two PETRA cavities on their way to the synchrotron tunnel (summer 2019)*

BESSY VSR requires the inclusion of four (in the prep phase two) additional superconducting cavities in the storage ring in one straight section.

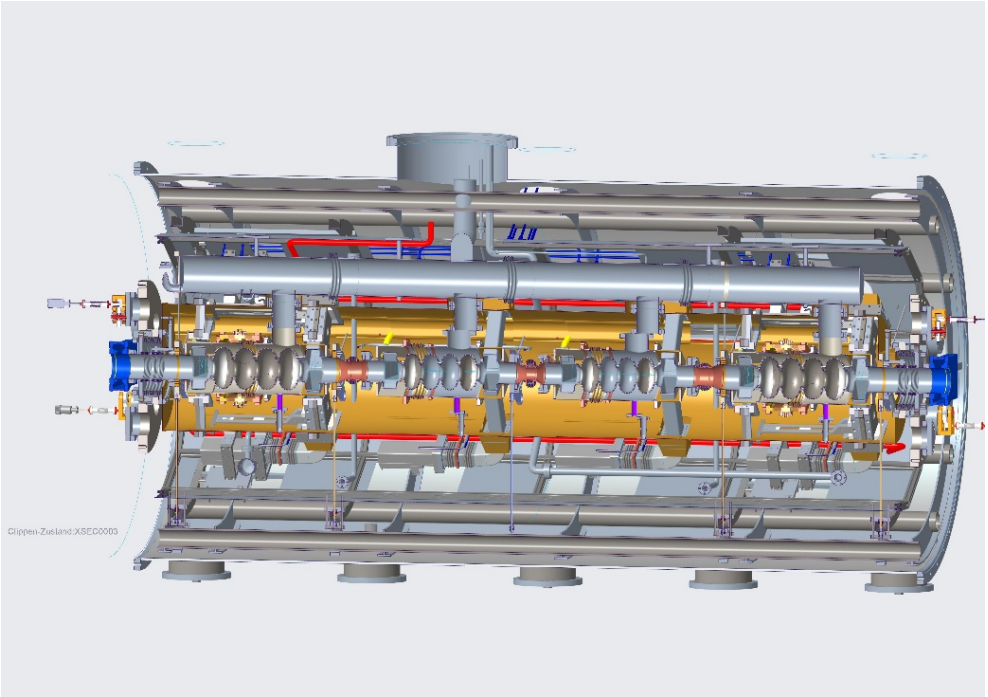

Figure 3: *VSR module with two* 1.5 GHz *and two* 1.7 GHz *superconducting cavities with the cryomodule*

The superconducting 7 T multipole wiggler was located in this section has already been removed.

Field emission up to the Sv/h range is possible, so the need of additional local shielding has been investigated. The design of this local shielding has been accomplished by FLUKA calculations.

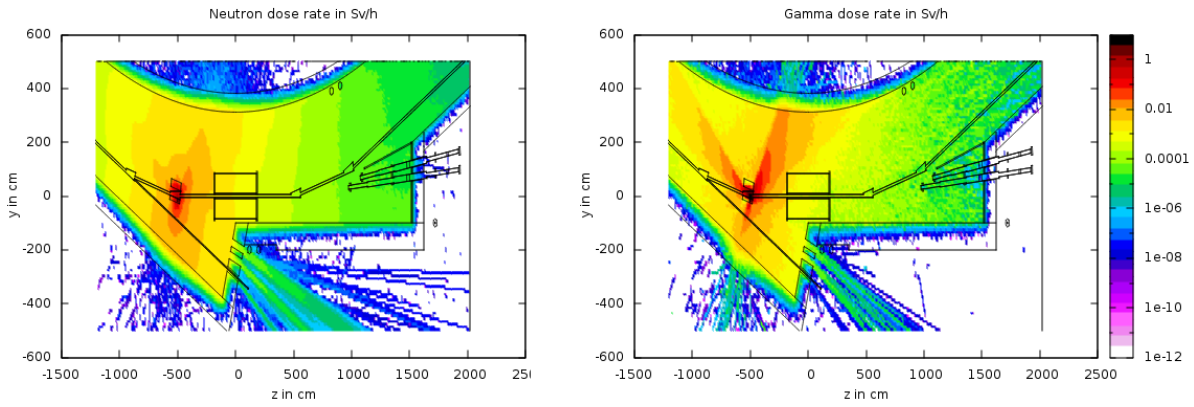

Figure 4: *FLUKA simulation of upstream field emission of VSR cavities:Max. dose rates in Sv/h left neutrons, right gammas.*

In fig.4 the maxumim dose rate by upstream field emission of the superconducting cavities is shown. Based on former measurements of field emission we used 0.25 μA and 80 MeV as worst case parameter. The dipole field is 1.3 T, the dipole (C magnet yoke 30 cm Fe) will be locally shielded by 15 cm of lead. The area close to the front ends in the experimental hall is an interlock saved exclusion area. Even for this worst case assumptions the radiation safety could be reached by the combination of accelerator and local shielding combined with exclusion areas.

Field emission downstream is less dangerous because the field emission beam is deflected to the inner wall of the storage ring tunnel and the distance to the down stream front end is larger. The down stream dipole will also

be local shielded the same way to compensate the reduced inner wall thickness and to absorb the backscattered radiation from the yoke.

The supply of the new cavities requires additional openings and ducts in the shielding walls and therefore the design of media labyrinths. The largest of these labyrinths is located on the roof of the storage ring. It will contain the cryo and rf supply of the VSR module with its superconducting cavities. It is shown in fig. 5.

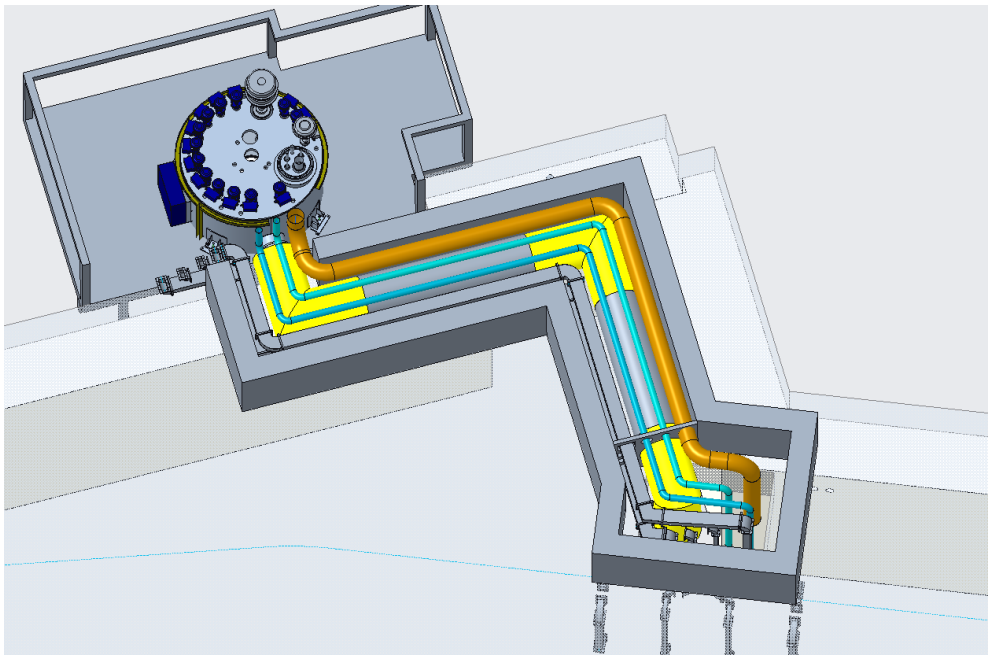

Figure 5: *Media labyrinth for rf and cryo supply of VSR cavities:*

At BESSY the roof of the storage ring tunnel is accessible during operation and injections. The shielding effect of the labyrinth is therefore the same as the general shielding of the roof in this area. The labyrinth design has been conducted using FLUKA.

To assemble and to test the VSR modules the construction of the testing hall 2 has been started. In the cellar of this building a bunker is under construction for rf and cryo tests of these modules.

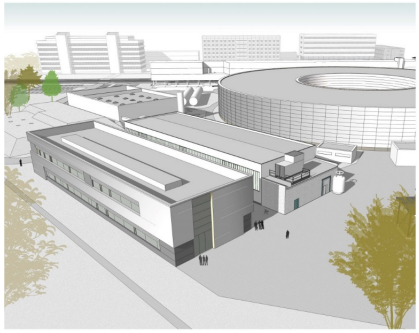

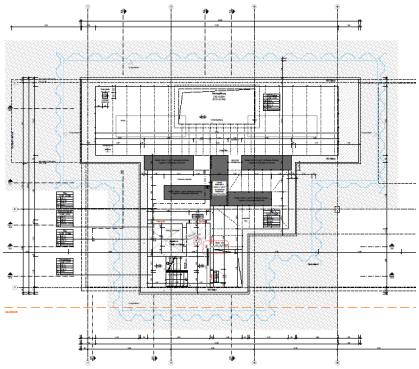

Figure 6: *Testing hall 2 and bunker (cellar) to test VSR modules:*

The bunker will have in part a removable roof to transport the accelerator components to be installed there by a crane. Besides the labyrinth for persons it will have a second one for media e.g. rf and cryo supply. The cellar will be an interlocked saved exclusion area during operation. The interlock will also require that the elevator cabin is opened and fixed at the basement level during operation.

5 Summary

ESSY VSR is an upgrade program that enables time resolved ps X-ray experiments and CSR for THz experiments. In comparison with the low-α mode the THz power is increased by four orders of magnitude. VSR will have in the storage ring a sequence of long ($15\,\mathrm{ps}$) and short ($1.5\,\mathrm{ps}$) bunches. To reduce Touschek losses the current in the short bunches will be reduced. Four super conducting cavities ($1.5\,\mathrm{GHz}$ and $1.7\,\mathrm{GHz}$) will be included in one straight section of the storage ring. VSR will be accomplished in two steps. In the preparation phase only two $1.5\,\mathrm{GHz}$ cavities will be installed. Their usage will allow to operate the ring with short bunches only during e.g. several short pulse weeks per year.

The established top-up conditions with the control of injection efficiency and life time (among others) will also be used for VSR operation.

Radiation from field emission has been investigated by FLUKA calculation. The dipoles up- and downstream of the VSR section have to be local shielded. The combination of accelerator and local shielding and interlock saved exclusion areas in the experimental hall is sufficient to hold the annual dose limit- in the accessible parts.

The labyrinth on the roof of the storage ring tunnel for rf and media supply has been designed by FLUKA calculations. The labyrinth will have the same shielding effect as the roof. The roof is accessible during operation.

To avoid a reduction of injection efficiency the booster bunch length will be reduced by two additional PETRA cavities.

Construction of testing hall 2 has been started. Testing hall 2 includes a subterraneous bunker to test the VSR cavities.

An overview was given about the improvements of the measurement system and methods at BESSY. The ability to measure pulsed and high energy radiation avoids considerable measurement errors and makes it possible to prove that the dose limit of $1\,\mathrm{mSv/a}$ is hold in the accessible parts of the experimental hall. The in-vacuum undulator has been successfully commissioned. This will allow to approve the end of the test operation and return to regular operation thus transforming the radiologically controlled area in the experimental hall to a surveillance area.

VSR requires new operating licences for the booster and later for the complete facility. The established top-up conditions will allow to keep the surveillance area also for this new operation mode.

References

[1] A. Jankowiak et al, *The BESSY VSR Project for Short X-Ray Pulse Production*, Proceedings IPAC (2016)

[2] A. Jankowiak, J. Knobloch et al., *Technical Design Study BESSY VSR* , Helmholtz-Zentrum Berlin, 2015, http://dx.doi.org/10.5442/R0001

[3] G. Battistoni, S. Muraro, P.R. Sala, F. Cerutti, A. Ferrari, S. Roesler, A. Fasso, J. Ranft, *The FLUKA Code: Description and Benchmarking*, Proc. of Hadronic Shower Simulation Workshop 2006, Fermilab 6-8 September 2006, M. Albrow, R. Raja eds., AIP conference Proceeding 896, 31-49 (2007)

[4] A. Fasso, A. Ferrari, J. Ranft, P.R. Sala, *FLUKA: A Multi-Particle Transport Code*, CERN-2005-10 (2005),INFN/TC_05/11,SLAC-R-773

[5] K. Ott, *Radiation Protection Issues of the Top-Up Operation of BESSY*, Proceedings RADSYNCH (2013)

[6] K. Ott, Y. Bergmann, M. Martin, L. Pichl, *Measurement Errors and Upgrades of the Ambient Dose Measurement System at BESSY*, Proceedings RADSYNCH (2017)

[7] M. Caresana, M. Helmecke, J. Kubanak, G.P. Manessi, K. Ott, R. Scherpelz, M. Silari, *Instrument Intercomparison in the High Energy Mixed Field at the CERN-EU Reference Field (CERF) Facility*, Rad. Prot. Dos. 161, 67-72 (2014)

[8] A. Bundels, K. Ott, *Calculation of High Energy Neutron Corrections for Albedo Dosimeters at BESSY*, this conference

[9] K. Ott, M. Helmecke, M. Luszik-Bhadra, M. Martin, A. Weber, i͡Dead Time Effects of Neutron Detectors due to Pulsed Radiation, Rad. Prot. Dosi. Doi:10.1093/rpd/ncs326 (2012)

[10] K. Ott, Y. Bergmann, *FLUKA Calculations of Gamma Spectra at BESSY*, Proceedings IPAC (2014)

SLS 2.0: Safety Challenges of the upgrade of the Swiss Light Source

L. Pedrazzi and M. Keller and D. Mohr, S. Mayer

Department of Radiation Safety and Security, Paul Scherrer Institute, 5232 Villigen PSI, Switzerland
October 2019

Abstract

The Swiss Synchrotron Light Source (SLS) at PSI is a third-generation light source that has been in operation since 2001. With an electron energy of 2.4 GeV, it provides photon beams of high brightness for research in materials science, biology, and chemistry.

The facility will be undergoing a major upgrade in 2023-2024 (SLS2.0) to increase the overall brightness. The upgrade will consist of replacement of the entire storage ring (288 m circumference) and potential changes to the concrete shielding.

An overview of the SLS 2.0 project and the main associated radiation safety challenges are discussed.

1 Introduction to PSI

The facilities at PSI cover a broad range of research areas: from materials research and energy research to nanotechnology and biology.

On the Western side of the river Aare, there are three large research facilities: the SLS, the Neutron Spallation Source (SINQ) and the Muon Source. The Center for Proton Therapy for the treatment of specific cancers is also located here. Our fourth large research facility, the Swiss Free Electron Laser (SwissFEL), is located in a forested area on the Eastern side; it is currently undergoing commissioning.

PSI runs these facilities not only for its own use, but also for researchers in academia and industry from Switzerland and abroad.

Figure 1: *Bird's eye view of PSI.*

2 Introduction to SLS

Planning for the Swiss Synchrotron Light Source started in 1991. The project was approved in 1997 and the first light from the storage ring was seen on December 15, 2000. The experimental program started in June 2001. As of June 2009, SLS has 18 experimental stations (undulators and bending magnets) and 16 operational beamlines. There are three protein crystallography beam-lines, two of which are partially funded by associations of Swiss pharmaceutical companies including Novartis, Roche, Actelion, Boehringer Ingelheim and Proteros.

The SLS consists of a linac, a booster, and a storage ring. The linac pre-accelerates electrons to an intermediate energy of $100\,\mathrm{MeV}$. The booster accelerates the electrons, coming from the linac, to their final energy of $2.4\,\mathrm{GeV}$. After extraction from the booster, the electrons are injected into the storage ring.

The storage ring is composed of 36 dipole magnets of 1.4 tesla magnetic field strength, 177 quadrupole magnets, 120 sextupole magnets, 73 horizontal and vertical beam steerers, 24 skew quadrupole magnets, and 12 straight sections with undulator magnets that generate ultraviolet and x-ray light.

The storage ring and booster are housed in a concrete tunnel. Two layers of $40\,\mathrm{cm}$ thick concrete blocks cover the tunnel and can be removed to give a crane access to the accelerator components. The linac is located in a separate tunnel.

3 The SLS upgrate project (SLS 2.0)

The goal of the SLS upgrade project is to achieve a smaller emittance resulting in higher brightness. In order to achieve this, the entire storage ring has to be re-built. The upgrade may include modification to the concrete shielding (space problems) and some of the beamlines (Fig. 2).

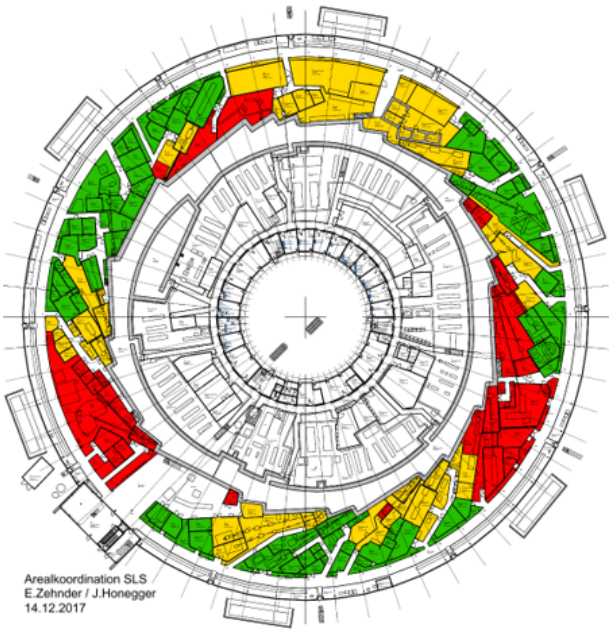

Figure 2: *The SLS upgrade will include modification of the beamlines. In red are the beamlines that have to be completely modified, in yellow partially modified, and in green slightly modified.*

The most important boundary conditions of the project are duration and budget. The dark period is set to 18 months, which is a very big challenge, considering the extent of the necessary modifications. The dark period is projected to start in April 2023 and end in October 2024.

In the current planning state (as of June 2019), there are some problems with the lattice design including various space conflicts and the fact that the brightness appears to be lower than was originally planned. There

are, therefore, discussions about alternate lattice designs with a smaller vacuum chamber and smaller magnets. This should relieve conflicts and eliminate the need to modify the tunnel.

4 SLS2.0 radiation safety challenges

According to the Swiss radiation protection ordinance (RPO) [1], material that could have been activated or contaminated has to undergo a clearance measurement. At SLS, the structures and materials outside the concrete shielding tunnel are neither activated nor contaminated; therefore, no clearance measurements are necessary. However, inside the tunnel, activation cannot be excluded, and all materials, including concrete shielding which will be removed or modified, must be cleared.

The Swiss RPO introduced new clearance requirements coming in force in 2018. For many radionuclides, these limits are significantly lower than before. For example, for Cobalt-60 the new limit is 10 times lower (Fig 3). In order to satisfy the new clearance limits, the clearance measurement times need to be increased and/or the background radiation levels need to be decreased. Because of the time restraints of the upgrade, increasing the clearance measurement times is only possible if the measurements are done independently of the dismantling and outside the SLS building. Background reduction is also problematic because the high intensity proton accelerator, the cyclotron for proton therapy, and the spallation neutron source will continue operating during the dark period.

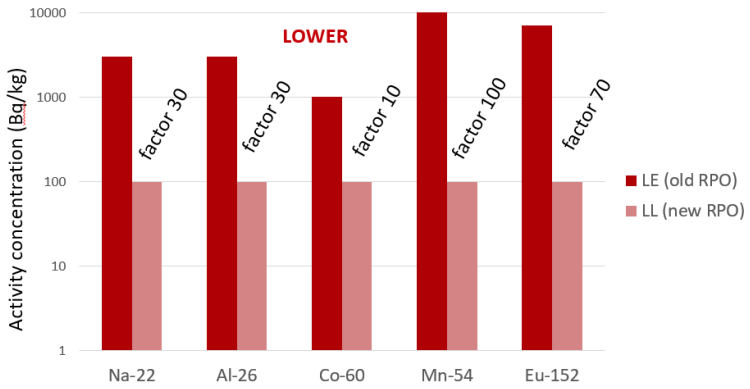

Figure 3: *Comparison of old and new Swiss clearance limits for some radionuclides.*

To address these issues, PSI is building a facility for clearing materials from various upgrade and decommissioning projects. The building should be completed by the summer of 2020. Discussions on the types of measurement equipment to be purchased are ongoing, but total gamma measurements and gamma spectrometry will be necessary. The clearance measurement building is being erected independently of the SLS upgrade, but poses an important precondition for the clearance measurements for the upgrade.

Preparations for the SLS upgrade clearance measurements have already begun. The first step is defining the composition and volume of the waste stream. It is important to distinguish which materials are going to be reused in a supervised area from those that will be disposed, because clearance measurements are not required if the material will be reused. The second step is to determine the nuclide vectors for each material type via measurements (sampling) and simulations. Finally, the most efficient and accurate measurement methods for each type of component and material need to be defined. PSI predicts that a lot of material can be cleared by proving the absence of activation using process knowledge and material history. For the remainder, PSI will establish procedures for dismantling, segregating, and measuring.

Clearance measurements will start with the dark period in April 2023. The first, and most important part, will be the dismantling and separation by component and material type. Because of the short dark period, the dismantling must occur quickly. Thus, the breakdown and separation have to be performed outside the SLS building. A space large enough and protected enough for these activities has yet to be defined. Due to potential dose rate and contamination issues, separation activities cannot occur within the new clearance facility, which

will be reserved solely for measurement activities (dose rate, contamination, and activity concentration).

All clearance measurements have to be reported to the Swiss authorities, who have 10 days to provide feedback. Upon approval from the authorities, materials will be disposed of or stored for decay. By Swiss law, materials can be stored for decay for a maximum of 30 years. If material will not decay to below the clearance levels within this time frame, it is deemed as radioactive waste.

5 Conclusions

SLS 2.0 is a big challenge for PSI. In particular, the short dark period and the relatively low budget will require the radiation safety specialists to be efficient and creative. The main radiation protection challenge will clearing a large quantity of material in a short time period. This requires both completion of the new building for clearance measurements and preparation and execution of a detailed clearance protocol.

References

[1] Swiss Radiological Protection Ordinance of 26 April 2017 (RPO, SR 814.501). Swiss Federal Council (2017).

Radiation Protection Instrumentation of bERLinPro

L. Pichl, Y. Bergmann, A. Bundels, H. Huck, K. Ott

Helmholtz-Zentrum-Berlin, BESSYII, 12489 Berlin, Germany
October-2019

Abstract

The Energy Recovery Linac project bERLinPro is a test facility to study the possible usage of an ERL as synchrotron light source [1]. It is currently under construction and will be operated with the maximum beam parameters of $50\,\mathrm{MeV}$ and $100\,\mathrm{mA}$ cw current. Even though the electron losses within the recirculator are limited to $0.6\,\%$ due to the available rf power supply, (at higher losses an immediate beam break up occurs because of the ERL principle) the beam loss power is by orders of magnitude higher than in electron storage rings used for synchrotron radiation (e.g. the injection beam power of BESSYII is $17\,\mathrm{W}$ during $10\,\mathrm{Hz}$ injections). The Fluka [6,7] calculations of the resulting activation of machine components and air activation have been discussed in earlier papers [3,4].
We present in this work the components of the ambient dosimetry, the measurement system of air activations and their inclusion in the personal safety system. Additionally we present recent calculations of the activation of cooling water and the method of storing and measuring it in case of a leakage.

1 Introduction

In 2011 the Helmholtz-Zentrum Berlin started the design and construction of the **B**erlin **E**nergy **R**ecovery **L**inac **Pro**ject called **bERLinPro** to develop and demonstrate cw superconducting Linac technology and expertise that is required to drive next-generation Energy Recovery Linacs (ERL's). bERLinPro will consist of a SRF photo injector (gun), a merger, superconducting booster and linac modules, the ring and a beam dump ($650\,\mathrm{kW}$ water cooled).

The electrons are accelerated up to $50\,\mathrm{MeV}$, with a maximum current of $100\,\mathrm{mA}$ (cw) and a maximum power loss of $30\,\mathrm{kW}$, limited by the rf-supply in the recirculator.

The low energy parts (gun, booster, merger, dump line and dump incl. its cooling water) of the machine are operated at energies $\leq 6.5\,\mathrm{MeV}$. An activation of these parts is excluded because the necessary threshold energy of nuclear reactions with photons can not be reached.

On the other hand the beam power is much higher, by several orders of magnitude, than in conventional electron storage rings. For bERLinPro it means a permanent injection with $650\,\mathrm{kW}$ (BESSYII: 19 W), a beam power up to $5\,\mathrm{MW}$ in the recirculator and $650\,\mathrm{kW}$ in the beam dump.

The rf power supply in the recirculator ($30\,\mathrm{kW}$) can compensate $0.6\,\%$ ($0.6\,\mathrm{mA}$) losses to avoid an immediate beam break. Even one point source of $0.1\,\mathrm{mA}$ beam current can produce $200\,000\,\mathrm{Sv/h}$ bremsstrahlung in forward direction. In transversal direction this radiation is three orders of magnitude lower. That is why the accelerator hall has been placed subterraneously. The neutron radiation dose rate in transversal direction is about the same as gamma radiation.

2 Ambient Dosimetry

Environmental monitoring is carried out with the aid of six local dose rate measuring stations (Fig.1). The stations are located on the bunker roof above the arcs of the recirculator. They are housed in air-conditioned

measuring cabinets. Each is equipped with an Anderson neutron monitor FHT751 (0.025...10 MeV), supplied with lead moderators (Fig.2) to extend the measurement range up to 1 GeV [8] and an ionization chamber FHT191N for photon measurements (35 keV...7 MeV).

Fig. 1 shows the bunker roof with the six stations, Fig. 2 the interior of a measuring station with the lead moderator (yellow) and the display and alarm unit.

Figure 1: *Measuring stations on the bunker roof*

Figure 2: *Interior view of a measuring station*

The calculated expected annual doses outside the bunker are shown in (Fig.3) [4].

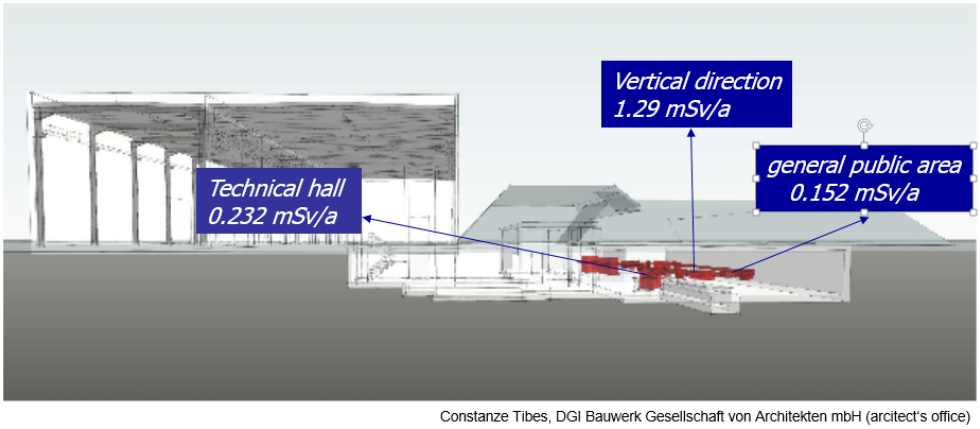

Figure 3: *Calculated annual dose [1]*

3 Air activation, ventilation and dosimetry

During operation the air in the accelerator hall is activated, mainly due to γ-n and n_{th}-γ-reactions. (Table 1).

Table 1: *Activity concentration of main nuclides caused by air activation [4] and legal limits for unrestricted release [9]*

Nucleus	**C**	$\mathbf{T}_{1/2}$	**StrlSchV**
	$\mathrm{Bq/m^3}$	min	$\mathrm{Bq/m^3}$
Be7	2.52×10^2	53.3 d	6.0×10^3
C11	8.29×10^4	20.364	3.0×10^4
N13	2.71×10^5	9.965	2.0×10^4
O15	3.81×10^5	2.037	1.0×10^4
Cl39	4.54×10^3	56.12	6.0×10^3
Ar41	1.99×10^4	109.61	2.0×10^3

In general, the resulting dose for the general public due to γ-submersion must be estimated while taking into account meteorological data, surrounding buildings and atmospheric models, but in our case the calculation is simplified into (Eq. 1) due to the fact that the chimney is at least twice as high as the closest buildings in the neighborhood. (β-submersion, ingestion and inhalation are irrelevant as well in our case.)

$$H_{T,\gamma,r} = A_r \times g_{T,\gamma,r} \times \chi \times f_r \times C_{Geo} \quad [\mathrm{Bq/a},\ \mathrm{Sv\,m^2/Bq/s},\ \mathrm{s/m^2},\ 1,\ 1](Eq.1) \tag{1}$$

$H_{T,\gamma,r}$ - annual dose due to submersion of the nuclide r

A_r - annual activity for the nuclide r

$g_{T,\gamma,r}$ - dose rate coefficent for the nuclide r

χ - dispersion factor for γ-submersion (=1e-2 s/m^2 for 21 m chimney height)

f_r - energy spectrum factor (=1)

C_{Geo} - age factor for grown-ups (=1)

Plugging into (Eq. 1) the annual activity A_r (Table 2) due to the slow exhaust air flow of 2000 hours of operation (at other times the activity is negligible, though it is still monitored) yields a total annual dose of $1.3\,\mu\mathrm{Sv/a}$, well below the legal limit of $50\,\mu\mathrm{Sv/a}$. (In Germany the limit for indirect radiation is $300\,\mu\mathrm{Sv/a}$ [9], but two other emitter in the neighborhood with a total of $250\,\mu\mathrm{Sv/a}$ have to be added.)

Table 2: *Calculated annual discharge rate [4]*

Nucleus	$g_{\gamma,r,T}$	A_r	$H_{\gamma,r,T}$
	(Sv/s) / (Bq/m^2)	Bq/a	Sv/a
C11	3.4×10^{-16}	4.15×10^{10}	1.41×10^{-7}
N13	3.4×10^{-16}	1.36×10^{10}	4.62×10^{-7}
O15	3.4×10^{-16}	1.91×10^{11}	6.50×10^{-7}
Ar41	4.1×10^{-16}	5.99×10^{9}	2.46×10^{-8}
in total			**$1.28\,\mu\mathrm{Sv/a}$**

The activation of the recirculation air is determined by four Xenon-filled proportional counter tubes for activity measurements in gases (Fig.4). The measured activities are accumulated by a data logger (Fig.5).

Figure 4: *counter tube for activity measurements*

Figure 5: *Data logger*

The main fan can only be switched on if it has been released by the activation measurement at the underpressure system and when the bunker gate is open. The air released via the main ventilation is also monitored and logged. In this case we use a large area counter tube (Fig.6 + 6a) for air activity measurements and the logging of the discharge rate.

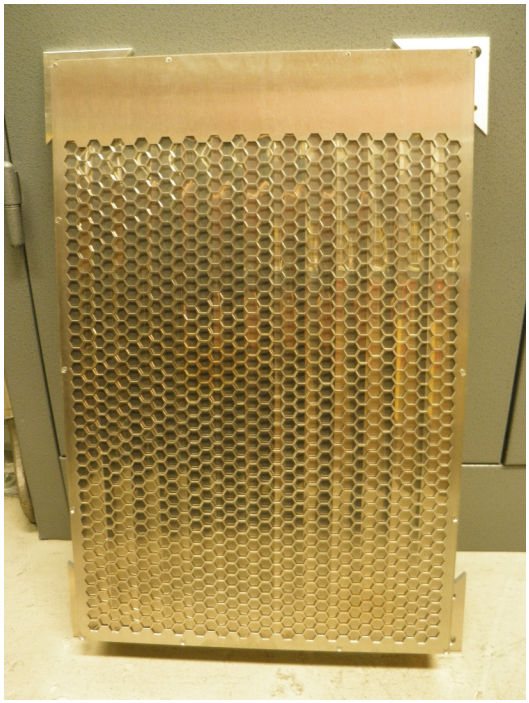

Figure 6: Large area proportional counter for activity measurements

Figure 6a: *mounted on the ventilation ductr*

The radiation protection door, which closes the access to the bunker during operation of the accelerator, is approx. $4.1 \times 3.5 \times 1.3$ m in size. It consists of a steel shell which is filled with heavy concrete and weighs approx. 77 tons. An inflatable seal in the frame of the radiation protection gate seals it airtight against the antechamber (Fig.7).

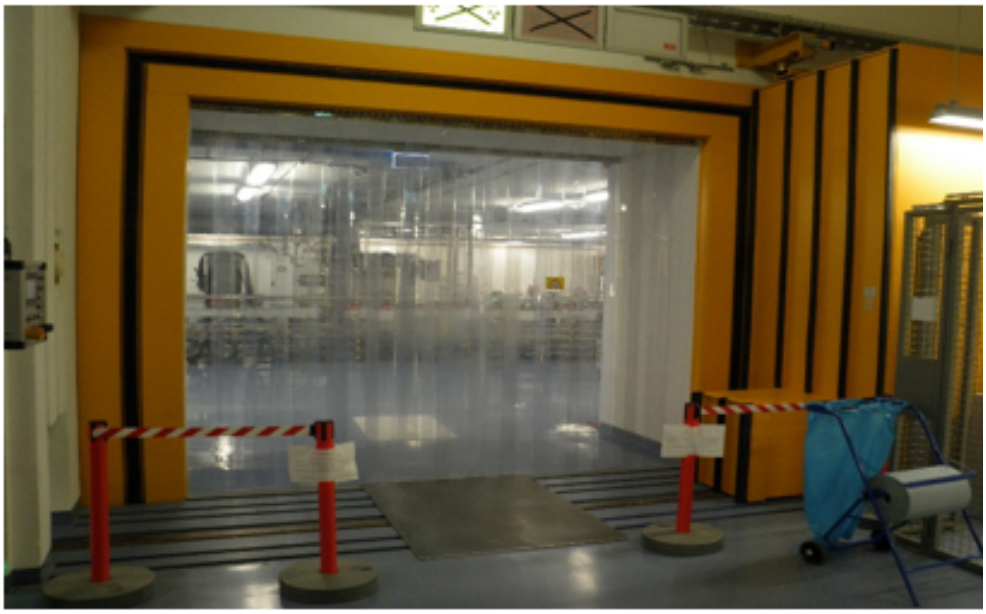

Figure 7: *Radiation protection gate (open) with sealing frame*

Opening the bunker gate and switching the ventilation to the fast ventilation circuit is only possible after the activation values are below the entrance limits. The anticipated waiting time period will be calculated according to the half-lives of the relevant nuclei and displayed in the control system.

4 Cooling water activation and leakage water collection

Even if a very high Bremsstrahlung dose is generated in the forward direction, due to the relatively low energy (6.5 MeV) of the electrons reaching the beam dump, there won't be any activation of machine parts or cooling water in or near the beam dump. The same applies to the other low energy parts (gun, booster and merger, Fig.8) [3]

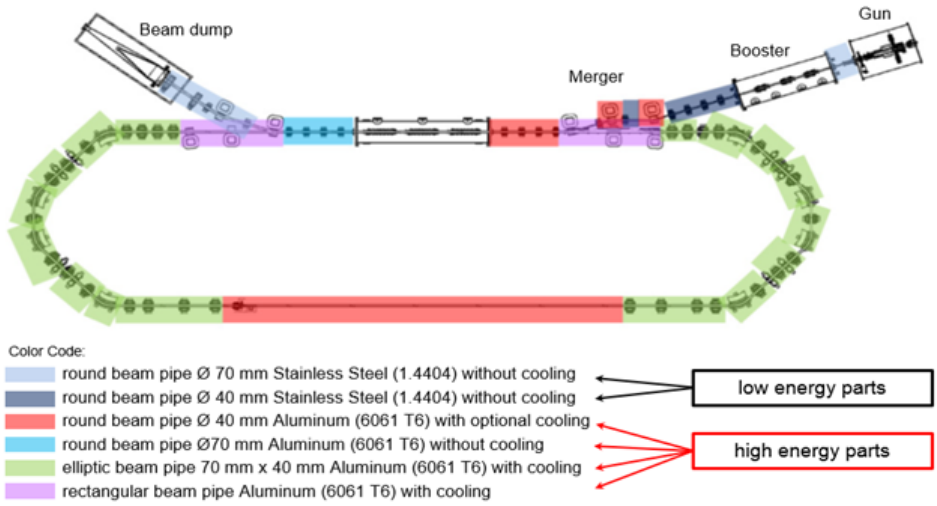

Figure 8: *Materials used for different sections of the vaccum system*

Aluminum was used for the high-energy parts in order to keep the dose due to Bremsstrahlung and thus the activation as low as possible. The situation is different in the recirculator (50 MeV). Fig.9 shows the profile of the vacuum chamber used in the arcs, with cooling ducts on both sides.

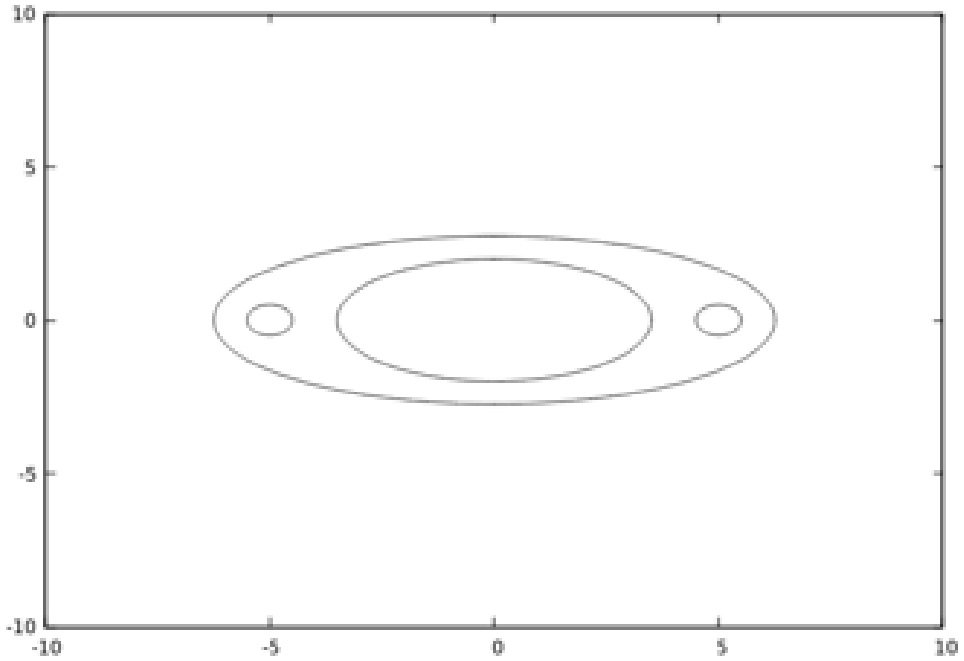

Figure 9: *Geometry of the vacuum chamber (Dimensions in cm)*

The vacuum system consists of an AlMg3 alloy and has a circumference of $58\,\mathrm{m}$. The diameter of the cooling channels is $10\,\mathrm{mm}$. The total cooling water inventory has a volume of $198\,\mathrm{litres}$. To calculate the dose rate caused by the cooling water activation in the pipes, the energy spectrum of the photons and in a second step the activation due to this photon spectrum was calculated using FLUKA [6][7]. A few cm from the pipe, consisting of $2\,\mathrm{mm}$ Cu, the dose rate caused by the generated nuclides is only a few $10\,\mathrm{nSv/h}$, therefore no special safety requirements are necessary along the cooling circuit. Although the total dose rate near the beam pipe will be considerably higher due to activated accelerator components, a determination of the cooling water activation and the resulting possible dose rate is necessary because the heat exchanger is located outside the accelerator hall and any leakage water must be checked before disposal because of the possibility to exceed the activation limits for waste water according to radiation protection ordinance (StrlSchV). The main isotopes created by the cooling water activation are listed in Table 3.

Table 3: *Table 3 - Activity concentration compared to the legal limits for unrestricted release [1][2] A(t) activity after t=1 year of operation*
(A_∞) saturation activity
N_K – nuclei produced per primary particle
C – calculated activity concentration after one year of operation

Nucleus	**N_K in Bq**	**A_∞ in Bq**	**A(t=1a) in Bq**	**$T_{1/2}$**	**C (t=1a) in Bq/cm^3**	**Limit according to StrlSchV in Bq/cm^3**
^{3}H	1.080×10^{-8}	9.237×10^{6}	1.159×10^{4}	12.323 a	72.34	100
^{7}Be	2.587×10^{-9}	2.212×10^{6}	5.028×10^{4}	53.29 d	313.82	10
^{14}C	3.694×10^{-8}	3.159×10^{7}	8.770×10^{1}	5730 a	0.54	1

Only the values for ^{7}Be exceed the allowed dose rate limits for unrestricted release according to radiation protection ordinance (StrlSchV). But also this is reached or fallen below after approximately five half-lives (53.2 d) or 266 days of decay (Table 3). There are two water collection tanks (Fig.10). The capacity of each

of the two tanks is 286 liters. It is therefore possible to collect any leaking water there and let it decay until it falls below the release limit. A possible activation determination of the leakage water takes place by means of a hand probe (e.g. LB134, OD-02...) or a wipe test.

Figure 10: *The two leakage water tanks, 286 Liters each*

An important aspect to be considered is that the contaminated water is not allowed to mix with non-contaminated water (Mixing ban according to §34 StrlSchV). This is achieved by separated drains (Fig.11) in the floors of the accelerator hall and anterooms. Special cable bushings (Fig.12) prevent an infiltration into the cable shafts and a special floor coating avoids an infiltration into the ground.

Figure 11: *Leakage water capturing via drains in the floor*

Figure 12: *Cable bushing*

5 Machine Activation

Four measuring stations are provided for measuring the dose rates caused by activation of machine parts. They are located in the arcs and each one is equipped with a proportional counter tube (Fig.13)

Figure 13: *proportional counter tube installed on the inner side of the first arc*

Figure 14: *Activation measuring monitor for the determination of machine activation*

During operation, these counter tubes are switched off due to the high radiation levels in the accelerator hall. After the machine has been switched off, they are put back into operation. The remaining time until the radiation protection gate can be opened is calculated using the measured radiation levels and a previously determined nuclide vector and displayed in the control system.

6 PSI and exclusion areas

Fig. 15 shows a top view of the bERLinPro basement with the allocation of the exclusion areas. The basement is divided into different exclusion areas, therefore it is not necessary to search the entire facility every time, but only those that have been entered during shutdown.

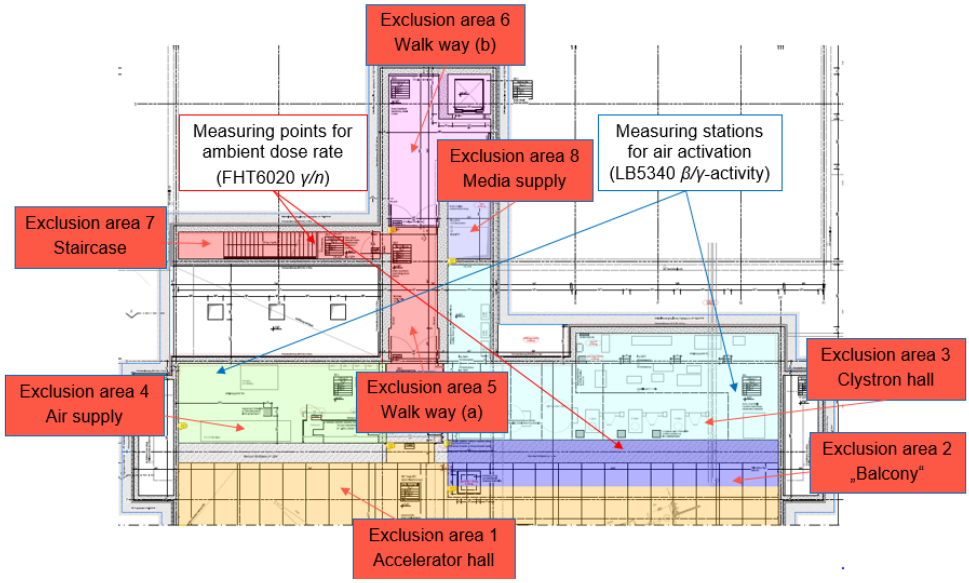

Figure 15: *bERLinPro Basement with exclusion areas (EA1-8)*

During operation EA1-8 are exclusion areas. The operating state is defined as irradiation of the photocathode or the RF supply to at least one cavity. The walk ways (a and b), the Klystron Hall and the air supply sector are at ground level in the hall. The delivery shaft is located on the way to the elevator. It is closed at the top by a ceiling screen. The 10 m long and 3 m wide ceiling screen consists of 50 cm thick, z-shaped concrete blocks made of normal concrete. The cover is not part of the interlock system (covering is not monitored). Due to its high weight, removal is not possible without a crane. Operation without this shielding is prohibited by radiation protection instructions. The elevator is located in the basement during operation and the elevator doors are open. The search button is positioned in such a way that the elevator cabin can also be viewed during the search. The staircase connects the escape route via an exit to the outside and via a second door to the ground level of the technical hall. The media supply sector (EA8) contains an access to the cable duct leading into the bunker.

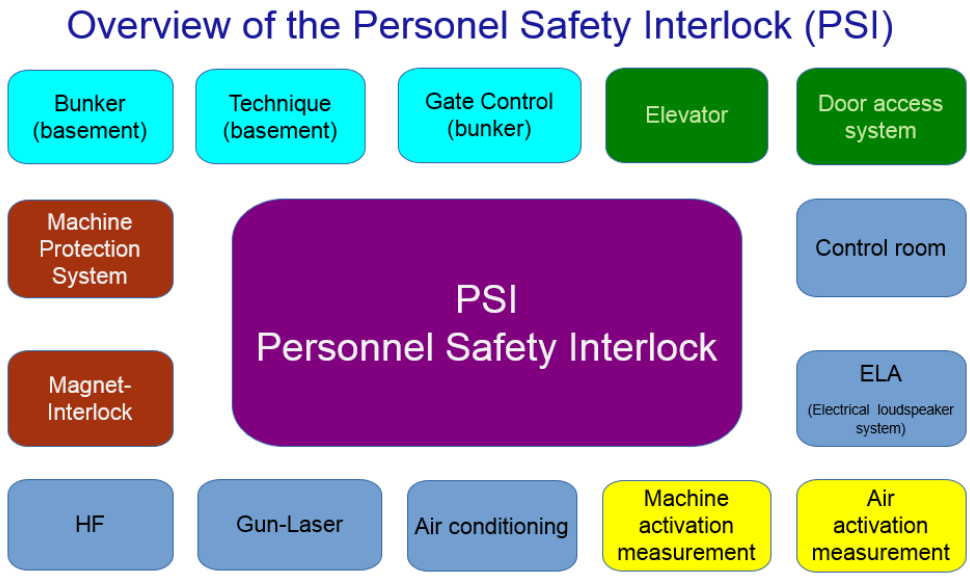

Figure 16: *Overview of the components of the PSI system*

In the bunker there are emergency stop switches, search buttons and LED panels to indicate the interlock status. The technical rooms are equipped in the same way. In addition, the remaining waiting time until the door can be opened is displayed in the control system and in front of the bunker gate. A magnet interlock ensures that the injection energy equals the energy that is absorbed in the dump. When the PSI is switched on, the bunker, the

gallery and the technical rooms in the basement become radiation controlled area which is signalled acoustically and with yellow LED panels in the affected areas. In order to enable operation of the facility, the bunker and gallery must be a restricted area (the red LED panels are switched on). To do this, the corresponding areas must be searched and the successful search confirmed by pressing the search buttons. This is also signalled acoustically. After the PSI has been switched off, all system parts are radiation monitored area. In general, the following remarks apply to the components of the PSI:

a) The door contacts and the associated circuits are redundant.

b) The search of the corresponding area is confirmed by manually pressing the search buttons in the specified order.

c) With the help of a "temporary access", the exclusion areas can be entered and left without breaking the PSI (no further search required). Each person entering the restricted area must remove a key from the key box next to the door and carry it with them until they leave the restricted area. In addition, a log by name is kept in the operating logbook.

d) The acoustic warning consists of an announcement "Attention, the accelerator is switched on" which is repeated for 30 seconds. Only after that a release is possible. At the same time, yellow warning lights are switched on in the exclusion area 1.

e) Next to all search buttons in the exclusion areas there are emergency stop buttons.

f) The monitoring contacts on the laser shutter are redundant.

g) The termination of the beam operation in the accelerator is provided in two independent ways (laser and RF supply).

References

[1] M. Abo-Bakr et al., *bERLinPro: a Prototype ERL for Future Light Sources*, SRF'09, Berlin, Germany, TUPPO017 (2009), http://accelconf.web.cern.ch/AccelConf/srf2009

[2] *Allgemeine Verwaltungsvorschrift zu §47 StrlSchV, Dosisleistungskoeffizienten beiäußerer Strahlungsexposition*, Bundesamt für Strahlenschutz (2013)

[3] M. Helmecke, K. Ott, *Activation Calculation with FLUKA for the bERLinPro Vacuum System*, RADSYNCH2013,BNL, USA(2013)

[4] K. Ott, Y. Bergmann, *Radiation Protection Issues of bERLinPro*, RADSYNCH2015, DESY, Hamburg, Germany(2015)

[5] A. Bundels, K. Ott, *Berechnung Kühlwasseraktivierung bei bERLinPro*, Internal report, HZB (2018)

[6] G. Battistoni, S. Muraro, P.R. Sala, F. Cerutti, A.. Ferrari, S. Roesler, A. Fasso, J. Ranft, *The FLUKA code: Description and benchmarking*, Proceedings of the Hadronic Shower Simulation Workshop 2006, Fermilab 6-8 September 2006, M. Albrow, R. Raja eds., AIP Conference Proceeding 896, 31-49, (2007)

[7] A. Fasso, A. Ferrari, J. Ranft, and P.R. Sala, *FLUKA: a multi-particle transport code*, CERN-2005-10 (2005), SLAC-R-773

[8] K. Ott, Y. Bergmann, M. Martin, L. Pichl *Upgrade of the Neutron Dose Measurement System at BESSY*, IPAC 2017, Copenhagen, Denmark, 2017 May 14-19

[9] *Strahlenschutzverordnung (StrlSchV) 2019*, Bundesamt für Strahlenschutz (29.11.2018)

Radiation Safety at FLUTE with Special Emphasis on Activation Issues

P. Wesolowski, A. Böhm, E. Bründermann, M. Hagelstein, A. Malygin,
S. Marsching, A.-S. Müller, M.J. Nasse, R. Ruprecht, N. Smale,
T. Schmelzer, M. Schuh, O. Zwernemann

Karlsruhe Institute of Technology, Karlsruhe, Germany
October 2019

Abstract

The accelerator FLUTE (name abbreviation derived from its German name: Ferninfrarot Linac- und Test-Experiment) has been set up in cooperation with DESY and PSI [1]. The electron source and diagnostics has commenced operation.
General safety issues of FLUTE are covered in this paper. The activation of the accelerator and vacuum parts were predicted previously [2]. The attention is given to the activation of aluminum and impurities in the electron absorber of the beam dump. Potential air activation in the experimental hall is also discussed.

1 Introduction

The accelerator FLUTE is currently being set up in cooperation with DESY and PSI and commenced operation in 2018 [1]. So far, an rf-photo-injector driven by a $6\,\mathrm{mJ}$ titanium-sapphire laser and the diagnostics up to $5.5\,\mathrm{MeV}$ were commissioned. Since the FLUTE experimental hall is surrounded by thick concrete walls and no activation whatsoever is expected below $10\,\mathrm{MeV}$, no major radiation protection issues are taken into account. However, when an extension by an accelerator linac and a magnetic bunch compressor will be added, the energy will increase to approximately to $50\,\mathrm{MeV}$. Hence, the activation in accelerator components, as well in air, has to be considered. In the present paper, the activation of accelerator parts will be limited to the dump absorber, as activation in other components, at least in the course of regular operation, will remain manageable.

2 Personal safety

The existing FLUTE experimental hall is surrounded by concrete walls of at least $1.5\,\mathrm{m}$ thickness, that provide extensive radiation protection and simplify remaining safety issues considerably. The access doors to the experimental hall are labyrinthed by thick concrete walls as well. The main revolving door consists of steel and concrete and has a minimum shielding equivalence of $1.5\,\mathrm{m}$ concrete. Nevertheless, some scenarios as, e.g., a direct interaction of the primary beam with matter may make the existing concrete shielding insufficient. Additionally, an activation of the absorber, even if well contained, has to be considered.

The area inside the experimental hall is a temporary exclusion area. No person is allowed to stay in this area during the accelerator operation. This area is protected by a personal interlock system. This has to be set by the operator before starting accelerator operation. The setting procedure requires a visual search of the area and pushing a predefined sequence of search-up buttons. This search process is announced and accompanied by acoustic and light warnings. After the search procedure, the revolving door of the experimental hall is closed

by the operator and the temporary exclusion area can be set by pressing a button outside of the experimental hall. If the temporary exclusion area is inactive, the rf cannot be switched on.

A person overlooked in the experimental hall can interrupt the search and disable the temporary exclusion area any time by pressing one of the emergency buttons installed at each wall of the hall. This results in the immediate switch off the main RF drive.

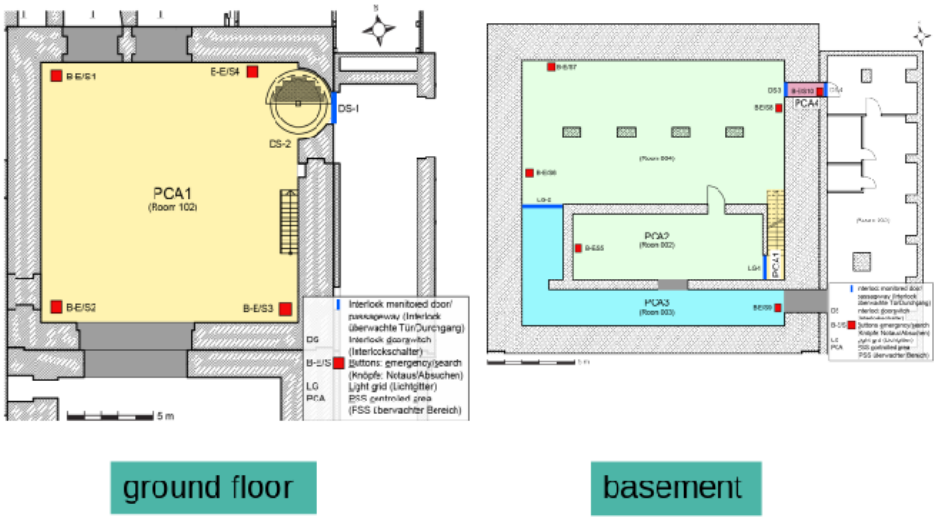

Figure 1: *The personal safety system. Left - ground floor with clearly visible revolving door) and, Right – basement. Both floors are temporary exclusion areas, interlocked during the operation.*

3 Beam dump

The beam dump was identified as the most pronounced source of radiation. In the following, the equivalent radiation dose originating from the bremsstrahlung in the beam dump, its activation, as well air activation originating from the dump are elaborated.

FLUTE operation is limited to the electron energy of less than $10\,\mathrm{MeV}$ so far. A downscale version of a dump is used for this purpose. The electron beam is fully absorbed in an aluminum cylinder (thickness=$15\,\mathrm{mm}$) mounted on the inner side of the vacuum flange terminating the electron beam guidance. There is an unsubstantial amount of bremsstrahlung- x-rays and gammas transmitted through the vacuum system tubes and flanges, accompanied by a minor neutron flux, both measured inside the experimental hall. The presence of neutron flux is yet unexplained and still under investigation. This neutron flux during the operation is not related – as reasonably explained by beam energy not reaching the activation energy of any typical nuclear reaction – by any post-irradiation activation.

The situation will most probably change when the energy will increase by $40-50\,\mathrm{MeV}$, when using a linac extension. For minimizing the potential activation in the absorber a material was chosen with low susceptibility for nuclear reactions. A pure aluminum block (chemical purity better than 99.995%) was chosen, surrounded by a led shielding (Figure 2).

The dump was intentionally over-dimensioned to accommodate the higher total beam load in the dump related to potential high dark currents originating from the cathode or the $2\frac{1}{2}$ cell rf-cavity. In addition, the shielding is designed and constructed in a way, that its modular extension with standard lead bricks will be anytime possible. The next Section will cover the activation issues in the dump.

Table 1: *Summary of saturation activity for the aluminum of the dump absorber. The nuclear activation data was taken from [3]. Column 2 specifies the daughter nuclide considered, columns 4-6 give the threshold energy for the reaction and the specific saturation activation coefficients per* kW *e-beam power As for two electron energies, approximately corresponding to electron energies in different operational regimes of FLUTE.*

1	2	3	4	5	6	7
target	nulclide	$T_{1/2}$	Threshold	A_S GBq/kW at e-beam energy [MeV]		activity at 35 MeV
			[MeV]	10	35	Bq
Al	Na-24	14.96h	23.71	0	1.1	1.2
	Al-26m	6.37s	13.03	0	325	341.3

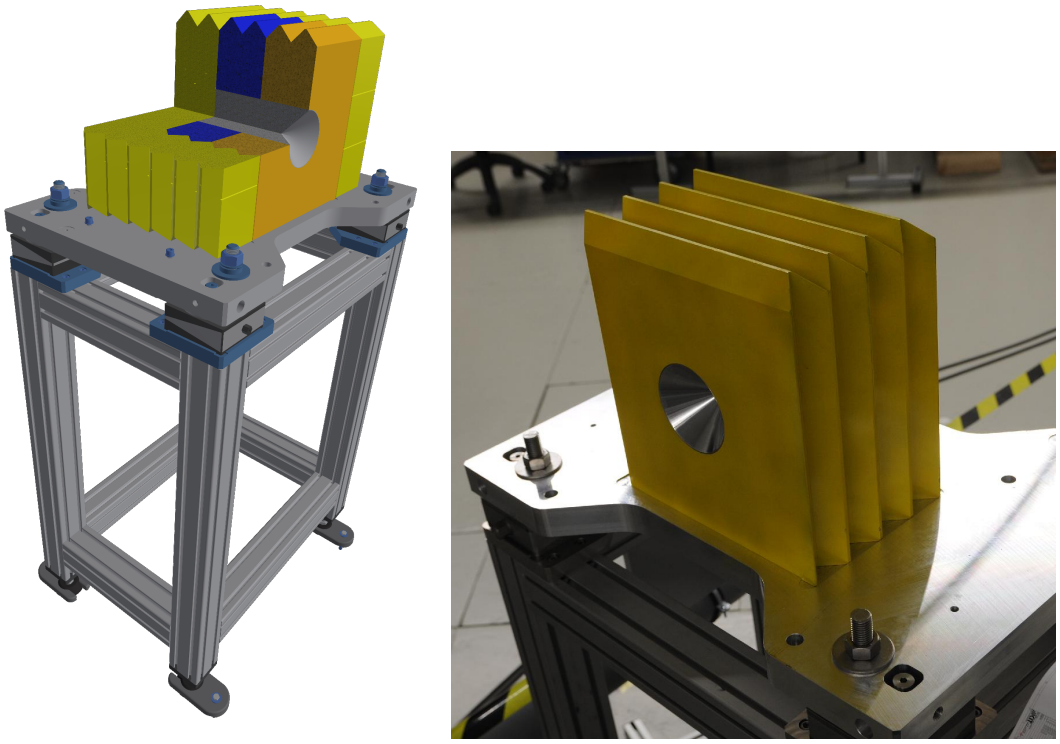

Figure 2: *The electron beam dump. Left – CAD drawing, Right – realization of its core elements. The lead shielding can be added on demand. This option of a modular shielding extension is kept open if unexpectedly high beam currents (as, e.g., increased dark currents originating from the cathode and rf-cavity) have to be handled.*

4 Activation in the dump at higher energy electron beam

For coarse estimations, a saturation activation of typical reaction products was chosen. For pure aluminum, two most prominent daughter nuclides were considered after [3]: Al-26m and Na-24. The latter originates from a sophisticated (n,α) reaction with a considerable cross section [4]. The overview is given in Table 1.

The value for Na-24 is manageable, especially as well contained in the absorber and attenuated by lead shielding (see Section 3). The initial activation with Al-26m seems high, but cools down, due to the short decay half time (6.35 s) by a factor of 106 within three minutes. This time is substantially shorter than the opening time of the massive revolving door, separating the FLUTE experimental hall from the foyer and control room (see Section

Table 2: *Summary of saturation activity for impurities in the dump absorber. Column 7 gives the activation values for three daughter products originating of stable Iron. They are scaled down with the spurious iron concentration in the absorber. Due to high purity of the absorber, the values are very low. See caption for Table 1 for more details.*

1	2	3	4	5	6	7
target	nulclide	$T_{1/2}$	Threshold	A_S GBq/kW at e-beam energy [MeV]		activity at 35 MeV
			[MeV]	10	35	Bq
Fe	Mn-54	303d	20.42	0	22	570.6
	Mn-56	2.57h	10.57	0	1.23	1.1
	Fe-53	8.51m	13.62	0	27	700.2

2 and Figure 1). The machining, decommissioning and disposing of the dump is prohibited for operators and technicians and can be managed only by qualified radiation safety staff. Hence, the exposition of staff with activation products in the absorber is excluded. The activation numbers are based on an energy of $35\,\mathrm{MeV}$, as known in the literature and given in [3].

Table 2 summarizes the saturation activation originating from iron impurity concentration in the aluminum absorber. Due to chemical analysis of the aluminum block, the spurious iron content is $24.7\,\mathrm{ppm}$. Its reciprocal value corresponds to a factor, in which the saturation activity scales down in relation to a (hypothetically) pure iron material.

5 Prediction of the hall air activation at higher energy electron beam

The quantification of expected experimental hall air activation during operation with up to $90\,\mathrm{MeV}$ electron energy (more than ever envisaged) was requested by the competent Authority as a document accompanying the application for the operational license for FLUTE. The estimations were provided using a straightforward and easily to be followed method, based on consideration of potential nuclear reactions in air. The most gamma radiation was expected to origin from the shielded dump absorber. The estimations were presented prior to this paper [2]. The activations during the future operation, using design parameters of FLUTE, were compared to an activation budget given by regulations, concluding, that only a total fraction of 3% was exploited (see Table 3).

6 Conclusion

In the present early stage of operation of FLUTE no activation of any accelerator component or air was predicted nor measured. The consideration of the potential activation in later stages at higher energies have also been considered. The activation of components, especially the beam dump, remains manageable.

Special attention was given to the activation of air. A closed air circulation in air potentially increases risk of concentrating the reaction products with run time. Despite this specific feature of FLUTE, which was financial budget-related, the activation of air remains far below exemption limits, defined by the regulations.

References

[1] M.J. Nasse, A. Bernhard, A. Böhm, E. Bründermann, S. Funkner, B. Härer, I. Kriznar, A. Malygin, S. Marsching, W. Mexner, G. Niehues, R. Ruprecht, T. Schmelzer, M. Schuh, N. Smale, P. Wesolowski,

Table 3: *Calculated total and specific activations (3rd and 4th columns) of the hall air with chosen daughter isotopes originating from reactions with air components [2]. Comparison with limits given in the Appendix VII of StrlSchV (German Radiation Protection Ordinance) are shown, according to a scheme defined ibidem for determining their exemption in a particular case (last column); see [2] for details. Please note that total exploitation of activation budget (lower right number) is lower than 3%*

				limits			
Nulcide	$\mathbf{T}_{1/2}$ h	**activation** Bq	**activation** Bq/m^3	**inhalation** Bq/m^3	**submersion** Bq/m^3	**after App VII** Bq/m^3	**exploited**
^{13}N	1.66E-01	1.00E+05	5.90E+01	n.a.	2.00E+03	2.00E+04	2.95E-03
^{15}O	3.39E-02	1.07E+04	6.30E+00	n.a.	1.00E+03	1.00E+04	6.30E-04
^{14}C	4.99E+07	5.15E+00	3.03E-03	6.00E+00	n.a.	6.00E+01	5.05E-05
^{41}Ar	1.83E+00	6.94E+04	4.08E+01	n.a.	2.00E+02	2.00E+03	2.04E-02
^{11}C	3.39E-01	3.77E+04	2.22E+01	6.00E+02	3.00E+03	6.00E+03	3.69E-03
Sum							0.028

M. Yan, A-S. Müller, *First electron beam at the linear accelerator FLUTE at KIT*, Proceedings of 10th International Particle Accelerator Conference, IPAC2019, Melbourne, Australia, 2019, p. 882

[2] P. Wesolowski, E. Bründermann, M. Hagelstein, E. Huttel, A.-S. Müller, R. Ruprecht, M. Schuh, M. Schwarz, O. Zwernemann, *Ab initio method for dose estimation in a linear electron accelerator*, Proceedings of RadSynch2017, Hsinchu, Taiwan, 2017, p. 122

Radiation levels around SOLARIS 1.5 GeV storage ring after the machine commissioning

Justyna Wiklacz, Magdalena Jaglarz, Adriana Wawrzyniak

National Synchrotron Radiation Center SOLARIS
October-2019

Abstract

The commissioning of the SOLARIS storage ring started in 2015 and since then radiation measurements has been performed using radiation monitoring stations and thermoluminescence dosimeters (TLDs). In the meantime several improvements to the radiation shielding were done to fulfill the ALARA principle. To reduce electron losses and decrease radiation levels around the synchrotron, optimizations of the electron beam during injection into the storage ring, ramping and standard operation were carried out.

Radiation measurements results received before and after the chopper installation in the linac and additional problems with radiation levels while the beam current is increasing to the designed $500\,\mathrm{mA}$ value are presented.

1 SOLARIS machine and beamlines

The SOLARIS machine is made up of the $40\,\mathrm{m}$-long linear accelerator with a thermionic gun and 6 acceleration sections, the transfer line and the $1.5\,\mathrm{GeV}$ storage ring. The ring consists of 12 Double-Bend Achromat cells, 12 straight sections, 2 main cavities and 2 Landau cavities. This third (3rd) generation light source has circumference of $96\,\mathrm{m}$ and can operate with $500\,\mathrm{mA}$ stored current. The ramping mode is used to achieve the full electron energy.

In the Fig.1 the machine outline and designed parameters are presented.

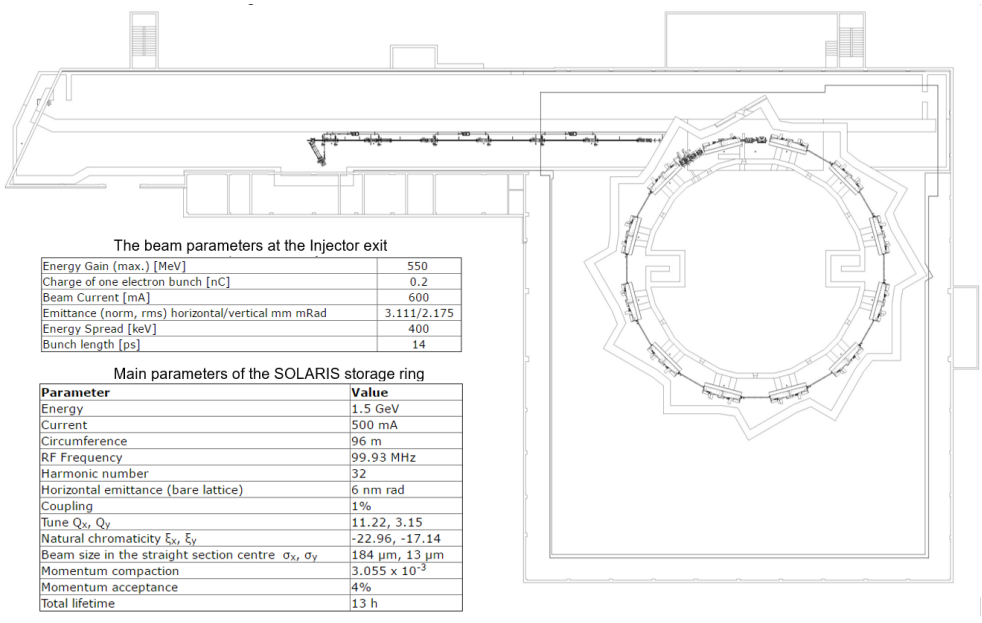

The beam parameters at the Injector exit

Energy Gain (max.) [MeV]	550
Charge of one electron bunch [nC]	0.2
Beam Current [mA]	600
Emittance (norm, rms) horizontal/vertical mm mRad	3.111/2.175
Energy Spread [keV]	400
Bunch length [ps]	14

Main parameters of the SOLARIS storage ring

Parameter	Value
Energy	1.5 GeV
Current	500 mA
Circumference	96 m
RF Frequency	99.93 MHz
Harmonic number	32
Horizontal emittance (bare lattice)	6 nm rad
Coupling	1%
Tune Q_x, Q_y	11.22, 3.15
Natural chromaticity ξ_x, ξ_y	-22.96, -17.14
Beam size in the straight section centre σ_x, σ_y	184 µm, 13 µm
Momentum compaction	3.055×10^{-3}
Momentum acceptance	4%
Total lifetime	13 h

Figure 1: *The scheme and the parameters of the SOLARIS machine.*

Table 1: *Workers categories, their dose limits and corresponding area classification.*

Category	Dose limits	Who?	Area classification
Radiation workers category A	$20\,\mathrm{mSv/year}$	No workers at Solaris	Controlled area
Radiation workers category B	6 mSv/year	Technical team of Solaris, Radiation Protection Officer	Supervised area
Public	$1\,\mathrm{mSv/year}$	Administrative and external workers, users, visitors	Unclassified area

The building construction started in January 2012 and in May 2015, after one year of the machine installation, the commissioning of the storage ring has begun. Two beamlines, UARPES and PEEM/XAS which were designed in parallel with the machine, started the commissioning in April 2016 and in April 2017, respectively. Finally in October 2018 first users could have performed their experiments at SOLARIS.

Through all these years the commissioning of the storage ring was continuously proceeded and as a result of this progress in January 2018 the designed electron current $500\,\mathrm{mA}$ was reached. Right now the average operational current is about $300\,\mathrm{mA}$.

2 Polish regulations and area classification during operation

In Poland all the radiation protection requirements are described by the Atomic Law act and additionally clarified in government regulations. In accordance with them, the SOLARIS facility is the accelerator laboratory and it involves unclassified, supervised and controlled areas. Furthermore, SOLARIS workers are dived into non-radiation workers, radiation workers category B and radiation workers category A. Dose limits for workers and classified areas are presented in the Table 1 and areas division during the machine commissioning is shown in the Fig. 2.

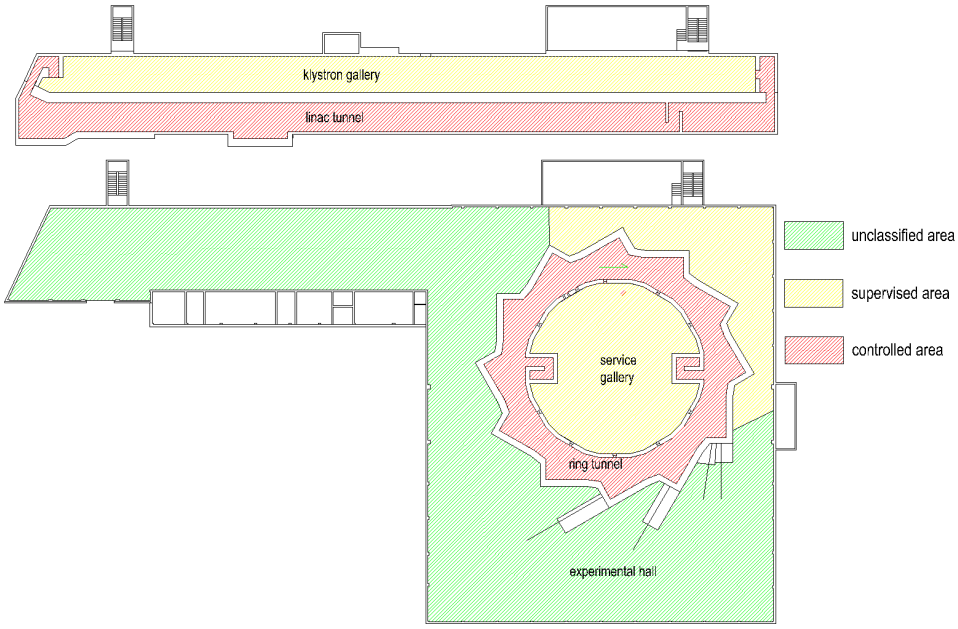

Figure 2: *Area classification during the commissioning at SOLARIS.*

3 Radiation measurement equipment

To measure radiation levels during the machine commissioning and normal operation radiation monitoring system has been used. Currently it contains 9 gamma detectors – Thermo FHT 192 ionization chambers, and 2 neutron detectors – Thermo FHT 752. Dose rates and accumulated doses are monitored 24 hours per day in selected places around the storage ring and next to the beamlines. The results are available locally on a display and in the control room thorough the Tango system. Additionally, dose values from the radiation stations are archived. The typical positions of the radiation monitoring stations at SOLARIS are presented in the Fig. 3.

Moreover, environmental measurements are carried out with thermoluminescence dosimetry (TLD). About 40 points at the whole facility were selected for TLD dosimeters placement and they are read-out once per three months. Moreover, cyclic measurements around the whole facility are performed using portable radiometers: Thermo FH 40 G-L10 proportional counter, Fluke ASM 990S with the 489-35 Geiger–Müller counter and the Rotem RAM ION ionization chamber. All these activities allow to evaluate people exposure to ionizing radiation.

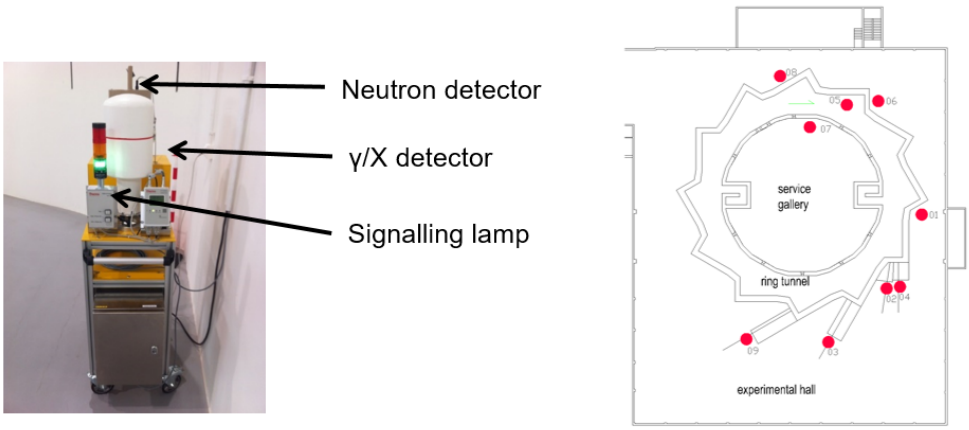

Figure 3: *A radiation monitoring station and the positions of the station at SOLARIS (red spots).*

4 Radiation at the injection region on the experimental hall

During early stage of the commissioning high radiation levels were found, what was described in [1] and [2]. Especially, on the experimental hall in sections 1-3 significant dose rates were reached, what caused the necessity of access limitation and determining the controlled area in this zone. Examples of dose rate levels during injection and ramping processes are shown in Fig. 4.

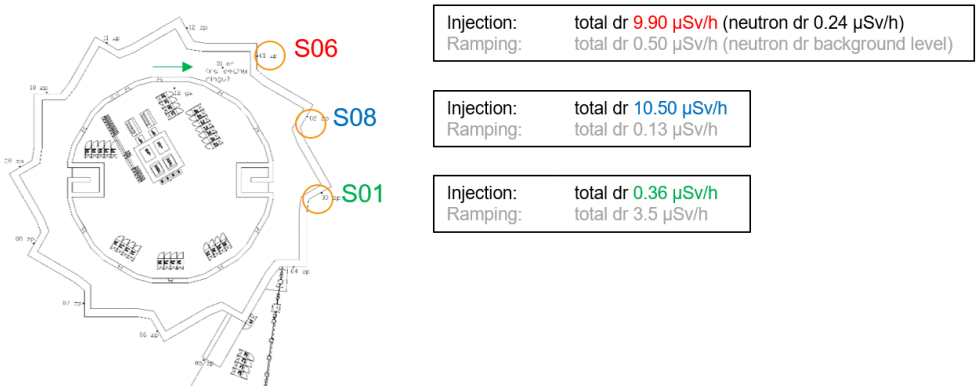

Figure 4: *Dose rate levels during injection and ramping, March 2017, Current:* $\sim 250\,\mathrm{mA}$

.

In the following months the machine was going through optimization to increase injection efficiency and therby

to reduce the radiation levels. Additionally, in December 2017, the machine started to operate with a chopper in the linac, what also improved the injection efficency. The chopper has been installed just after the gun to reduce high-energy electron losses along the injector, in the transfer line and in the storage ring [3]. From the radiation protection point of view, installation of the chopper was a very good option, because radiation levels during electron injection into the storage ring has been reduced five times (Fig. 5). Further measurements have shown that dose rate levels are reasonable also with increased klystrons' repetition rate up to 2 Hz, what is illustrated in Fig. 6.

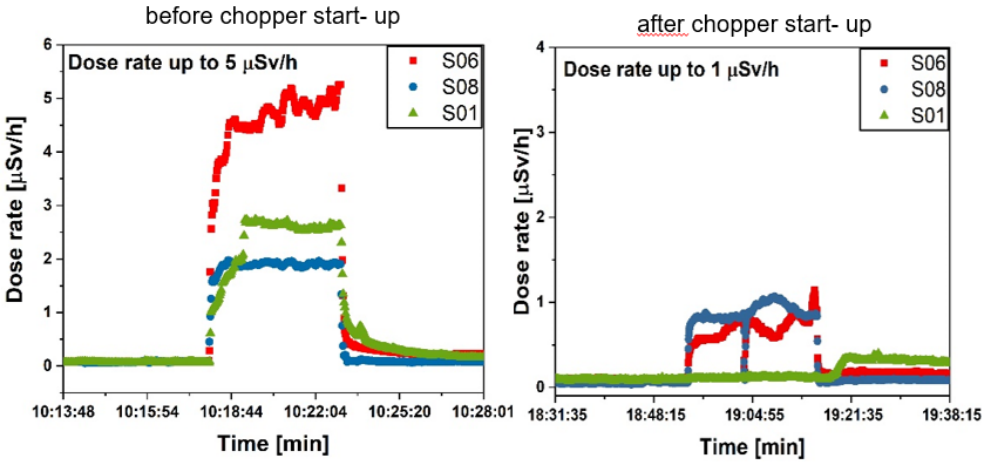

Figure 5: *Radiation levels during injection before and after chopper installation. 05.12.2017 Injection up to* $\sim$200 mA*, klystrons repetition rate* 1 Hz

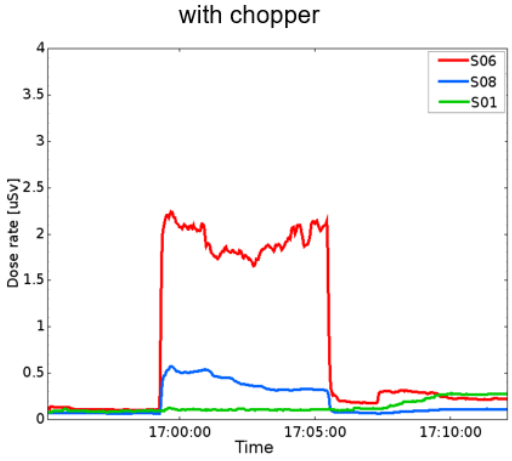

Figure 6: *Radiation levels during injection after chopper installation. 24.04.2019 Injection up to* $\sim$250 mA*, klystrons repetition rate 2 Hz*

5 Radiation on the experimental hall around the ring with higher currents

Unfortunately, start-up of the chopper has not solved the problems with too high radiation levels when the stored beam current is above 250 mA. Measurements with portable meters were performed to evaluate radiation levels at 350 mA stored current. Problems with too high radiation appeared at every ratchet wall at the 0 deg port. Almost in every section dose rates were higher than the limits for unclassified area (see Fig. 7).

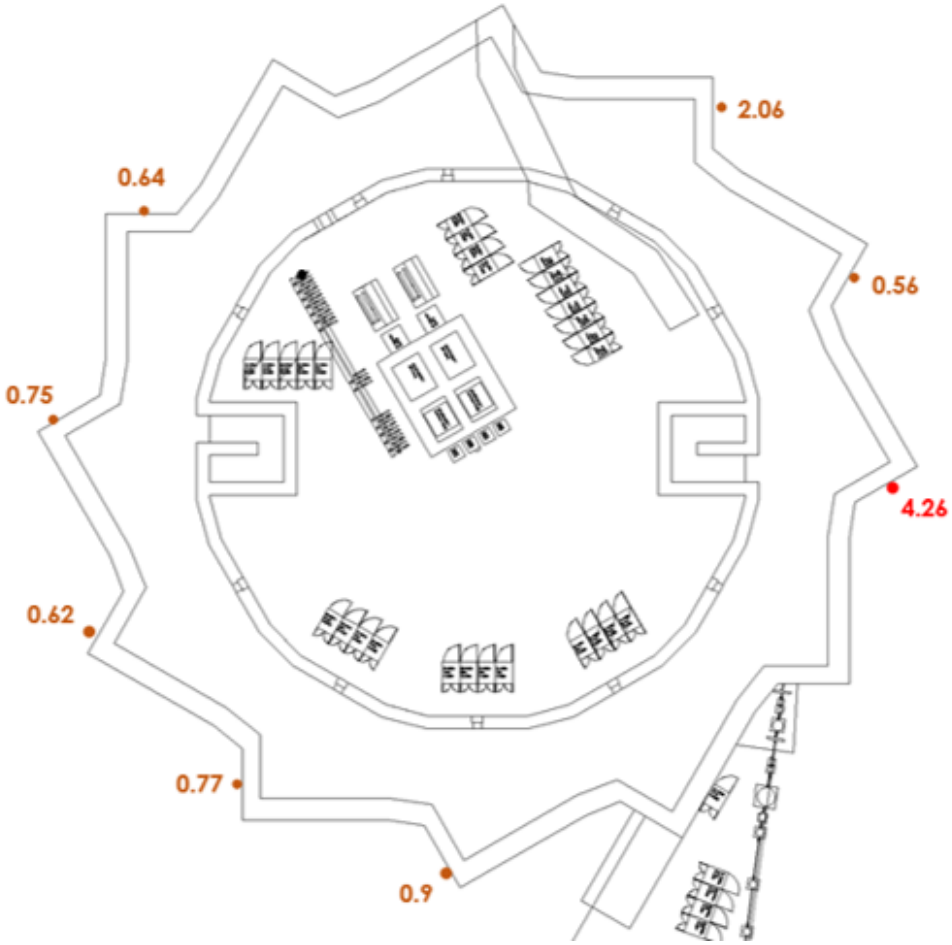

Figure 7: *Radiation levels directly next to the walls, results in* $\mu\mathrm{Sv}/\mathrm{h}$. *31.01.2018, stored current* $350\,\mathrm{mA}$

At the SOLARIS facility the ALARA principle is strictly followed, so to allow users to work on the experimental hall without any restrictions it is needed to keep it like the unclassified area. Therefore, as presented in Fig. 2, whole injection area is fenced and properly marked. In addition, if operation with higher currents (more than $300\,\mathrm{mA}$) is performed, measurements with portable radiometers are carried out to assess dose rates and some areas are fenced if necessary.

It is planned to add lead walls on the ring ratchet walls in section 1-3 (0^o ports) to eliminate supervised area in the injection region. Moreover, operation with currents higher than $250\,\mathrm{mA}$ requires further beam optimization and/or placing some additional shielding on every ring ratchet wall (0^o port) and/or defining radiation zones as a temporary solution.

6 Ongoing works at SOLARIS

Besides improving the quality of the electron beam and being concerned with presented radiation protection issues, activities at SOLARIS facility are focused on designing, installation and commissioning of new beamlines. PHELIX beamline, using APPLE II undulator with permanent magnets and soft X-rays for experiments, has already started the commissioning. Another one, XMCD beamline (old MAX-Lab I1011) with EPU undulator, PEEM microscope and STXM, is under construction. Two more beamlines, SOLCRYS and SOLABS, are under design with cooperation with foreign partners.

Recently two diagnostic beamlines have been built. First – PINHOLE beamline, analyzing the emitted X-rays and monitoring such beam parameters as position, transverse beam profiles, emittance in real time, has been in operation since September 2018 and the next one, LUMOS, is under construction. The commissioning of it is foreseen by the end of 2019.

References

[1] J. Wiklacz, *Radiation Protection Issues at SOLARIS - Safety Assumptions and Project Status*, Radsych15, Desy, June 2015

[2] J. Wiklacz, *Update of the commissioning of the SOLARIS 1.5 GeV storage ring*, Radsynch17, NSRRC Taiwan, April 2017

[3] M. Jaglarz, J. Wiklacz, A. Wawrzyniak, *Radiation Safety at SOLARIS 1.5 GeV storage ring*, IPAC'19, Melbourne, May 2019